UC-413
LBL-27687

Lawrence Berkeley Laboratory
UNIVERSITY OF CALIFORNIA

Physics Division

Fragmentation Properties of Jets Produced in Proton-Antiproton Collisions at $\sqrt{s} = 1.8$ TeV

B. Hubbard
(Ph.D. Thesis)

November 1989

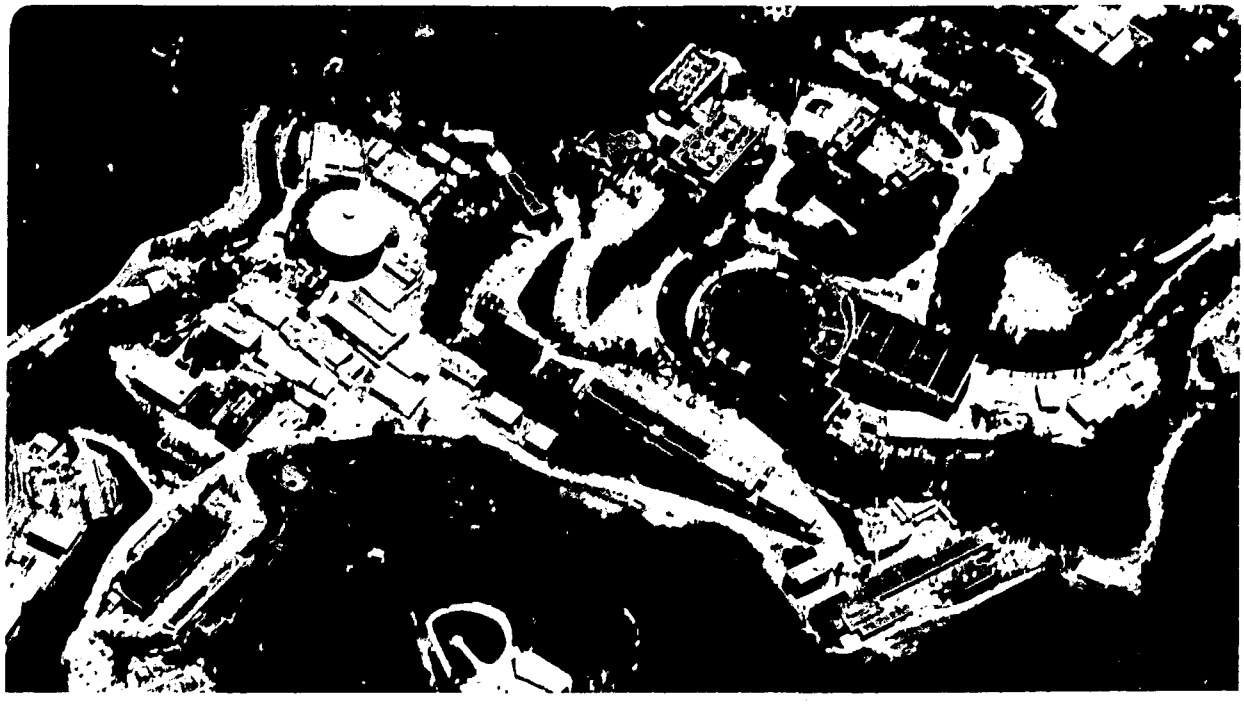

Prepared for the U.S. Department of Energy under Contract Number DE-AC03-76SF00098.

DISCLAIMER

LBL-27687

Fragmentation Properties of Jets Produced in Proton-Antiproton Collisions at $\sqrt{s} = 1.8$ TeV

by
Bradley Hubbard
Ph.D. Thesis
November, 1989

Department of Physics
University of California
and
Physics Division
Lawrence Berkeley Laboratory
1 Cyclotron Road
Berkeley, CA 94720

Abstract

Jet fragmentation properties have been studied in collisions of protons and antiprotons at a center-of-mass energy of 1.8 TeV, using the Collider Detector at Fermilab (CDF). The fractional momentum distribution of charged particles within jets is presented and compared with Monte-Carlo predictions. With increasing di-jet invariant mass from 60 to 200 GeV/c^2 the fragmentation is observed to soften as predicted by scale breaking effects in Quantum Chromodynamics (QCD). The charged multiplicity in the jet core is observed to rise with di-jet invariant mass.

This work was supported by the U.S. Department of Energy and Lawrence Berkeley Laboratory under Contract DE-AC03-76SF00098.

Acknowledgements

The past few years spent doing my graduate work on the CDF experiment have been very rewarding for me. I've seen that performing an experiment of this magnitude requires the effort of a large number of people, from different institutions and different countries, to accomplish the wide variety of technical and clerical tasks. I extend my gratitude to all my collaborators (some of which I have not met personally) for their efforts which have made the experiment and my dissertation possible.

Especially to the local contingent from the Lawrence Berkeley Laboratory, who have provided a comfortable, small group atmosphere to the project. Special thanks to Willy Chinowsky, my thesis advisor, for igniting my interest in this topic and for extending his wisdom in physics and in life; to Jim Siegrist, for providing a great deal of inspiration and advice, both on the nitty-gritty and the broader picture; to Bob Ely, Bill Carithers and Lina Galtieri for the help and encouragement they have given me; and to Carl Haber, Mike Gold, Paul Tipton and Robert Harris, who have made this experience fun and shown me how to keep things in perspective.

Most of all, I thank my wife Elizabeth for her love and support during these exhausting years. She has made this graduate experience something I will never forget, and, with the aid of her parents, siblings and friends has made me feel very much at home here in California.

Finally, I am most grateful to my parents, who, by bringing me up and supporting me in my education, have given me my scientific curiosity and my outlook on life.

Contents

Abstract i

Acknowledgements ii

1 Introduction 1

1.1 Hadron Collisions 4

1.2 Jet Fragmentation 6

2 Experiment Description 9

2.1 CDF Experiment Overview 9

2.2 Tevatron Collider 11

2.3 Tracking Detectors 12

2.3.1 General Tracking Principles 13

2.3.2 Vertex Time Projection Chambers 15

2.3.3 Central Tracking Chamber 16

2.3.4 CTC Track Reconstruction 19

2.3.5 Tracking Simulation 19

2.3.6 Performance 20

2.3.7 Track Selection Criteria 23

2.3.8 Track Finding Efficiency 23

2.3.9 CTC Track Resolution 26

2.4 Calorimetry 28

2.4.1 Central and Endwall Calorimeters 30

2.4.2 Endplug and Forward Calorimeters 36

2.5 Data Acquisition and Trigger 37
2.5.1 Trigger System 37

3 Jets in CDF **39**

3.1 Jet Definition 39
3.1.1 CDF Jet Clustering Algorithm 39
3.1.2 Monte-Carlo Jet Definition 41
3.2 Jet Energy/Momentum Corrections 42
3.2.1 Tracking Correction to Jet Energy and Momentum 43
3.2.2 Average Jet Energy/Momentum Correction 46
3.2.3 Systematic Uncertainty on the Jet Corrections 49
3.3 Jet Angular and Momentum Resolution 49
3.4 Dijet Event Selection 53

4 Jet Fragmentation Properties **59**

4.1 Definition of Variables and General Issues 59
4.2 Corrections to the Raw dN/dZ Distribution 61
4.2.1 Acceptance Corrections 62
4.2.2 Tracking Efficiency 65
4.2.3 Underlying Event 66
4.2.4 Correction for Detector Resolution 67
4.3 Backgrounds and Systematic Uncertainties to dN/dZ 70
4.3.1 Estimation of Backgrounds 70
4.3.2 Estimation of Systematic Errors 74
4.3.3 Consistency Checks 76
4.4 Results 76
4.4.1 dN/dZ 76
4.4.2 Evolution with Dijet Invariant Mass. 77
4.4.3 Extraction of $< f_{ch} >$ 81

4.5 Transverse Fragmentation Properties 82
4.5.1 Transverse Momentum Distribution 82
4.5.2 Charged Particle Rapidity Distribution 84

5 Summary and Conclusions **89**

A CTC Track Reconstruction **91**

B CTC Tracking Efficiency Studies **95**

B.1 Merging Single Tracks with Jet Data 95
B.2 Monte-Carlo Event Simulation 98
B.3 Estimating Efficiency from Data 99

C Unfolding Detector Resolution Effects to the Charged Fragmentation Function **100**

C.1 General Procedure 100
C.2 Unfolding the Jet Momentum Spectrum 102
C.3 Unfolding the Fragmentation Function 103

THE CDF COLLABORATION

F.Abe,[16] D.Amidei,[3] G.Apollinari,[11] G.Ascoli,[7] M.Atac,[4], P.Auchincloss,[14] A.R.Baden,[6] A.Barbaro-Galtieri,[9] V.E.Barnes,[12] F.Bedeschi,[11] S.Behrends,[12] S.Belforte,[11] G.Bellettini,[11] J.Bellinger,[17] J.Bensinger,[2] A.Beretvas,[14] P.Berge,[4] S.Bertolucci,[5] S.Bhadra,[7] M.Binkley,[4] R.Blair,[1] C.Blocker,[2] J.Bofill,[4] A.W.Booth,[4] G.Brandenburg,[6] D.Brown,[6] A.Byon,[12] K.L.Byrum,[17] M.Campbell,[3] R.Carey,[6] W.Carithers,[9] D.Carlsmith,[17] J.T.Carroll,[4] R.Cashmore,[4] F.Cervelli,[11] K.Chadwick,[4,12] T.Chapin,[13] G.Chiarelli,[11] W.Chinowsky,[9] S.Cihangir,[15] D.Cline,[17] D.Connor,[10] M.Contreras,[2] J.Cooper,[4] M.Cordelli,[5] M.Curatolo,[5] C.Day,[4] R.DelFabbro,[11] M.Dell'Orso,[11] L.DeMortier,[2] T.Devlin,[14] D.DiBitonto,[15] R.Diebold,[1] F.Dittus,[4] A.DiVirgilio,[11] J.E.Elias,[4] R.Ely,[9] S.Errede,[7] B.Esposito,[5] B.Flaugher,[14] E.Focardi,[11] G.W.Foster,[4] M.Franklin,[6,7] J.Freeman,[4] H.Frisch,[3] Y.Fukui,[8] A.F.Garfinkel,[12] P.Giannetti,[11] N.Giokaris,[13] P.Giromini,[5] L.Gladney,[10] M.Gold,[9] K.Goulianos,[13] C.Grosso-Pilcher,[3] C.Haber,[9] S.R.Hahn,[10] R.Handler,[17] R.M.Harris,[9] J.Hauser,[3] T.Hessing,[15] R.Hollebeek,[10] L.Holloway,[7] P.Hu,[14] B.Hubbard,[9] P.Hurst,[7] J.Huth,[4] H.Jensen,[4] R.P.Johnson,[4] U.Joshi,[14] R.W.Kadel,[4] T.Kamon,[15] S.Kanda,[16] D.A.Kardelis,[7] I.Karliner,[7] E.Kearns,[6] R.Kephart,[4] P.Kesten,[2] H.Keutelian,[7] S.Kim,[16] L.Kirsch,[2] K.Kondo,[16] U.Kruse,[7] S.E.Kuhlmann,[12] A.T.Laasanen,[12] W.Li,[1] T.Liss,[3] N.Lockyer,[10] F.Marchetto,[15] R.Markeloff,[17] L.A.Markosky,[17] P.McIntyre,[15] A.Menzione,[11] T.Meyer,[15] S.Mikamo,[8] M.Miller,[10] T.Mimashi,[16] S.Miscetti,[5] M.Mishina,[8] S.Miyashita,[16] N.Mondal,[17] S.Mori,[16] Y.Morita,[16] A.Mukherjee,[4] C.Newman-Holmes,[4] L.Nodulman,[1] R.Paoletti,[11] A.Para,[4] J.Patrick,[4] T.J.Phillips,[6] H.Piekarz,[2] R.Plunkett,[13] L.Pondrom,[17] J.Proudfoot,[1] G.Punzi,[11] D.Quarrie,[4] K.Ragan,[10] G.Redlinger,[3] J.Rhoades,[17] F.Rimondi,[4] L.Ristori,[11] T.Rohaly,[10] A.Roodman,[3] A.Sansoni,[5] R.Sard,[7] V.Scarpine,[7] P.Schlabach,[7] E.E.Schmidt,[4] P.Schoessow,[1] M.H.Schub,[12] R.Schwitters,[6] A.Scribano,[11] S.Segler,[4] M.Sekiguchi,[16] P.Sestini,[11] M.Shapiro,[6] M.Sheaff,[17] M.Shibata,[16] M.Shochet,[3] J.Siegrist,[9] P.Sinervo,[10] J.Skarha,[17] D.A.Smith,[7] F.D.Snider,[3] R.St.Denis,[6] A.Stefanini,[11] Y.Takaiwa,[16] K.Takikawa,[16] S.Tarem,[2] D.Theriot,[4] A.Tollestrup,[4] G.Tonelli,[11] Y.Tsay,[3] F.Ukegawa,[16] D.Underwood,[1] R.Vidal,[4] R.G.Wagner,[1] R.L.Wagner,[4] J.Walsh,[10] T.Watts,[14] R.Webb,[15] T.Westhusing,[7] S.White,[13] A.Wicklund,[1] H.H.Williams,[10] T.Yamanouchi,[4] A.Yamashita,[16] K.Yasuoka,[16] G.P.Yeh,[4] J.Yoh,[4] F.Zetti[11]

[1] Argonne National Laboratory, Argonne, Illinois 60439
[2] Brandeis University, Waltham, Massachusetts 02254
[3] University of Chicago, Chicago, Illinios 60637
[4] Fermi National Accelerator Laboratory, Batavia, Illinois 60510
[5] Laboratori Nazionali di Frascati of the Istituto Nazionale di Fisica Nucleare, Italy
[6] Harvard University, Cambridge, Massachusetts 02138
[7] University of Illinois, Urbana, Illinois 61801
[8] National Laboratory for High Energy Physics (KEK), Tsukuba-gun, Ibaraki-ken 305, Japan
[9] Lawrence Berkeley Laboratory, Berkeley, California
[10] University of Pennsylvania, Philadelphia, Pennsylvania 19104
[11] Istituto Nazionale de Fisica Nucleare, University and Scuola Normale Superiore, Pisa, Italy
[12] Purdue University, West Lafayette, Indiana 47907
[13] Rockefeller University, New York, New York 10021
[14] Rutgers University, Piscataway, New Jersey 08854
[15] Texas A&M University, College Station, Texas 77843
[16] University of Tsukuba, Ibaraki 305, Japan
[17] University of Wisconsin, Madison, Wisconsin 53706

Chapter 1

Introduction

Over the past few decades, there has been substantial progress in understanding the nature of matter at the smallest scale - the elementary particles and their interactions. On the experimental side, technological advances in accelerators, detectors, electronics and computers have enabled physicists to observe elementary particle interactions at very high energies (equivalently, at small distances), facilitating many discoveries such as the quark structure of nucleons and the existence of vector bosons. On the theoretical side, a vast quantity of knowledge about elementary particles and forces has been incorporated into a simple framework known as the 'standard model'. This theoretical synthesis has brought about many predictions which thus far have not been contradicted by experimental data.

According to the standard model, all matter is composed of two basic types of particles, quarks and leptons, and their corresponding antiparticles. The quarks and leptons come in several varieties ('flavors'), as listed in Table 1.1. The standard model describes three forces (interactions) these particles experience: the electromagnetic interaction between charged particles and photons, described by Quantum Electrodynamics (QED)[1]; the weak interaction, which at low energy is responsible for radioactivity, and at high energy is unified with QED in the Weinberg-Salam $SU(2) \times U(1)$ model[2]; and the strong interaction between quarks and gluons, which causes the forces between nucleons, described by the $SU(3)$ gauge theory Quantum Chromodynamics (QCD)[3]. [1]

The subject of this thesis, hadronic jets and their properties, deals with the strong in-

[1] Gravity has not been incorporated into the model; however, at presently attainable energies, the gravitational interaction is of negligible strength in comparison with the others.

Table 1.1: Fundamental matter particles of the standard model.

QUARKS

				charge	
'down'-type quarks	d	s	b	$-\frac{1}{3}$	
'up'-type quarks	u	c	t	$+\frac{2}{3}$	(t not yet observed)

LEPTONS

				charge	
Charged leptons	e	μ	τ	-1	
Neutrinos	ν_e	ν_μ	ν_τ	0	(massless?)

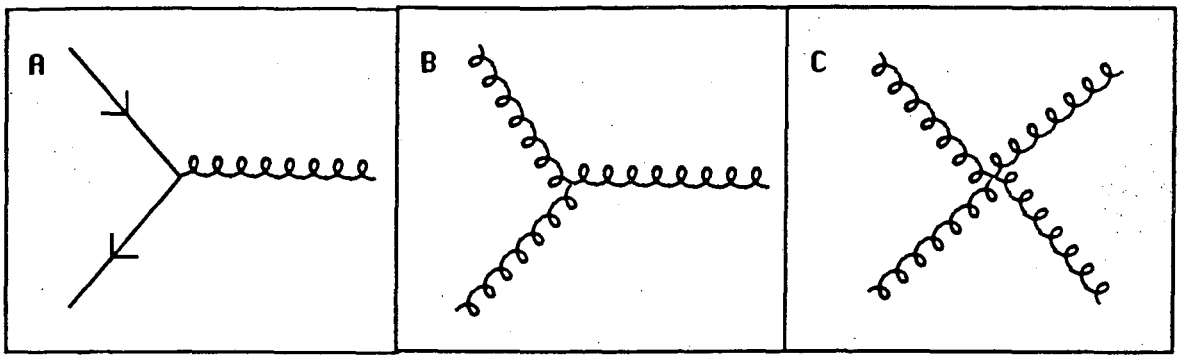

Figure 1.1: Interactions of quarks and gluons in Quantum Chromodynamics.

teraction. QCD is a renormalizable field theory similar to QED, in that quarks[2], which carry a different kind of charge called 'color', interact with gluons (analogous to photons in QED) via a Lagrangian similar in appearance to the QED Lagrangian. Unlike QED, the gauge symmetry is non-Abelian, causing gluons also to possess color charge and consequently interact with gluons as well as quarks. The basic interactions among gluons and quarks are the Feynman vertices shown in Figure 1.1. The additional gluon-gluon interactions cause the strong coupling constant $\alpha_s = g_s^2/4\pi$ to have a qualitatively different behavior with Q^2 (the interaction momentum transfer scale) than the QED coupling constant $\alpha_{QED} = e^2/4\pi$.

[2]For simplicity, both quarks and antiquarks will be referred to as quarks in this discussion.

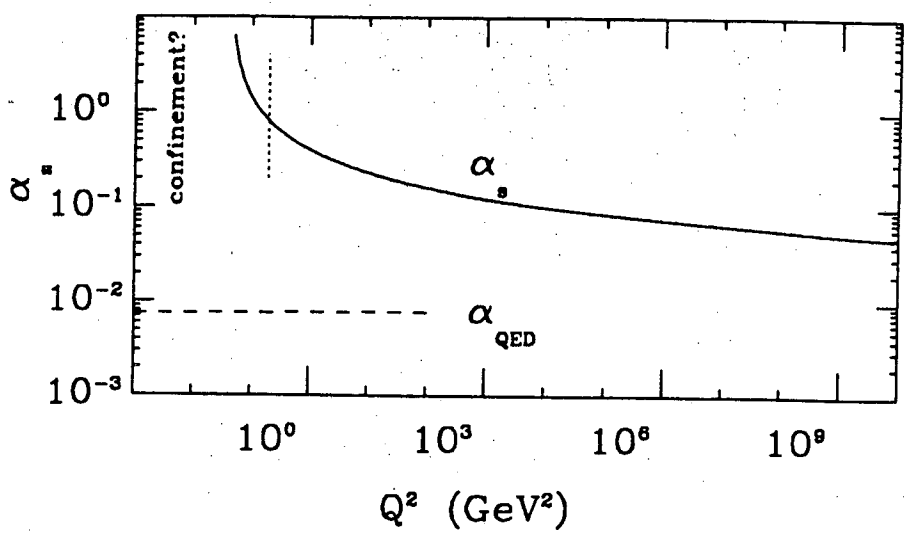

Figure 1.2: Q^2 dependence of the strong coupling constant α_s and the QED coupling constant α.

The Q^2 dependence of α_s, illustrated in Figure 1.2, is approximately

$$\alpha_s(Q^2) = \frac{4\pi}{(11 - \frac{2}{3}N_f)\ln(Q^2/\Lambda^2_{QCD})},$$

where N_f is the number of quark flavors with mass less than Q, and Λ_{QCD} is a constant, determined experimentally to be about 0.2 GeV.

The 'running' of the strong coupling constant causes the strong interaction to be very different at small versus large Q^2. In the infinite Q^2 limit, quarks and gluons are 'asymptotically free' particles, and the theory is well behaved. Below about (1 GeV)^2, however, the coupling becomes large and the techniques of perturbation theory can not be applied; it is believed that this causes the quarks and gluons to be confined into hadrons and not observable in isolation.

The confinement of color charge is responsible for the jet structure of high energy hadron collisions. Though for an instant a gluon or quark may be knocked out of a proton, as soon as it is separated by distances of the order of the proton size (approximately 1 Fermi), the potential energy becomes large enough to create quark-antiquark pairs from the vacuum. Rather than the outgoing quark, a group of hadrons travelling approximately in the original quark or gluon direction is observed. The observation of jets, first in e^+e^- collisions[4] and later in hadron collisions[5], provided strong evidence for the quark model

and QCD.

Prior to the advent of QCD as a dynamical theory, the 'parton model'[6] was proposed to describe nucleon substructure seen in deep inelastic scattering experiments. The 'structure functions' $F(X)$, describing the distribution of the nucleon momenta among various types of partons (quarks and gluons), appeared to be only a function of the momentum fraction X and to scale with the probing momentum transfer. Similarly, the 'fragmentation function' $D(Z)$ describing the momentum distribution of hadrons from an outgoing quark was assumed to be a function of the momentum fraction Z and independent of Q^2. Further, it was suggested that these functions could be used to describe a large variety of processes including deep inelastic scattering, e^+e^- annihilation, and hadron collisions.

The theory of QCD was later seen to support the basic parton model tenets as its lowest-order approximation; the exception is that the existence of a momentum scale (Λ_{QCD}) in the theory would necessarily introduce scaling violations (Q^2 dependence) in the fragmentation and structure functions. Since any 'hard' (high Q^2) process involving QCD includes also the 'soft' (low Q^2) region, higher orders always enter in, which can be absorbed into the fragmentation and structure functions. The Q^2 dependence acts to hinder the quantitative comparison of the different processes, because of ambiguity regarding the precise definition of Q^2 for a particular process.

1.1 Hadron Collisions

Jet production in proton-antiproton collisions in the QCD-improved parton model is illustrated in Figure 1.3. The incoming protons and antiprotons may be thought of as a broad-band parton beam, where the structure functions describe the effective luminosity of incoming gluons and quarks. The transverse momenta of the incoming partons is small compared with their momenta in the beam directions. Pairs of constituent partons with momentum fractions x_1 and x_2 collide with a subprocess cross section $\hat{\sigma}(\hat{s}, \hat{t}, \hat{u})$ appropriate to the parton species. The kinematic variables $\hat{s}$, $\hat{t}$ and $\hat{u}$ are defined (for massless partons)

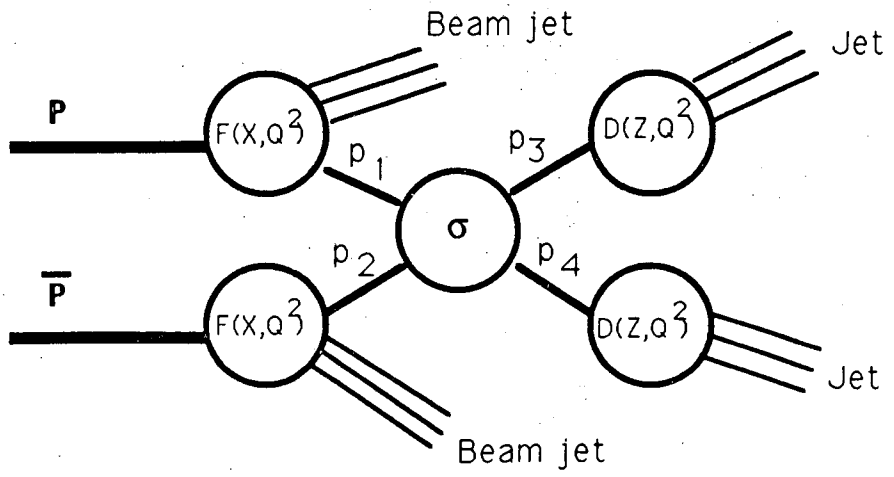

Figure 1.3: QCD improved parton model description of jet production.

by the relations:

$$\hat{s} = (p_1 + p_2)^2 = x_1 x_2 s,$$

$$\hat{t} = (p_1 - p_3)^2,$$

and

$$\hat{u} = (p_2 - p_3)^2.$$

The remnants of the incoming hadrons add an 'underlying event' background to the jets from the hard scatter.

The cross section for inclusive jet production in lowest order is obtained by summing over the parton subprocesses that contribute, weighted by the parton distributions and the subprocess cross sections. The calculated differential cross section versus transverse momentum (P_T) at the Tevatron center-of-mass energy $\sqrt{s} = 1.8$ TeV is shown in Figure 1.4, as calculated from the PAPAGENO program[7] using the EHLQ set 1 structure functions[8]. Between 20 and 100 GeV/c, the cross section decreases by several orders of magnitude, primarily a reflection of the structure functions, which are peaked at low X values. The predicted fraction of events as a function of P_T which are gluon-gluon, quark-gluon and quark-quark collisions is plotted in Figure 1.4b. The fraction of quark-quark scatterings is

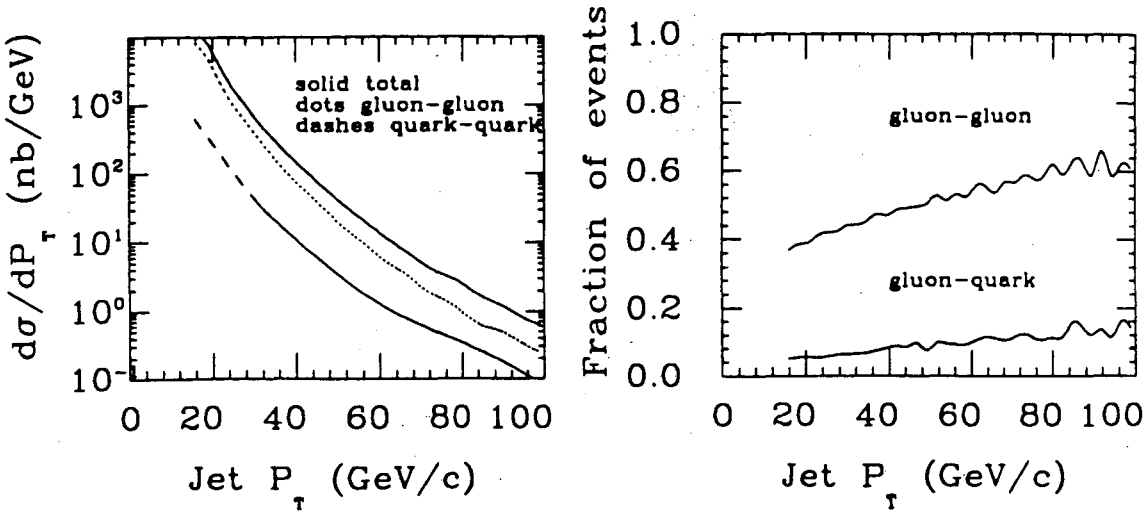

Figure 1.4: a) Cross section for QCD jet production in 1.8 TeV $\overline{p}p$ collisions. Also shown are individual contributions from quark-quark and gluon-gluon collisions. b) Fraction of gluon-gluon, quark-gluon and quark-quark events as a function of jet P_T.

only a few percent of events, rising slowly with P_T. The plot also shows that the outgoing jets in these collisions are expected to be approximately 75 percent gluon initiated.

1.2 Jet Fragmentation

The fragmentation properties of the jets should be entirely specified by QCD (with the exception of effects due to weak and electromagnetic decays), if QCD is indeed the correct theory of strong interactions. Fully understanding the phase transition in which hadrons are formed is beyond the capabilities of present mathematical techniques. The transition may not be very complicated; models have been developed, such as the string model[10] and the cluster models[11, 12], based on physical intuition, which describe fragmentation data reasonably well; But they do not tell us whether the QCD theory is right or wrong.

At higher and higher jet momenta, QCD is able to make more solid predictions about jet properties[13, 12]. As illustrated in Figure 1.5, the development of a jet can be schematically separated into four stages: the production of a parton in a hard collision, with a virtual mass on the order of the collision momentum transfer; perturbative evolution of the parton to a lower virtual mass ($\sim$ 1 GeV), through gluon *bremsstrahlung* and quark-

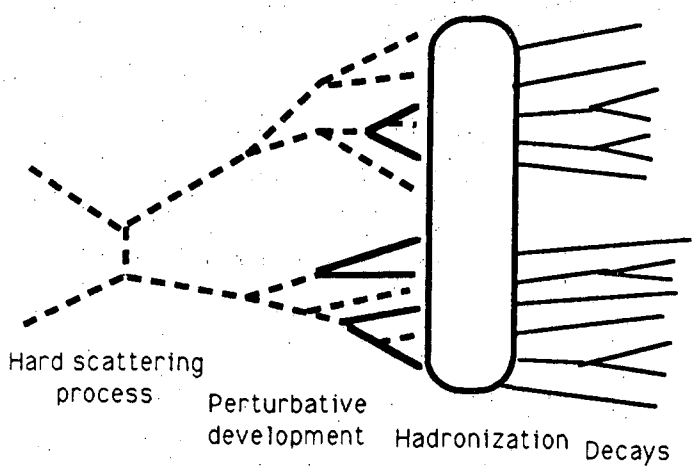

Figure 1.5: Schematic development of partons into jets of hadrons.

antiquark pair production; the transition into hadrons; and the decay of unstable hadrons. With increasing jet energy, as the tools of perturbation theory become applicable to a larger portion of the jet development, QCD is able to make two solid predictions:

- The fragmentation properties of quark jets and gluon jets should be different at high energy. The differences should asymptotically reach a maximum for infinite jet energy. For example, the ratio of average multiplicity in gluon versus quark jets was predicted to be 9/4 (the ratio of gluon to quark color charge)[14], with higher order corrections giving a value somewhat lower (~ 2)[15]. Equivalently, the fragmentation function for gluon jets should be 'softer' (more steeply falling), with more of the jets momentum taken up by low Z particles[13].

- For each type of jet, the fragmentation function should become more peaked at very low fractional momenta Z, with a correspondingly higher average multiplicity, as energy increases. The Q^2 dependence of the quark and gluon fragmentation functions (from measurements at a fixed Q^2 value) can be calculated from the Altarelli-Parisi evolution equations[19]:

$$\frac{\partial D_q(Z,Q^2)}{\partial \ln Q^2} = \frac{\alpha_s}{2\pi}\int_Z^1 \frac{dZ'}{Z'}[D_q(Z',Q^2)P_{qq}(\frac{Z}{Z'}) + D_g(Z',Q^2)P_{gq}(\frac{Z}{Z'})]$$

$$\frac{\partial D_g(Z,Q^2)}{\partial \ln Q^2} = \frac{\alpha_s}{2\pi}\int_Z^1 \frac{dZ'}{Z'}[\sum D_q(Z',Q^2)P_{qg}(\frac{Z}{Z'}) + D_g(Z',Q^2)P_{gg}(\frac{Z}{Z'})]$$

In the above formulae, D_q and D_g are the fragmentation functions for quark and gluon jets, respectively, and $P_{ab}(x)$ is the probability for a to split into b with momentum fraction x, calculated in QCD. The Altarelli-Parisi equations were originally applied to the structure functions.

Peterson *et al*[20] point out two other sources of non-scaling behavior in the fragmentation function (specifically in e^+e^- experiments). The first is nonperturbative phase space effects introduced by finite hadron masses and nonzero transverse momenta within the jet. These effects are expected to be negligible in comparison with perturbative evolution for P_T above $\sim$ 30 GeV/c. The other source is increased heavy (c and b) quark production. The fragmentation function of heavy quark jets into primary heavy hadrons is concentrated at high Z. The primary mechanism for heavy quark production at the Tevatron is gluon splitting (as opposed to s channel production) so their effect on the inclusive fragmentation function is not as dramatic as for e^+e^- jets.

The experimental evidence for differences between quark and gluon jets is not clear. In e^+e^- data, some studies have shown evidence for gluon jets fragmenting with higher average multiplicities[16], a steeper fragmentation function[17], or larger internal transverse momenta[18]. In general, these studies used asymmetric three-jet events to obtain a gluon enriched jet sample, and therefore compare the jets at different Q^2 values. By comparing symmetric three-jet events at $\sqrt{s}$ = 35 GeV with two-jet events at $\sqrt{s}$ = 22 GeV, TASSO has reported seeing no evidence of quark/gluon differences in the fragmentation function[21]. In $\overline{p}p$ collisions, the UA1 Collaboration compared the fragmentation of gluon and quark enriched jet samples, from different dijet kinematic regions[22]. Jets from the 'gluon' sample (at an average dijet invariant mass of 95 GeV/c^2) were observed to fragment more softly than jets from the 'quark' sample (which had an average dijet invariant mass of 130 GeV/c^2).

Chapter 2

Experiment Description

2.1 CDF Experiment Overview

The Collider Detector at Fermilab (CDF) is an ongoing experiment to observe collisions of protons and antiprotons at the highest center-of-mass energy available to date. The collaboration includes over two hundred physicists from the United States, Italy, and Japan[23]. Planning for the experiment began in 1978, and the first $\overline{p}p$ collisions were seen in October 1985 using a subset of the CDF apparatus. In March through May of 1987, the first significant amount of data was recorded with the nearly completed CDF experiment. The analysis presented in this thesis uses these data, which amount to approximately 26 inverse nanobarns of integrated luminosity at the center-of-mass energy $\sqrt{s} = 1.8$ TeV. In the past year the experiment has recorded over 4 inverse picobarns, more than a factor of 100 increase over the 1987 sample, allowing for high statistics studies of previously rarely observed phenomena and a larger energy range in which to search for "new physics". Additional runs with an upgraded detector at higher luminosity are planned for the near future.

CDF is a general purpose collider detector, in which the goal is to measure the features of $\overline{p}p$ interactions in as much detail as feasible. The detector is shown in an isometric view in Figure 2.1. The various subsystems are designed to detect most standard model objects or their decay products. These subsystems include:

- tracking detectors for non-destructive measurement of charged particle momenta in a 1.5 Tesla solenoidal magnetic field.

- finely segmented calorimetry for measuring energy and direction of single particles

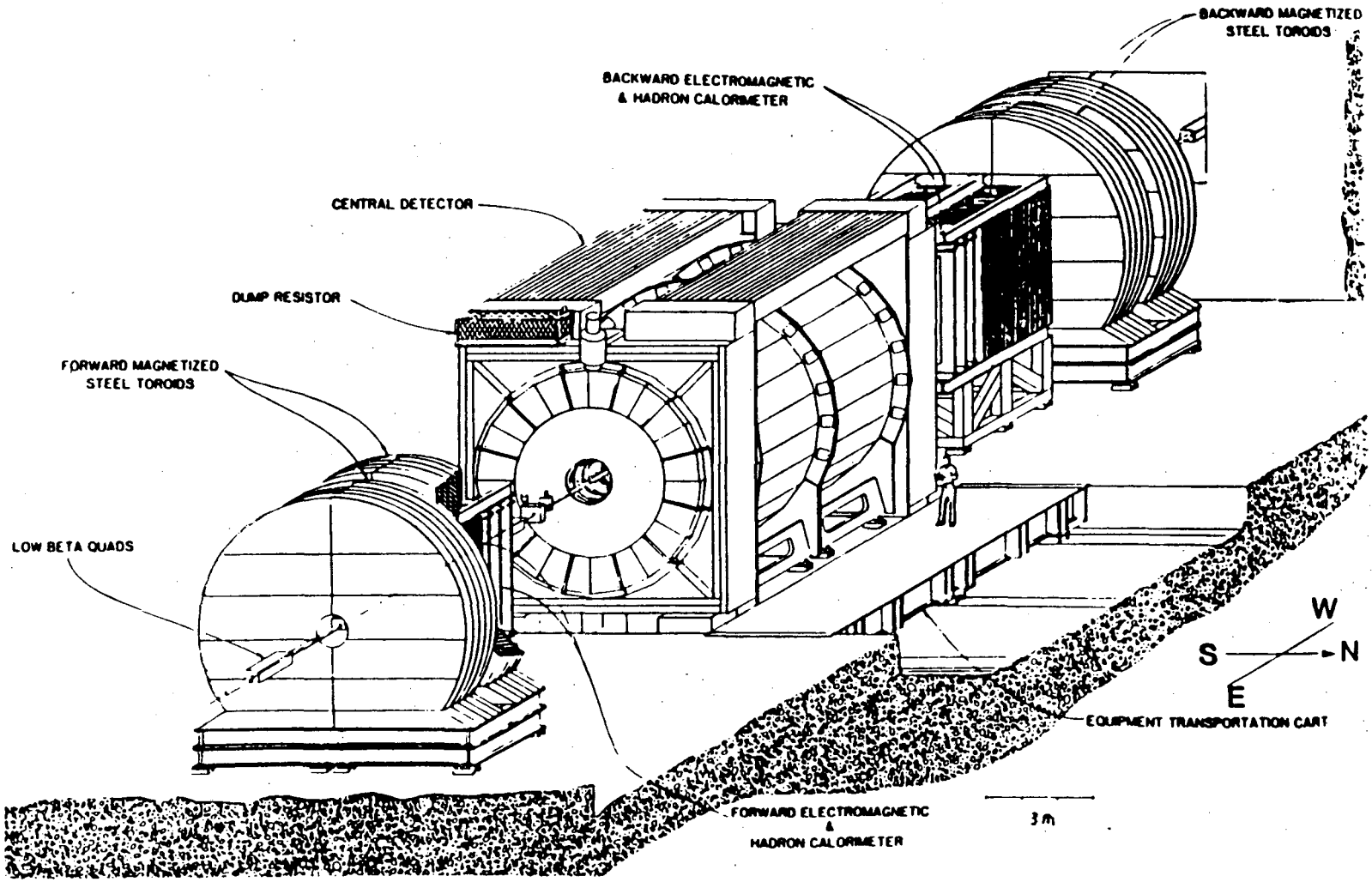

Figure 2.1: The CDF experiment

(hadrons, electrons or photons) or jets of particles via total absorption. As the calorimetry covers nearly the complete 4π solid angle, non-interacting particles such as neutrinos can be "detected" in events with substantial transverse momentum imbalance.

- chambers outside the calorimetry for detection and momentum analysis of muons.

A flexible multi-level trigger system enables the experiment to collect several sets of data with more or less complicated criteria based on the detectable objects mentioned above. These can be analyzed independently to investigate many different physics topics. In this sense the experiment may be thought of as a laboratory in itself.

In the following sections, the accelerator and those detector components that are relevant to this work will be described, which include the tracking detectors, the calorimetry, and the data acquisition and trigger systems. The complete CDF apparatus is described in detail in [24] and references contained therein. An orthogonal coordinate system is utilized in which x, y and z are the distance in horizontal direction outwards from the center of the accelerator ring, the vertical direction, and in the proton beam direction, respectively. ϕ is the azimuthal angle, and θ is the polar angle to the proton beam direction. Transverse momentum P_T or energy E_T are simply the momentum or energy multiplied by $\sin\theta$. An additional useful variable is the pseudo-rapidity η defined by the relation $\eta \equiv -\ln\tan(\theta/2)$.

2.2 Tevatron Collider

The CDF experiment is located at the B0 interaction region of the Fermilab Tevatron Collider[25]. The Tevatron is presently the world's highest energy accelerator and the first to extensively utilize superconducting magnet technology. The Tevatron is the final component of an accelerator complex which includes:

- A linear accelerator for the preacceleration of protons from hydrogen gas.

- An antiproton storage ring which utilizes the principle of stochastic cooling[26] to collect up to 10^{10} antiprotons per hour.

- The Main Ring which accelerates bunches of protons and antiprotons to 120 GeV for injection into the Tevatron. The Main Ring occupies the same tunnel as the Tevatron and passes directly above the CDF detector. It is used during Tevatron operation to collide protons on a target for production of antiprotons.

The antiprotons and protons are injected in bunches of typically 10^{11} particles, which are accelerated using RF cavities. In 1987 the Tevatron was operated with three bunches each of antiprotons and protons, which intersected each other within the detector every seven microseconds. A pair of focusing quadrupole magnets located on each side of the CDF detector squeeze the beam to maximize the luminosity.

The luminosity $\mathcal{L}$ is expressed in units of flux per area per unit time, and is used to calculate the rate $\mathcal{R}$ for a process with a cross section area σ by the relation:

$$\mathcal{R} = \mathcal{L}\sigma$$

The peak luminosity achieved in the 1987 running period was $10^{29}/\mathrm{cm}^2/\mathrm{sec}$, which resulted in a basic inelastic collision rate of about five kiloHertz. The collisions occurred in a spatial region of approximately 60 microns RMS in radius by 30 centimeters RMS in length.

2.3 Tracking Detectors

Within CDF there are four separate detectors for charged particle tracking: The Vertex Time Projection Chambers (VTPC), the Central Tracking Chamber (CTC), the Central Drift Tubes (CDT), and the Forward Tracking Chamber (FTC). The latter two were not used for this analysis and will not be described here. The VTPC, CTC and CDT are located inside a superconducting solenoid. The coil, manufactured by Hitachi, Inc. of Japan, has dimensions of five meters in length and three meters in diameter. The magnetic field is 1.5 Tesla oriented along the beam axis with nonuniformity of less than approximately two percent in magnitude and direction throughout the tracking volume. The coil is constructed of NbTi/Cu superconductor, and contributes 0.86 radiation lengths (at normal incidence) in front of the calorimetry.

2.3.1 General Tracking Principles

The CDF tracking detectors are conventional gas drift chambers. In such a device charged particles travelling through the gas volume leave a trail of ionization. The average energy lost in creation of electron-ion pairs (given by the Bethe-Bloch formula[27, 28]) reaches a minimum for velocity $\beta \sim 0.8c$, and rises very slowly for more relativistic particles. Singly charged high momentum particles therefore leave a similar ionization signal as minimum ionizing particles, nearly independent of mass. Local fluctuations from the average energy loss caused by single small impact parameter collisions are known as Landau fluctuations.

The ionization electrons and ions then drift under the influence of applied electric (E) and magnetic (B) fields. The electron drift velocity and trajectory depend on properties of the gas (in particular, the mean time between collisions) and the magnitude and relative orientation of the E and B fields. If they are parallel, as is the case for a time projection chamber, the electrons drift along them; otherwise they move at an angle to the E field direction called the Lorentz angle.

The electrons first drift through a region of uniform fields, experiencing diffusion along and perpendicular to the direction of drift, before being collected at the sense wires. In the drift region the drift velocity is constant, so the distance from the track to the wire is obtained from the time of the pulse as $\Delta d = v_{drift}\Delta t$. Depending on the gas and fields used, the drift velocity may be sensitive to the gas density. If not, the drift velocity is said to be saturated. Positive ions drift so slowly that they are not collected as signal, but may cause field distortions if their density is large enough.

The electron signal is amplified very close to the sense wires by avalanche multiplication. This occurs when the local electric field is strong enough to accelerate electrons to the necessary energy to ionize other gas molecules. The amplified signal will be proportional to the initial ionization (proportional mode) if the field near the wire is low enough to keep the avalanche small. The time, and in some cases the amplitude, of the avalanche signal on the sense wire are amplified, digitized and recorded.

The charged tracks are then reconstructed from these 'hits'. In the CDF case of a

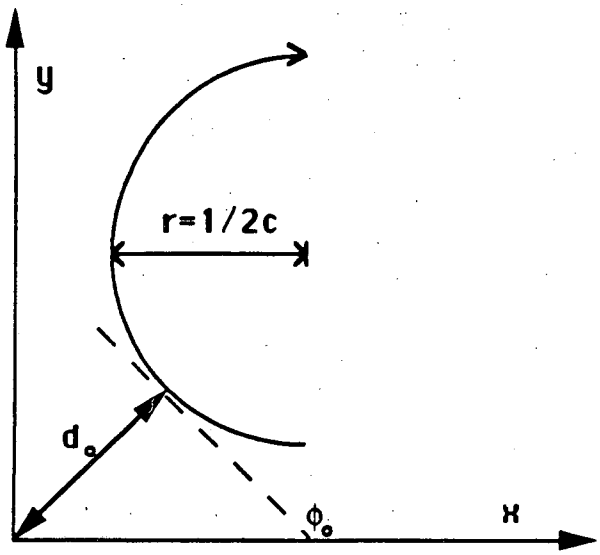

Figure 2.2: Track parameters defined

constant B field along the beam axis, the tracks follow a helical trajectory with the radius proportional to the particle's transverse momentum:

$$r_{curv}(\text{cm}) = \frac{P_T}{|q|B} = \frac{333.56}{1.515} P_T \ (\text{GeV}/c)$$

based on a fit to the reconstructed track, five parameters are obtained which describe the trajectory in three dimensions. As illustrated in Figure 2.2, they are:

- the half curvature: $c = q/2r_{curv}$.
- the azimuthal angle at closest approach to the beam: $\phi_0 = \tan^{-1}(P_y/P_x)$.
- the impact parameter: d_0. This is the radial distance of closest approach to the beam, and may be positive or negative, depending on which side of the track the beam spot is located.
- the cotangent of the polar angle: $\cot\theta = P_z/P_T$.
- the z coordinate at closest approach: z_0.

The correlations between these fit parameters are contained in the 5×5 covariance matrix, the diagonal elements of which are the squared fit errors of the individual parameters given the assumed position resolution.

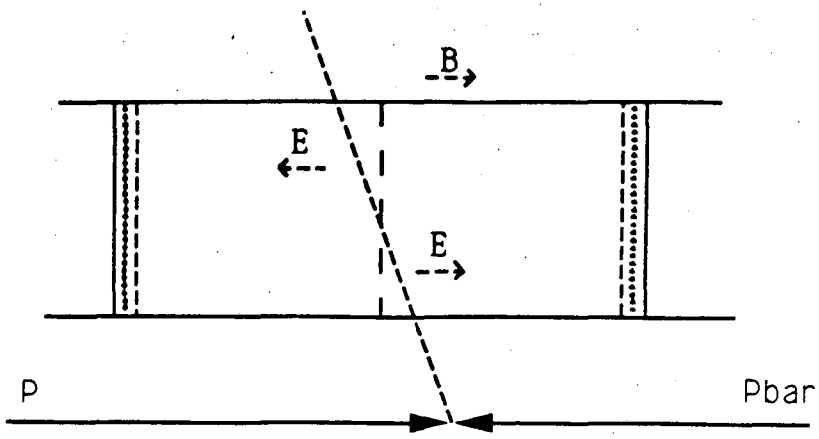

Figure 2.3: Side view of a VTPC module.

Table 2.1: VTPC design parameters.

VTPC Specifications:	
Number of modules	8
Inner radius	7 cm
Outer radius	21 cm
Sense wires	24 /octant
Sense wire spacing	6.336 mm
Drift length	15.25 cm
Drift E field	256 v/cm
Drift velocity	42 mm/usec
Max drift time	3.6 usec
Gas: 50/50 Argon-Ethane	

2.3.2 Vertex Time Projection Chambers

The VTPC are 8 octagonal time projection chamber modules situated immediately outside the beam pipe, covering the angular range $3.5° < \theta < 176.5°$ ($|\eta| < 3.5$). Some details of the VTPC construction are listed in Table 2.1. Each module consists of two 15 centimeter drift regions separated by a central grid, as shown in Figure 2.3. Ionization electrons drift in a uniform electric field parallel to the magnetic field and are detected by a plane of 24 sense wires at the end of the modules.

The VTPC measure a track's z coordinate with approximately 0.5 millimeter resolution, and the slope dr/dz. In the VTPC, information on the ϕ direction of tracks is limited.

Table 2.2: CTC design specifications.

Wire length	3214 mm
Innermost sense wire radius	309 mm
Outermost sense wire radius	1320 mm
Number of sense wire layers	84
Number of superlayers	9 total (5 axial, 4 stereo)
Cells per superlayer	30,42,48,60,72,84,96,108,120
Sense wires per cell	12, 6,12, 6,12, 6,12, 6, 12
Cell tilt angle	45°
Sense wire spacing	10 mm
Drift field	1350 V/cm ± 1.5% (rms)
Gas	Argon-Ethane-Ethanol (49.6%:49.6%:0.8%)

For low angle tracks ϕ is obtained by fitting tracks between modules tilted at a 11.3° stereo angle. The main purpose of the VTPC system is to locate the primary event vertex, which is accomplished with a precision of approximately 0.1 millimeter. The VTPC are also used to identify multiple collision vertices in the same bunch crossing.

2.3.3 Central Tracking Chamber

The Central Tracking Chamber is a large cylindrical drift chamber which occupies the volume between the VTPC and the solenoid coil. The primary purpose of the CTC is to measure the momenta of charged tracks with high efficiency and precision. It is also used for selecting electron or muon candidates at the trigger level with hardware track processors, and rejecting backgrounds to electrons by requiring consistency between energy and position measured in the calorimetry with track momenta from the CTC. As the CTC plays a key role in jet fragmentation analysis, it will be described in some detail, and further sections will discuss such issues as pattern recognition, track finding efficiency and resolution. Several important design parameters of the CTC are listed in Table 2.2.

The CTC covers the interval $|\eta| < 1$. Within this range a particle's trajectory is measured by 84 sense wire layers located between 31 and 132 centimeters radius from the beam line. These layers are grouped into nine superlayers which are further subdivided into cells to aid in local pattern recognition. Five axial superlayers are made up of 12 sense wire

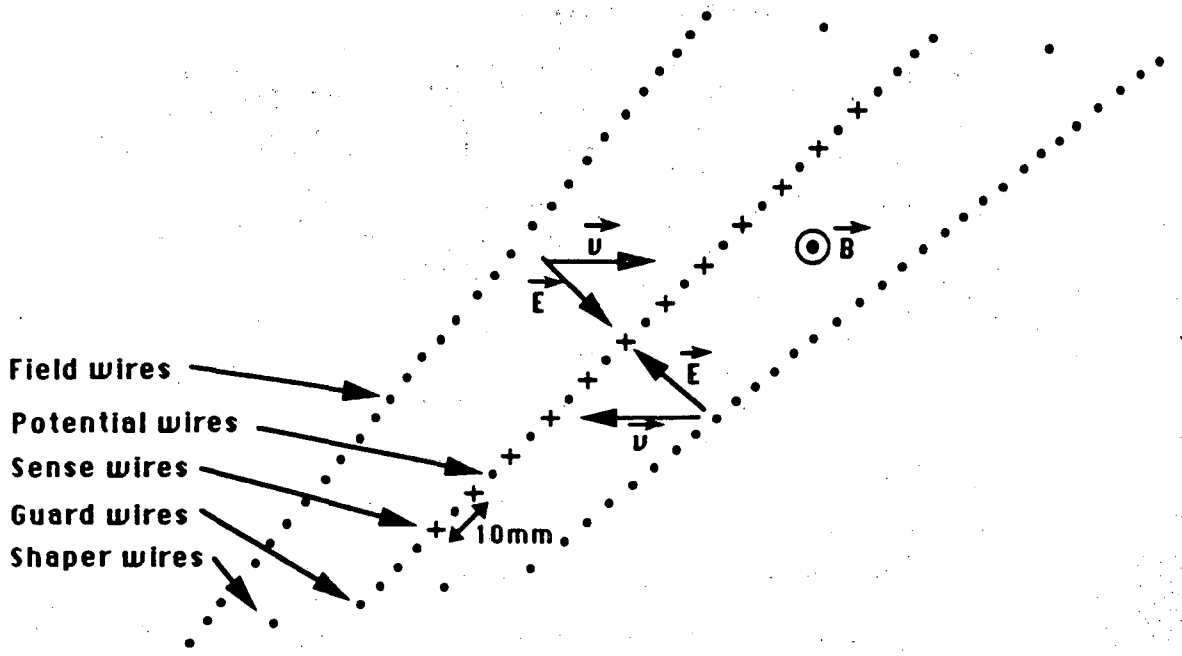

Figure 2.4: Axial superlayer cell geometry

layers that are parallel to the beam, providing information in the $r - \phi$ plane. Alternating with these are four stereo superlayers tilted by $\pm 3°$ with respect to the z direction with 6 sense wire layers each. The polar angle θ is obtained by matching hits of the stereo and axial layers.

The cell geometry is nearly constant in all axial or stereo superlayers, with the number of cells increasing from superlayer 0 (the innermost) to 8. A typical axial cell is shown in Figure 2.4. The plane of alternating sense and field wires is tilted by 45° to the radial direction. This orientation accomplishes three purposes:

- The electric and magnetic fields give a Lorentz angle of nearly 45° for the gas used, causing the electrons to drift in the azimuthal direction. The azimuthal drift simplifies the track reconstruction, and maximizes the uniform drift region by reducing dead space at cell edges.

- It is not known a priori from which side of the plane a given hit originates, so in addition to the real track there is a ghost track. The left/right ambiguity is easily solved since the ghost track is in most cases at an oblique angle, and does not match

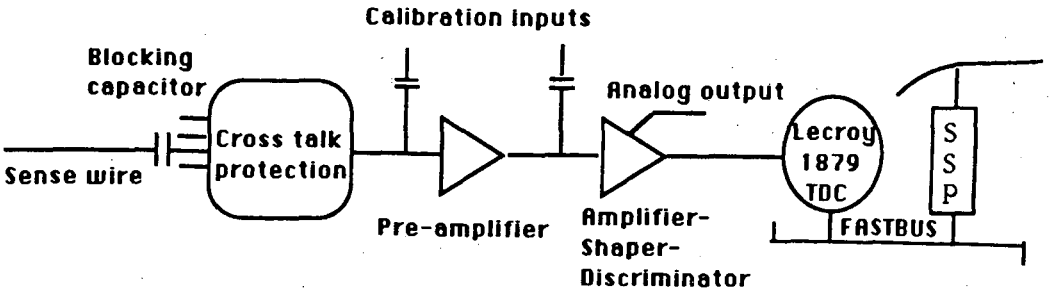

Figure 2.5: CTC read-out electronics

with track stubs in other superlayers.

- If a track has substantial P_T it will cross a sense wire plane in each superlayer producing a hit with a short drift time. These are useful for triggering and in pattern recognition.

With the field configuration chosen, the drift velocity in the gas is saturated at 5.1 centimeters/microsecond, so the velocity and the Lorentz angle are not affected by small variations from nominal conditions.

The electronics used to read out the sense wire hits are depicted in Figure 2.5. The signals are first amplified by hybrid preamplifiers which are a.c. coupled to the sense wire across a blocking capacitor and mounted directly on the CTC endplates. Cross talk from one wire to another caused by ion motion is cancelled by a passive compensation network at the preamplifier input. The signals go via ten meters of coaxial cable to Amplifier-Shaper-Discriminator (ASD) cards located on the outside of the CDF detector. The ASD output is a digital pulse, which travels 70 meters to the counting room, where the time and width are digitized by LeCroy 1879 FastBus TDC modules. The TDC's have a dynamic range of 512 nanoseconds in one nanosecond units, and can record up to 8 hits per wire on 96 wire channels per TDC module. The data in a crate TDC's are then read out and reformatted by a SLAC Scanner Processor (SSP) module[29].

The position resolution at each sense wire is approximately 200 microns or slightly less. This precision is determined primarily by the gas mixture and electric field and secondarily

by the cell geometry. For stereo sense wires the resolution in the z coordinate is (200 microns/sin 3°) or four millimeters. The CTC two track capability is approximately five millimeters, due primarily to the inter-wire spacing and the read-out electronics.

2.3.4 CTC Track Reconstruction

The raw data from the CTC are a list of wire addresses, hit times and widths, not all of which are associated with charged particles. The tracks used for physics analysis are obtained in the offline reconstruction, a complicated and CPU intensive process. It is useful to understand at a basic level how the reconstruction program works, in order to see where systematic effects from the hardware and software can influence the physics results. The track reconstruction algorithm is described in Appendix A.

2.3.5 Tracking Simulation

Detector simulation is an important part of CDF data analysis, as the simulation embodies what is understood about the detector - what effects are important and which approximations are valid - and allows the study of acceptance issues. Two different simulation programs have been used for various purposes in this analysis. One is a full detector simulation (CDFSIM) where raw hit data are generated which then needs to be reconstructed. The full simulation and track reconstruction is very CPU time consuming, so an alternate tracking simulation within the QFL program has also been used which directly generates tracks from particles taking into account detector resolution.

In the CDFSIM program, generated particles are propagated through the CDF detector, starting from a specified or randomly chosen vertex . Each subsystem may be enabled or disabled, but the effects of interactions in the material will still be simulated. Within the CTC a particle is moved in short steps past each sense wire. At each step it may decay producing other particles, suffer multiple scattering or create delta rays. Hadronic interactions in the CTC walls or VTPC are also simulated. If a low P_T particle spirals in the detector it is only followed for 2.5 turns, so the simulated events are 'cleaner' in this

regard than the actual data.

Hits are generated for each sense wire a particle traverses and stored in the raw data bank. In doing so, the positions are degraded by Gaussian detector resolution of 200 microns, and can be lost due to inefficiency or overlap with other hits. A perfect linear drift-time relation is assumed by default, and the track reconstruction program does not correct for this in Monte-Carlo runs. For reconstructing simulated data as real data, a feature has been added to apply drift time corrections in reverse for simulation. A record is kept of which hits correspond to which generated particle for testing pattern recognition using Monte-Carlo data. The CTC simulation within CDFSIM has been used for estimating track finding efficiencies and checking resolutions.

The faster QFL simulation is similar in design, but makes larger steps, simulates the most important effects only, and does not generate raw data. For many purposes this is sufficient. The CTC simulation creates a track for each particle which penetrates two or more superlayers and degrades the track parameters with nominal detector resolutions. In comparing QFL tracking simulated events to data tracking efficiency must be taken into account separately.

2.3.6 Performance

In the first operation of the CTC during the 1987 run, there were several problems, which were not observed to seriously affect the quality of the data as a whole:

- A set of Uranium bars outside the coil caused enough radiation in the CTC to necessitate reducing some voltage. The radiation also caused large pulses which would cause some electronics to oscillate, spoiling any event which happened to overlap. These 'noise burst' events are easily recognized and filtered out in the analysis.

- On about 1% of jet triggers, one or more SSP buffers would fill up and lose data. Usually this was in coincidence with electronic noise but was observed to happen on some very high multiplicity events.

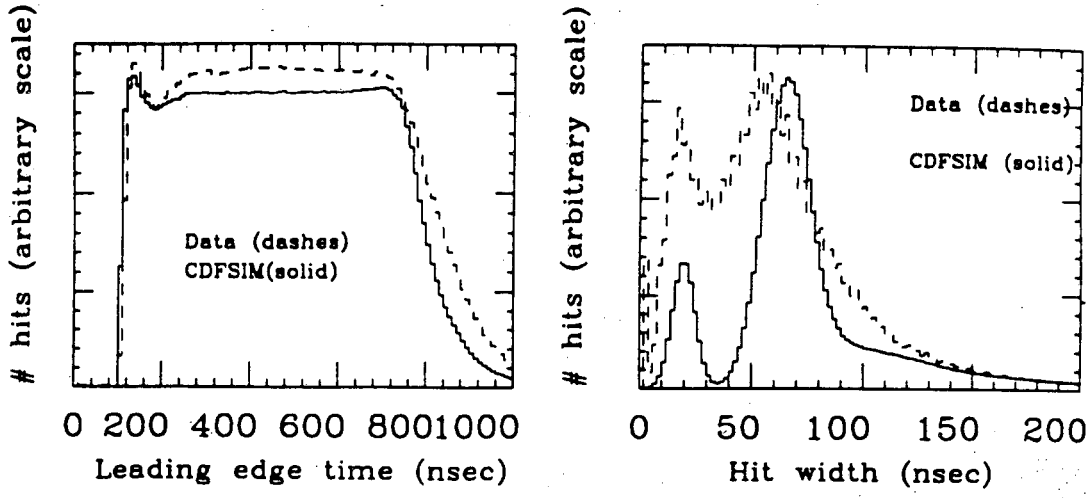

Figure 2.6: a) CTC leading-edge hit times in data and simulation. b) CTC hit widths in data and simulation.

- One fourth of the outer superlayer and two cells in superlayer 4 were not operating due to high voltage problems.

The hit leading-edge times and widths for all wires are shown in Figure 2.6 and compared with the CDFSIM simulation. The hit time distribution has a flat plateau corresponding to the uniform drift region, falling off at large times due to the changing cell width, and has a bump at low times due to nonlinearity in the time-to-distance relation for crossing hits near wires. There are two peaks in the hit width distribution corresponding to real hits and noise pulses, and a long tail from large angle tracks and hit overlap. The simulation and data do not agree very well in the width of real hits.

Figure 2.7 shows a dijet event in the CTC $r - \phi$ view. Energy depositions in the central calorimeter surround the CTC data. The tracks which have been reconstructed are listed. Charged particles with P_T less than 400MeV/c curl up in the CTC and are not found efficiently. A large number of hits, caused by these spirals or by noise, are not associated with tracks which were found. The most notable feature of the diagram is the high local multiplicity in the two jets which can cause confusion in the pattern recognition and degraded efficiency and resolution.

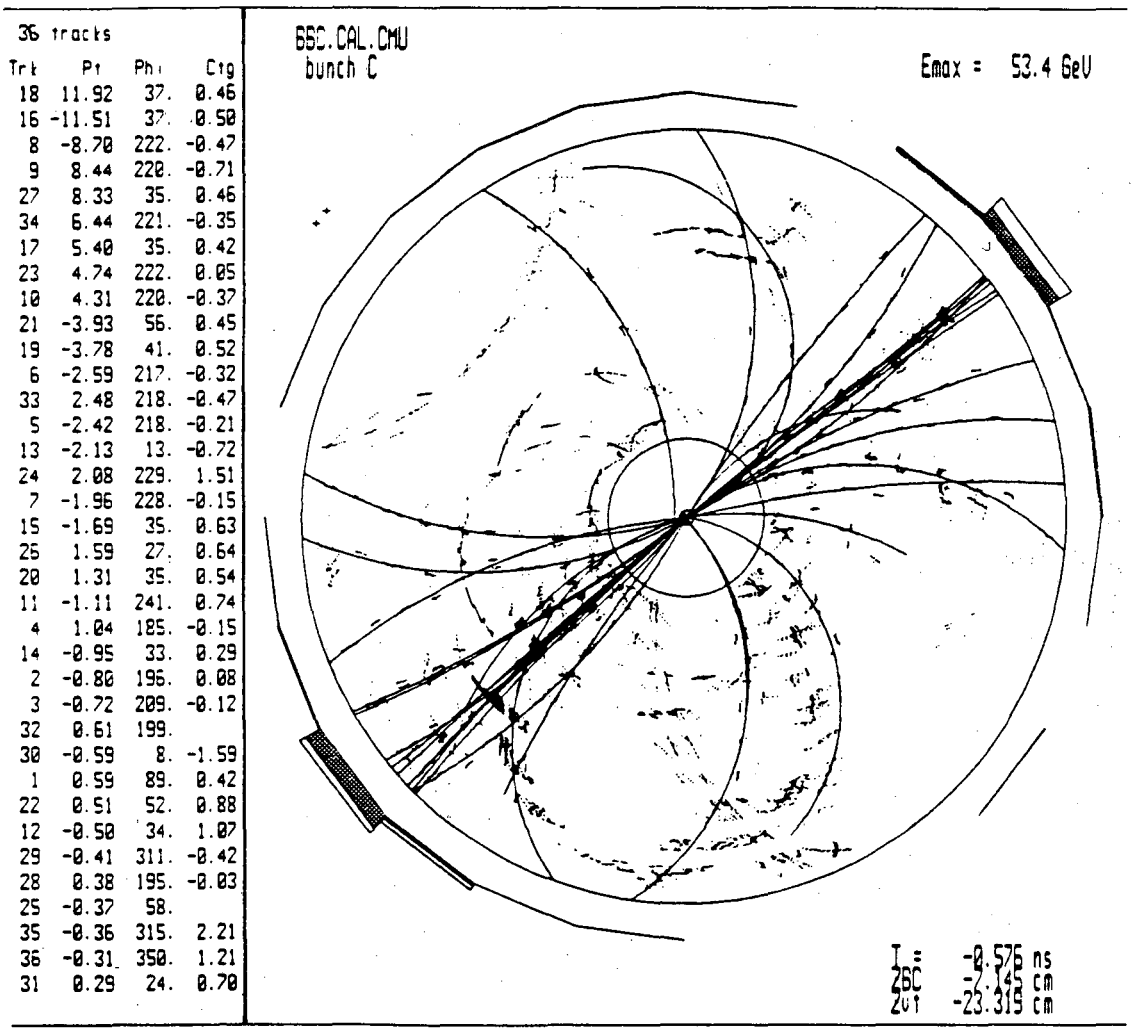

Figure 2.7: CTC view of a dijet event.

2.3.7 Track Selection Criteria

Tracks found by the reconstruction program are required to pass a set of selection criteria in order to be used. The criteria were chosen to reject (as much as possible) false or poorly measured tracks without incurring substantial loss in efficiency. Figures 2.8a through 2.8e show the distributions of the variables with the cuts indicated. For comparison, the equivalent distributions from CDFSIM are also shown. The criteria are as follows:

- Tracks must be found in three dimensions.
- Impact parameter cut : $|d_0| < 0.5$ cm. Only tracks from the primary event vertex are of interest for the fragmentation analysis.
- Delta z cut: $|z_0 - z_{event}| < 5.0$ cm.
- Fraction of possible hits used in the fit $> 50\%$.
- RMS residuals for axial and stereo hits < 900 and 800 microns, respectively. The residual distributions (Figures 2.8d and 2.8e) have long tails due to hit misassociation in the data that are not reproduced well in the simulation.

The fraction of tracks rejected by each of the above criteria is plotted in Figure 2.8f.

2.3.8 Track Finding Efficiency

A key element to the physics analysis is the tracking efficiency. The tracking efficiency is defined as the probability of finding a track which passes selection criteria in the region of complete CTC acceptance, including charged pions and kaons which decay before or within the CTC volume. In minimum-bias events the tracking efficiency was observed to be nearly 100% independent of multiplicity. This is to be expected since in these events particles tend to be well isolated and if not then the magnetic field bends them apart. In jets the tracking efficiency falls substantially below unity due to high track density in a small region in ϕ within the chamber.

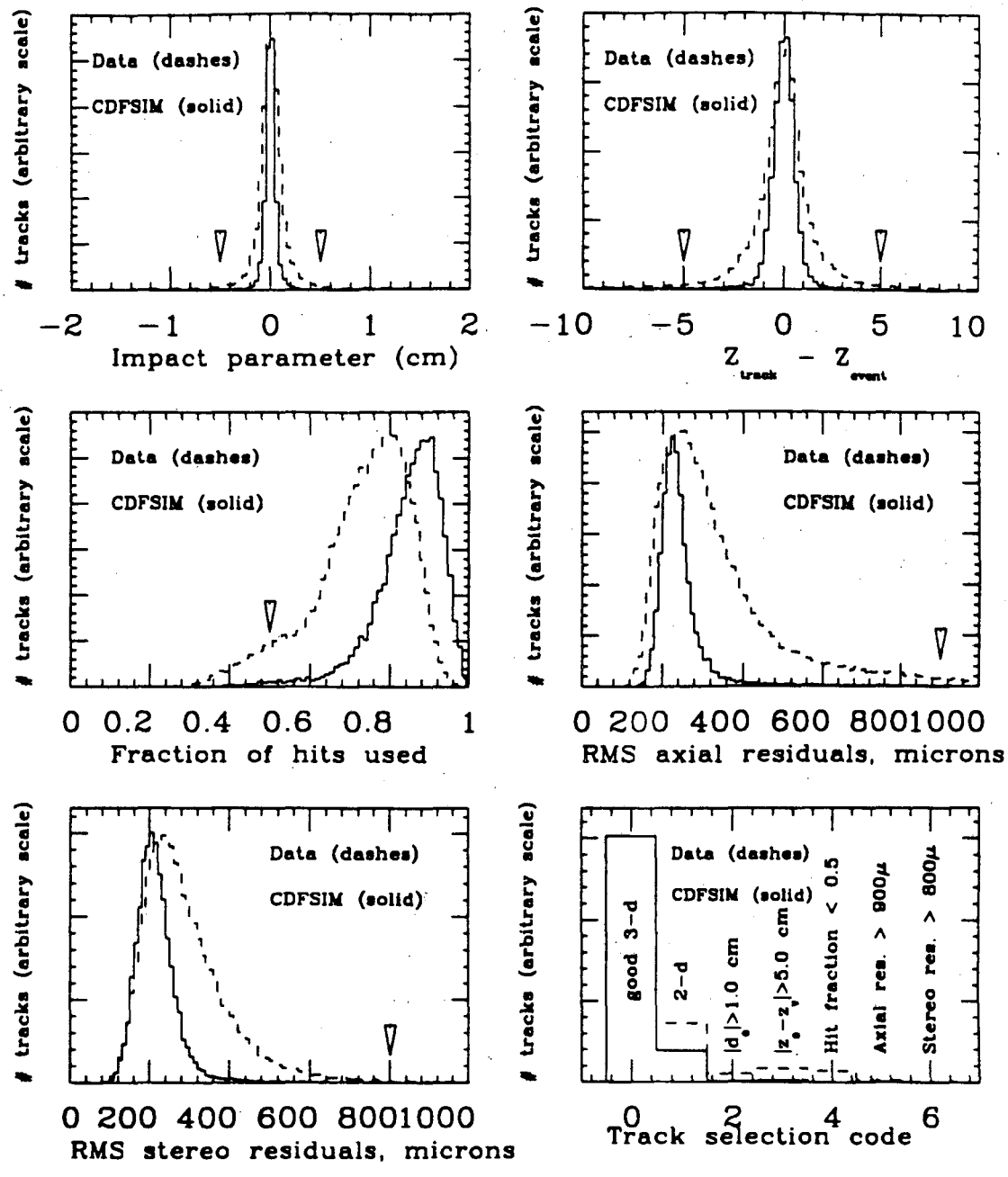

Figure 2.8: a) Track impact parameter distribution. b) Δz to event vertex. c) Fraction of possible hits per track. d) RMS axial hit residuals. e) RMS stereo hit residuals. f) Fraction of 'good' tracks and tracks that fail the various selection criteria.

Three techniques have been used to estimate the track finding efficiency within jets. These are described in detail in Appendix B. They are :

- Track merging. With jet data from the CTC as background, single simulated tracks were added with limited $P_\perp$ to the jet axis and the events were reconstructed as data. How often the tracks were found as a function of several variables was then tested. The track merging method is very CPU intensive, since an entire event was reconstructed to obtain a single test of efficiency. Also, since the modified events were more dense than data, the method is expected to provide a pessimistic estimate. In addition, the interpretation of the 'physics' variables (the fractional momentum Z of the track, for example) is ambiguous.

- Monte-Carlo event simulation. Monte-Carlo dijet events were generated, simulated and reconstructed. The efficiency was tested for each charged particle associated with a jet. The efficiency estimate from this method ought to be somewhat optimistic, since the detector simulation is 'cleaner' than the real data.

- Jet data. The fraction of tracks which were probably real tracks but failed track selection criteria for one reason or another was measured. This method served as a rough cross check of the other two.

The Monte-Carlo and track merging methods gave estimates which agreed reasonably well with each other. The estimated tracking efficiency is shown in Figure 2.9a as a function of the average distance in the $r - \phi$ plane to the nearest track in the event. The track merging and Monte-Carlo methods both show that the efficiency falls when the average distance between tracks is less than two centimeters. If two tracks are very close in $r - \phi$ throughout the CTC, then they are probably in the midst of a jet, so this is not a really a measure of the CTC's two track separation capability. Figure 2.9b shows the efficiency estimated as a function of the rapidity of a track to the jet, for two intervals of dijet invariant mass. The efficiency is observed to depend both on the rapidity and the invariant mass in a correlated manner.

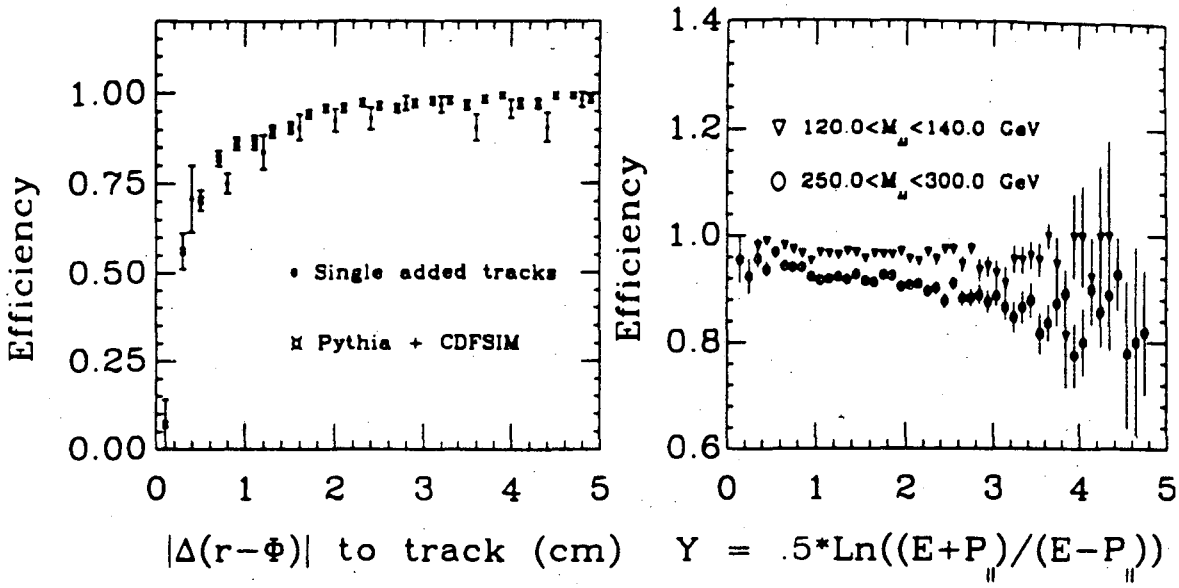

Figure 2.9: CTC track finding efficiency within jets. a) The efficiency evaluated as a function of average distance in the $r-\phi$ plane to the nearest track, from the track merging and Monte-Carlo studies. b) The Monte-Carlo efficiency evaluated as a function of the track rapidity to the jet axis, for two intervals in dijet invariant mass.

2.3.9 CTC Track Resolution

The CTC measures the curvature of a track (or equivalently, its sagitta) in order to determine the transverse momentum. Measurement errors of the curvature are Gaussian distributed, and are independent of the curvature if multiple scattering is neglected. Consequently:

- The relative precision in terms of momentum worsens linearly with increasing momentum :

$$\frac{\delta P_T}{P_T} \propto \frac{P_T}{B} \times \delta c$$

- The momentum errors are asymmetric. Tracks can fluctuate further upwards in measured P_T than downwards.

The curvature and angular resolutions of a tracking detector caused by measurement uncertainties and multiple scattering are discussed in a paper by Gluckstern[30]. In that paper, the resolutions in those quantities is calculated from the estimated hit position uncertainties, assuming the curvature and angles are determined by a least squares fit.

Assuming the hit position uncertainties are uncorrelated with each other, the following relation was derived for the curvature resolution from N equally spaced measurements with precision ϵ over a track length L:

$$\delta c \simeq \frac{\epsilon}{L^2}\sqrt{\frac{720}{N+5}}$$

Thus the momentum precision of such a detector is predicted to improve as $1/BL^2$.

Multiple scattering in the gas or material introduces wire-to-wire correlated deviations from an ideal helical trajectory. The effect of multiple scattering is to give a momentum 'kick' to a track. Thus it is only important at low track momenta, and dominates the CTC resolution for momenta below one GeV/c.

Vertex constrained fits

In the case where a particle originates from the primary event vertex, including this information as a vertex constraint in the fit adds 30 centimeters to the track length. The additional length should correspondingly diminish the curvature errors by a factor of typically $(100/130)^2$ or 0.6. The assumption that a track comes from the primary vertex is in most cases true if the measured d_0 and z_0 match the vertex within their resolutions.

For primary track candidates passing the selection criteria, the vertex constraint was imposed as a separate step from the original fit. The true beam x and y positions were used, which varied linearly with z of the event vertex up to two millimeters offset from $x = y = 0.0$, with an estimated uncertainty of 60 microns. The two constraint equations $d_0 = 0.0$ and $z_0 = z_{event}$ were imposed using the Lagrange multiplier technique[32], and an improved set of fit parameters and covariance matrix were calculated from the unconstrained fit parameters and covariance matrix.

Monte-Carlo results on resolution

The actual resolution with which a track is measured depends on many factors, including the density of nearby tracks and the effects dead cells have on a track. The resolution for tracks within jets was investigated for this work using simulated tracks merged with data

(Appendix B). As in the efficiency study, a track was identified with the inserted track if it contained greater than 25 percent of the simulated hits. If a track was identified and passed the track selection criteria, its parameters were compared with the generated parameters.

The distribution of $\Delta(1/P_T)$ between the reconstructed and generated tracks is shown in Figures 2.10a and b before and after imposing the vertex constraint. Inserted tracks were within the momentum range $10 < P_T < 20$ GeV/c. As expected, the addition of the vertex constraint improved the resolution by nearly a factor of two. There were a small number of tracks well separated from the central peaks of the distributions, suggestive of a non-Gaussian 'tail' to the track curvature resolution. However, interactive scanning of these tracks revealed that they were caused by misidentification of the simulated track among the real tracks in the event.

The r.m.s. $1/P_T$ resolution is plotted as a function of P_T in Figure 2.11. The estimated resolution for vertex constrained tracks is parametrized:

$$\frac{\delta P_T}{P_T} = P_T \delta(\frac{1}{P_T}) = \sqrt{(0.0015 P_T)^2 + (0.004)^2}$$

The 0.004 term is due to multiple scattering. At high momentum, the resolution is approximately $\delta P_T/P_T \simeq 0.15\% P_T$. The three curves show this resolution and upper and lower estimated uncertainties on the resolution.

2.4 Calorimetry

The CDF calorimeter measures particle energies with almost complete azimuthal coverage in the pseudo-rapidity range $|\eta| < 4.2$ ($2 < \theta < 178°$). The calorimetry is divided in depth into separate electromagnetic and hadronic compartments. Different pseudo-rapidity ranges are covered by four subdetectors:

- Central electromagnetic calorimeter ($|\eta| < 1.1$) and hadron calorimeter ($|\eta| < 0.9$).
- Endwall hadron calorimeter ($0.7 < |\eta| < 1.3$).
- Endplug electromagnetic calorimeter ($1.1 < |\eta| < 2.4$) and hadron calorimeter ($1.3 < |\eta| < 2.4$).

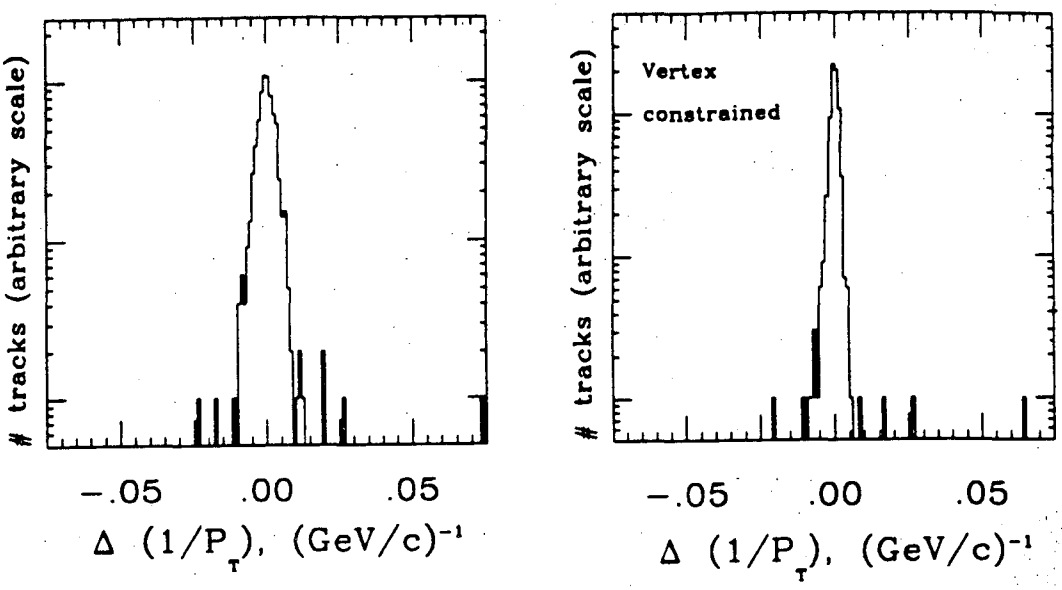

Figure 2.10: Distribution of $\Delta 1/P_T$ between measured and generated tracks for tracks between 10 and 25 GeV/c merged into jet events. a) Unconstrained to the event vertex. b) Vertex constraint imposed.

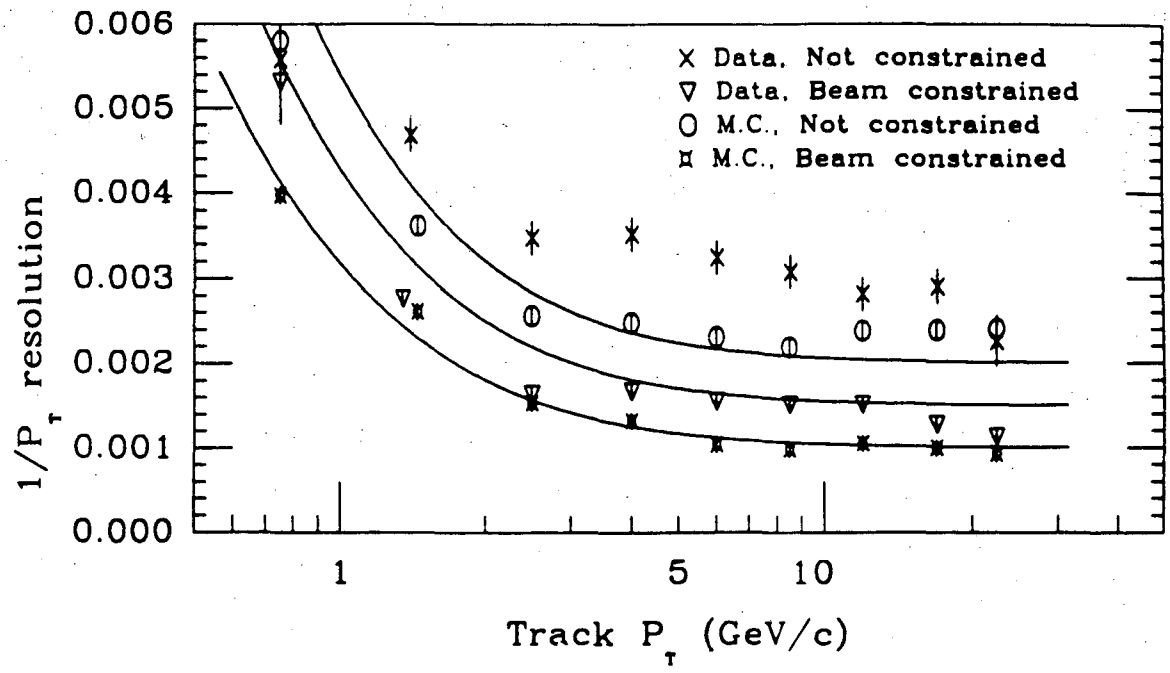

Figure 2.11: CTC $1/P_T$ resolution estimated from track merging, as a function of P_T. The three curves shown are the parametrized resolution and the estimated upper and lower uncertainties to the resolution.

- Forward electromagnetic calorimeter ($2.2 < |\eta| < 4.2$) and hadron calorimeter ($2.3 < |\eta| < 4.2$).

The calorimetry in CDF is segmented into a grid of towers in η and ϕ which project toward the nominal interaction point at $x = y = z = 0.0$. The tower segmentation, shown in Figure 2.12, was chosen such that typical high P_T jets deposit their energy over several towers.

Figure 2.13 is a calorimeter display of the same dijet event shown in Figure 2.7. In this calorimeter "Lego" plot the energy depositions of the two jets are clearly visible as energy clusters in the $\eta - \phi$ tower grid. Energy deposited in the electromagnetic and hadron calorimetry are shown in lighter and darker shades.

Sampling calorimeters such as those in CDF are composed of two media: a passive, dense medium causes a particle to interact and generate a shower of secondary particles, the number of which are nearly proportional to the incident particle energy; and an active, lower density medium which collects signals nearly proportional to the number of secondary particles. Electrons and photons interact with the absorber via bremsstrahlung and pair production in a characteristic distance called the radiation length X_0. For dense media the radiation length (expressed in grams/cm^2) is approximately $X_0 \simeq 180A/Z^2$[34], where A and Z are the atomic number and mass, respectively. Hadrons interact with nuclei in a typical length λ, the absorption length, which is approximately $35A^{1/3}$[34].

The CDF calorimetry uses lead as the absorber for the electromagnetic compartments and iron for the hadron compartments. The iron serves as a return yoke for the magnetic field. In the central and endwall calorimeters, the active medium is scintillator, whereas in the endplug and forward calorimeters gas proportional chambers are used to detect the shower. The scintillator and gas calorimetry will be discussed separately in the next sections.

2.4.1 Central and Endwall Calorimeters

The central and endwall calorimeters cover the angular region $30 < \theta < 150°$ shared by full CTC coverage. Important characteristics of these calorimeters are summarized in Table

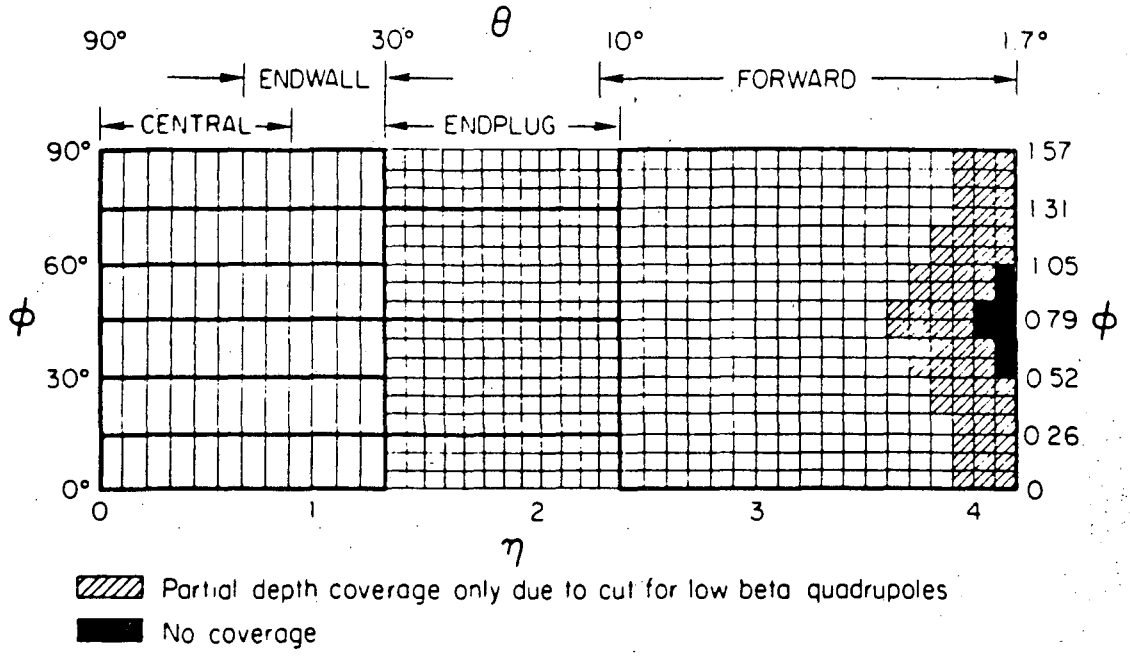

Figure 2.12: CDF calorimetry tower segmentation

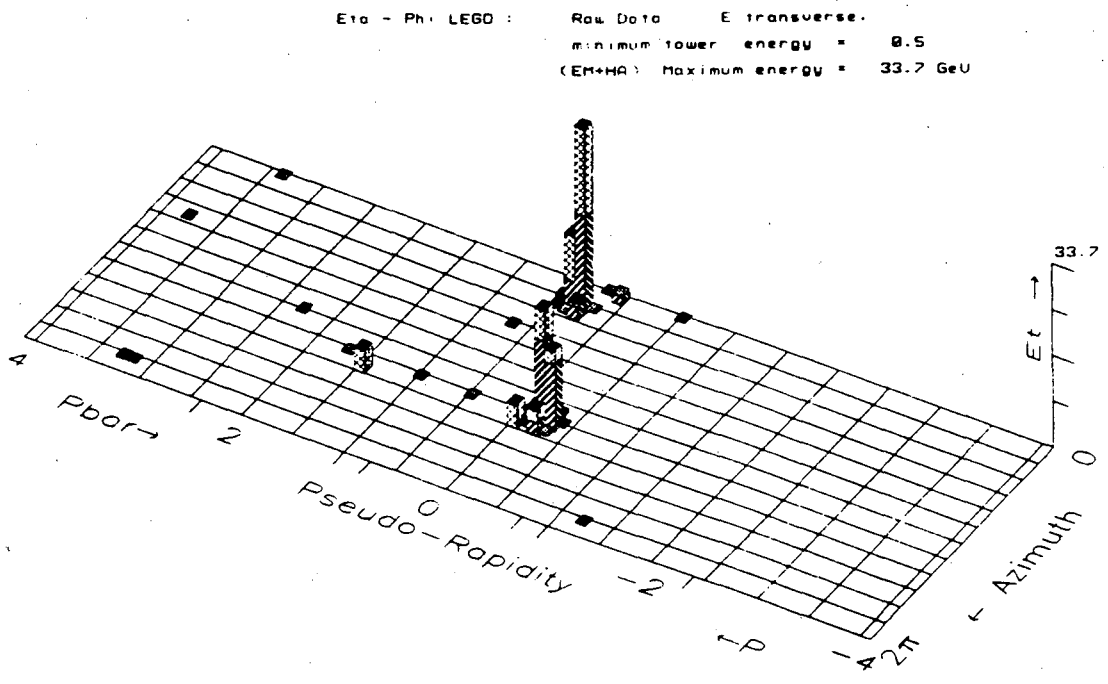

Figure 2.13: Jet event in calorimetry Lego plot

2.3. The central electromagnetic and hadron calorimeter are contained in two arches of 24 wedge shaped modules, each covering 15° in ϕ. The wedge modules also include a strip chamber embedded in the electromagnetic section for position measurement of electrons and photons to ± 2 millimeters precision, and a muon chamber located outside the hadron compartment. The endwall calorimeter is also divided into two groups of 24 modules which fit into the magnet yoke. The tower geometry is shown in Figure 2.14. Each tower covers 15° in ϕ and 0.11 units of η. Five tower channels in θ are covered partially by both central and endwall modules.

In each tower the scintillation light is transferred by wavelength shifters and light guides to a pair of photomultiplier tubes located on each side of the module. For isolated particles, the two photomultiplier signals are compared to improve the ϕ angular resolution and also reject anomalous depositions in a single tube.

The photomultiplier signals go to amplifier cards in crates mounted on the outside of the detector. Amplified signals above an analog threshold are digitized by ADC's. Signals from the hadron compartment also have their times recorded by TDC's. The hadron TDC information is used to reject out-of-time energy depositions.

Calibration and Monitoring

All of the central calorimeter modules were calibrated in a test beam. Electrons of 50 GeV were used to determine the absolute calibration constants for the electromagnetic compartment in picocoulombs/GeV, ignoring energy which leaked into the hadron compartment (typically one percent). The hadron compartment calibration was set using 50 GeV pions which were required to leave only minimum ionizing signals in the electromagnetic compartment. For each tower, the energy is defined as the unweighted sum of electromagnetic and hadronic tower energies. The relative calibration of all central modules was also checked using radioactive sources and cosmic ray muons.

The response of a scintillator calorimeter can change due to the effects of radiation damage and scintillator aging. In addition, a magnetic field raises the scintillator light

Table 2.3: Properties of the central and endwall calorimetry.

	Central electromagnetic	Central Hadron	Endwall Hadron
Number of modules	48	44	48
Number of layers	20-30	32	15
Absorber thickness	0.32 cm	2.5 cm	5.0 cm
Absorber material	Pb	Fe	Fe
Scintillator thickness	0.5 cm	1.0 cm	1.0 cm
Scintillator material	SCSN-38 polystyrene	PMMA acrylic	PMMA acrylic
Energy resolution	$13.5\%/\sqrt{E}$	11% (50 GeV π)	14% (50 GeV π)

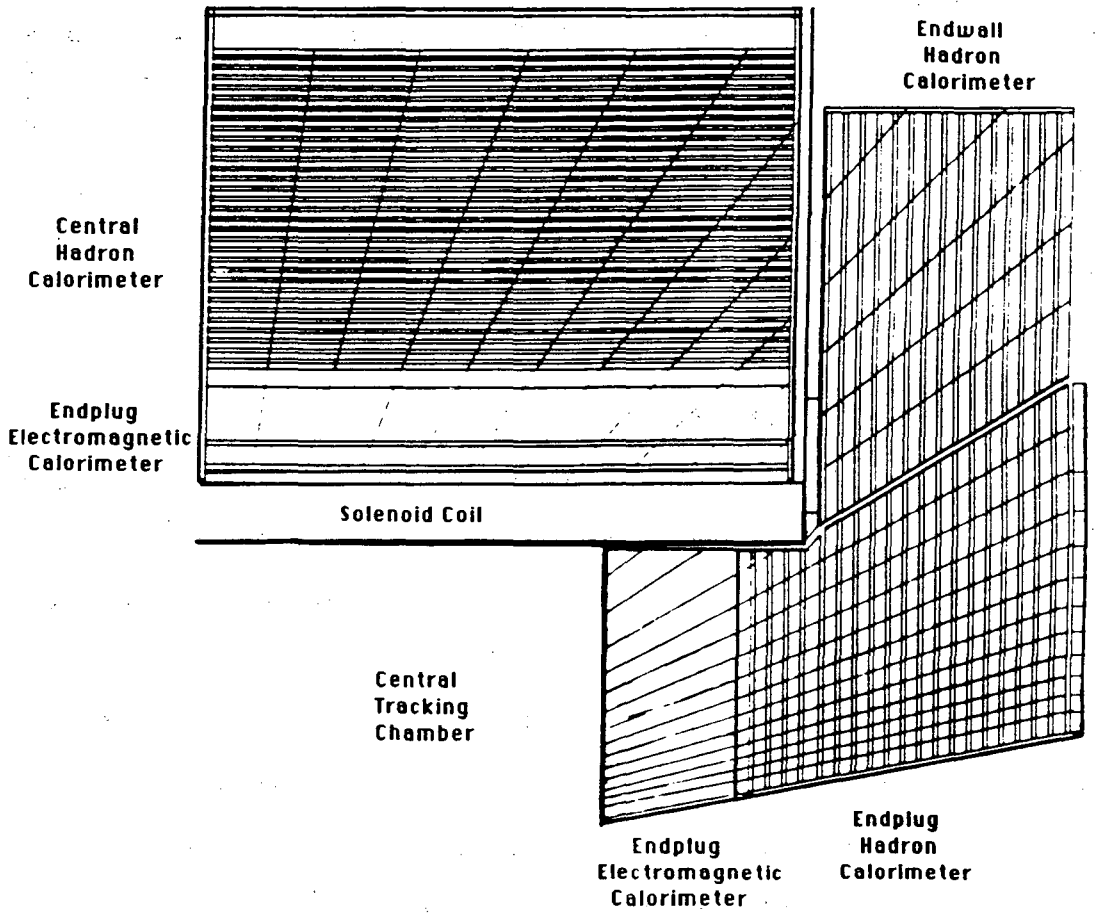

Figure 2.14: Tower geometry in the central, endwall and endplug calorimetry.

output, which in the case of CDF amounted to a five percent gain increase. Thus, it was important to monitor the stability of the calibration with time. Several systems were used for this purpose:

- A system of movable Cs^{137} radioactive sources was used to directly irradiate the scintillator plates.
- Xenon flash bulbs were used to illuminate the waveshifters in the electromagnetic compartment.
- A laser was used in the hadron calorimeters to inject light directly into the photomultiplier tubes.
- Light emitting diodes (LED's) were used in the electromagnetic calorimeter to monitor the gain of the photomultiplier tubes. In the hadron calorimeter, LED's were used to stabilize the gain of the photomultipliers to $\pm 2\%$ by pulsing between beam crossings.

With these systems, the absolute calibration of the electromagnetic and hadron compartments were maintained to approximately 0.2% and 2%, respectively, throughout the run.

Response Linearity and Uniformity

The response of the calorimeter to particles with momenta between 0.5 GeV and 10 GeV was determined in situ in two separate studies using isolated tracks in the CTC. At energies below 10 GeV, the lowest available test beam energy, the response of the calorimeter to hadrons deviates significantly from linearity. Most particles measured by the experiment, in jets or otherwise, are at these low energies.

The first study[35] used data from minimum-bias data collected in 1987. Particles (assumed to be pions) were required to be isolated in a five by five rectangle of towers in the range $|\eta| < 0.6$. Substantial systematic uncertainty to the results was caused by the procedure for subtracting neutral background energy. An improved study was performed with data from 1989 using a special trigger for high P_T particles as well as minimum bias data. In the recent study the systematic uncertainties were diminished to approximately

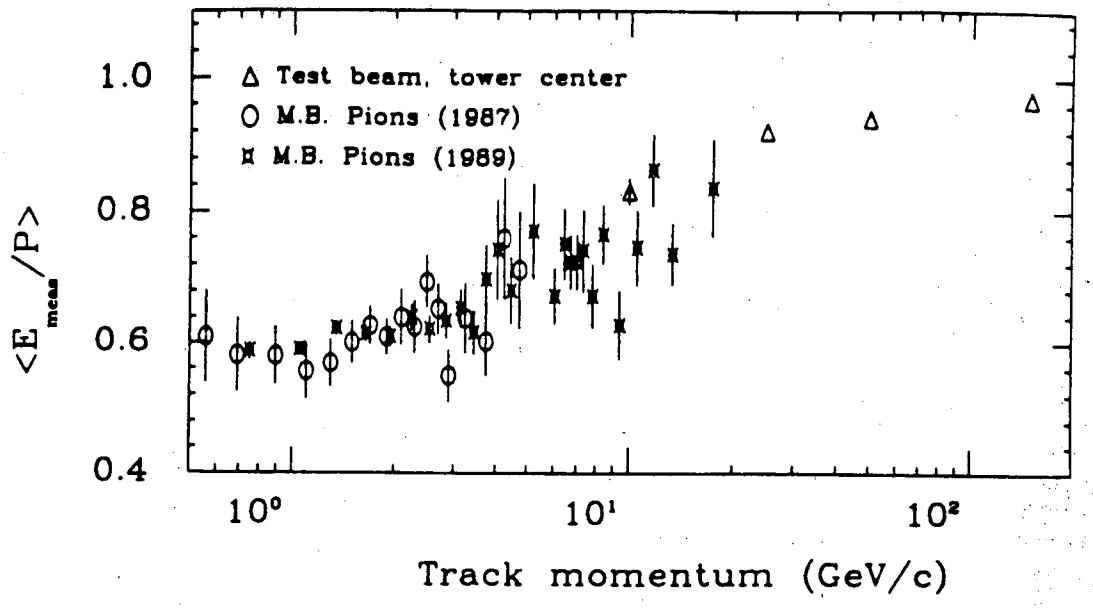

Figure 2.15: Central calorimeter response to charged pions.

5 percent and the momentum range was extended considerably. The results of both studies are illustrated in Figure 2.15. The plot shows that the calorimeter average response $< E_{measured}/P_{incident} >$ deviates from unity by up to 40 percent for low momentum particles.

The central calorimeter responds nonuniformly to electrons and pions incident on three regions:

- The crack where the two arches join at $\theta = 90°$.
- The θ cracks between towers. A ten percent response loss for pions was observed at the θ cracks in the test beam, but this effect is only noticeable for events very close to the nominal interaction point.
- The ϕ cracks, within one degree of the boundaries between the 15 degree wedge modules. For jet measurements, the ϕ cracks are the most serious nonuniformity in the central calorimeter, as they always project toward the collision vertex and the response in them is low by up to 40 percent.

Table 2.4: Characteristics of the endplug and forward calorimeters.

	Endplug electromagnetic	Endplug hadron	Forward electromagnetic	Forward hadron
Number of modules	8	24	8	8
Longitudinal sections	3	1	2	1
Anode layers	34	20	30	27
Absorber thickness	0.27 cm	5.1 cm	0.48 cm	5.1 cm
Absorber material	Pb	Fe	94%Pb/6%Sb	Fe
Energy resolution	4% (50 GeV)	20% (50 GeV)	4% (50 GeV)	20% (50 GeV)

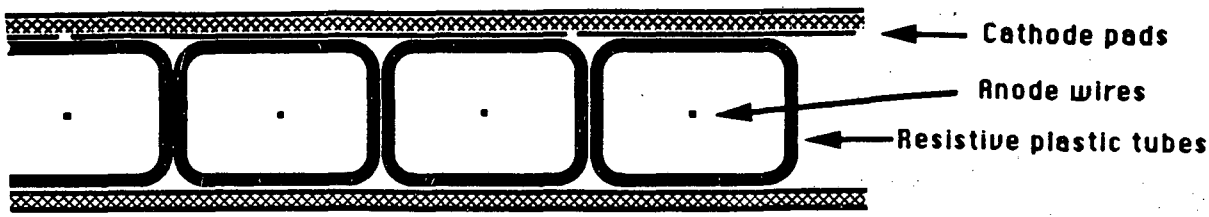

Figure 2.16: Cross section view of an endplug hadron calorimeter chamber.

2.4.2 Endplug and Forward Calorimeters

The gas calorimeters in the endplug and forward regions were commissioned during the 1987 running period. Some important characteristics of these detectors are listed in Table 2.4. The endplug and forward calorimeters are similar in design and operation. As an example, the endplug hadron calorimeter uses modular proportional chambers covering a 30 degree ϕ slice. A cross sectional view of an endplug hadron calorimeter chamber is shown in Figure 2.16. Inside the chamber an anode wire plane at high voltage is surrounded by extruded resistive plastic tubes. Charge deposited in the Argon-Ethane gas mixture is amplified at the anode wire, and this avalanche process induces a signal on a grid of cathode pads at

the edge of the chamber. The cathode pads from a stack of such chambers are joined into projective tower channels. Also, the anode wires in a chamber are read out as a single channel, providing information on the longitudinal shower development.

The θ range of these calorimeters is not covered by the CTC, with the exception of the outer edge of the endplug. For this reason they are not used directly for the analysis in this thesis, except for determining event topology used in event selection.

Calibration and Monitoring

The endplug and forward calorimeters were calibrated with test beams and using radioactive sources. One undesirable feature of the gas calorimetry is that the calorimeter response is a strong function of the gas density and mixture, which vary with atmospheric pressure and time. A system of proportional tubes was used to track the response with time using Fe^{55} radioactive sources. The position of the Fe^{55} source peaks with time was checked every few hours. When the calorimeter response changed by five percent or more, new calibration constants were downloaded to the data acquisition and trigger electronics.

2.5 Data Acquisition and Trigger

The CDF data acquisition system consists of an extensive FASTBUS[36] network containing the trigger system electronics, the SSP and MX/MEP scanners and a variety of other devices such as Segment Interconnects, TDC, and Flash ADC modules. Data collection is coordinated in the network by a VAX host computer which configures the network, downloads instructions and data to the scanners at the beginning of a run, and reads data from the network. The data are then stored on magnetic tapes for off-line analysis.

2.5.1 Trigger System

The trigger system is responsible for selecting events to be recorded and reducing the event rate to a manageable level of approximately one event per second. The full CDF trigger system works in three levels, each level applying more sophisticated criteria than the previous.

In 1987, however, only the first level trigger had been implemented. Events were required to satisfy one or more of several trigger criteria to be recorded. The triggers relevant to this work are the following:

- The minimum-bias trigger required a coincidence of scintillator hodoscopes on the east and west end of the detector, referred to as the 'beam-beam counters'. Timing information from the beam-beam counters is used to reject beam-gas events and measure the collision time, which is important for the tracking system. The minimum-bias trigger accepts a large fraction of the inelastic $\overline{p}p$ cross section[37], and the rate of such triggers was used to determine the instantaneous luminosity to an accuracy of approximately 15 percent.

- The calorimeter sum transverse energy (ΣE_T) triggers required a beam-beam counter coincidence along with transverse energy in the calorimetry above an adjustable threshold. The trigger hardware formed analog sums of energy in 'trigger towers' of segmentation $\delta\eta = 0.2$ by $\delta\phi = 15°$, requiring each tower included in the sum to be above a chosen single tower threshold. Two such triggers were used: one which summed transverse energy in the electromagnetic calorimeters only for triggering on electrons and photons; and one which triggered on both hadron and electromagnetic calorimeters, with the exception of the endplug and forward hadron calorimeters which were not included because of noise problems. The latter was suitable for central jet analysis and was used for the data presented in this thesis. The transverse energy thresholds were set to one of four values ranging from 20 to 45 GeV, depending on the beam luminosity during the run.

Chapter 3

Jets in CDF

Hadronic jets are the most notable feature in high P_T hadron collisions, as the cross section for their production is much higher at a given P_T than for any other standard model processes. At the Tevatron energy, dijet events such as the one displayed in Figures 2.7 and 2.13 are typical of events with substantial transverse energy. The interpretation of the event as hard scatter of quarks or gluons into two jets is clear. This is because the momentum of the interacting partons is much larger than the hadron mass scale ($\sim$1 GeV), so the longitudinal momenta of particles along the jet axis is large compared with the transverse components introduced in the fragmentation process.

3.1 Jet Definition

3.1.1 CDF Jet Clustering Algorithm

Jets are defined in CDF using only calorimetry data, with a clustering algorithm[38] which uses a fixed cone in $\eta - \phi$ to define a jet. There are several parameters which may be varied to change the jet definition, most important of which is the cone radius $R_{cluster}$. The algorithm proceeds as follows:

1) Preclusters are formed as seeds for jet clusters. At this stage a uniform tower segmentation of $\Delta\eta = 0.1$ by $\Delta\phi = 15°$ is used throughout the calorimetry. Adjacent towers, each with E_T greater than $E_{T,seed} = 1.0$ GeV per compartment, form a precluster if their combined E_T is greater than $E_{T,precluster} = 2.0$ GeV. Preclusters are kept small by requiring continuously decreasing tower E_T along a chain.

2) The preclusters, ordered in decreasing E_T, are made into clusters. Using the actual calorimeter segmentation, towers with E_T greater than $E_{T,min} = 0.1$ GeV per compartment are combined with a precluster if the tower center distance to the precluster E_T centroid $\Delta R \equiv \sqrt{\Delta\eta^2 + \Delta\phi^2}$ is less than $R_{cluster} = 1.0$. Towers may be shared between clusters at this stage.

3) For each cluster, the E_T centroid position is recalculated using the associated list of towers. The tower list is adjusted, where towers can be added or dropped based on their distance to the new centroid. This step is iterated until the tower list is constant.

4) In cases where two clusters overlap, the two are combined if the overlap E_T fraction is greater than half of the smaller cluster. Otherwise each overlap tower is given to the cluster with the closest centroid, and no towers are shared between clusters.

Several kinematic variables are used to describe the jet clusters. They are:

- The cluster energy E. This is taken as the unweighted sum of tower energies which make up the cluster.
- The cluster momentum $\vec{P}$. A momentum is defined for each tower from its energy and direction, assuming no internal mass for the energy deposited within a tower ($|P| = E$). The tower momenta are added as vectors obtaining a cluster P_x, P_y and P_z.
- The cluster transverse momentum $P_T = \sqrt{P_x^2 + P_y^2}$.
- The cluster polar angle $\theta = \tan^{-1}(P_T/P_z)$ and pseudo-rapidity $\eta = -\ln\tan(\theta/2)$.
- The cluster azimuth $\phi = \tan^{-1}(P_y/P_x)$.
- The cluster transverse energy $E_T = E\sin\theta$.
- The cluster detector pseudo-rapidity η_d is the position of the cluster in the calorimetry assuming the event vertex was at $z = 0.0$. η_d is used to make detector fiducial cuts, since boundaries between detector components are at fixed η_d but vary in η.

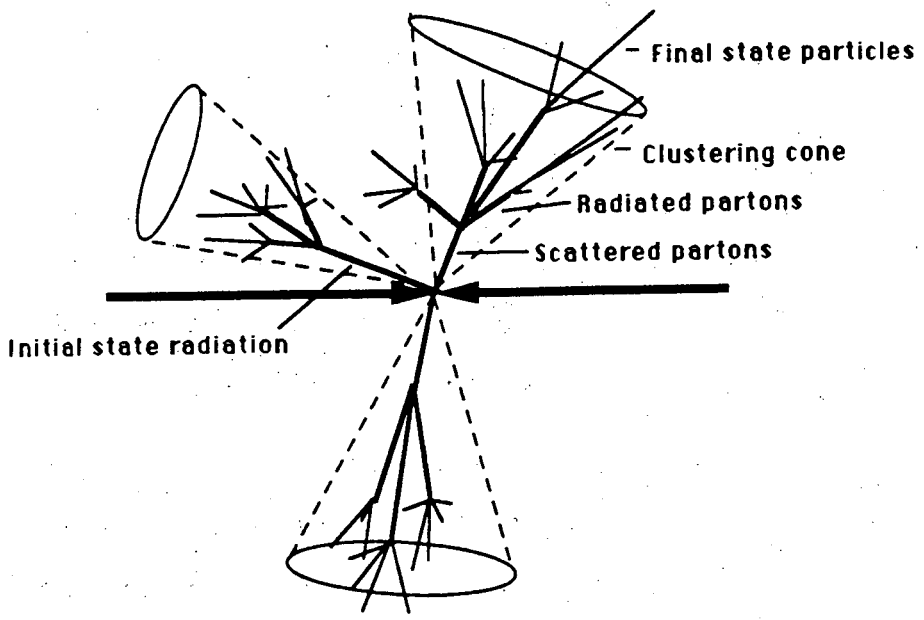

Figure 3.1: A sample jet event from a Monte-Carlo event generator.

3.1.2 Monte-Carlo Jet Definition

Four Monte-Carlo event generators have been used extensively in the CDF experiment: ISAJET[39], HERWIG[40], PYTHIA[41] and PAPAGENO[7]. PAPAGENO is a parton level generator which produces quarks and gluons rather than final state particles, and is therefore not included in this discussion. The other three combine parton level generators for $2 \rightarrow 2$ scattering processes with parton evolution and hadronization according to specific models. The output of the Monte-Carlo generators consists of the momenta of the partons which scattered or which were radiated from the initial or final state, the hadrons which those partons produce, and the decay products of those hadrons which are too short lived to observe in the laboratory.

Jets were defined in the Monte-Carlo case using the same $\eta - \phi$ cone as is used for the data, for consistency in comparing M.C. produced jets with detected jets. An example of an Isajet event is shown in Figure 3.1. For the ISAJET generated data, the algorithm defining jets was as follows:

1) The momenta of partons (quarks or gluons) which hadronize are put in a list ordered in decreasing P_T.

2) Each parton is compared with partons of higher P_T, and if two are closer than $R_{cluster} = 1.0$ they are combined into one. This step is repeated to make a smaller list of partonic jets.

3) The jet kinematic variables are calculated from the final state particles generated from the hadronization of the partons. This is because the hadronization model does not conserve energy. The final particles are not required to be within the cluster cone.

The unique correspondence between parton and hadrons in ISAJET is possible because of the independent fragmentation scheme, which also explains why some kinematic variables are not conserved in the process. For the other fragmentation models the primary hadrons, rather than the partons, are clustered. The distinction is important, since the partons are not observable; fortunately, at high jet E_T the ambiguity introduced by the different definitions is small.

3.2 Jet Energy/Momentum Corrections

The measured cluster 4-momenta need to be corrected for several effects, both instrumental and physical. The instrumental effects include:

- Nonlinearity of the calorimeter response to charged particles.
- Jet spreading due to the magnetic field.
- Calorimeter response nonuniformity from cracks and other variation in η and ϕ.
- Energy that escapes out the back of the calorimeter.
- Single tower thresholds.

The physical effects include:

- Energy entering clusters from the underlying event.
- Energy from jets not within the cluster cone.

- Unseen particles (neutrinos, muons) in jets.

There are inherent uncertainties involved with the physical effects; However, the physical effects are small in comparison to the instrumental effects and therefore the uncertainties have little impact on the overall corrections. This is especially true as the jet P_T increases. Some of the instrumental effects can be reliably estimated directly from the data whereas other effects require the Monte-Carlo and detector simulation.

For this work the jet corrections were applied in two stages. In the first stage, correction was applied to individual jets for calorimeter nonlinearity and the magnetic field utilizing tracking information[42]. The purpose of the tracking correction was to reduce jet response bias from fragmentation fluctuations. In the second stage, an average correction was applied for the other effects, based upon the measured cluster momenta. These are discussed in the next two sections.

3.2.1 Tracking Correction to Jet Energy and Momentum

Jet 4-vectors were corrected by associating charged tracks to jets, and correcting the jet momentum and energy for the expected losses from calorimeter nonlinearity and magnetic field effects for that set of tracks. Only jets within the pseudo-rapidity range $|\eta_d| < 2.0$ are corrected by this procedure. A track was associated with a jet if :

- the track passed the selection criteria (Section 2.3.7) and had enough P_T to reach the central calorimeter radius.

- the track total momentum was less than 100 GeV/c.

- the track did not penetrate the endplug electromagnetic calorimeter face, both for acceptance reasons and because the low energy pion response had not been investigated there.

- the track was inside the $\eta - \phi$ clustering cone using the track parameters at the event vertex or propagated to the calorimeter:

$$\Delta R = \sqrt{(\eta_{track} - \eta_{jet})^2 + (\phi_{track} - \phi_{jet})^2} < R_{cluster}$$

Tracks could be associated to jets at the event vertex, the calorimeter or both. Those associated to a jet at the vertex were assumed to be physically part of the jet, whereas those produced at large angles that entered the jet cluster because of the magnetic field were assumed not to be part of the jet. For each track of momentum P, the expected calorimeter response $< E_{meas} >$ was evaluated from the results of the 1989 nonlinearity study (Section 2.4.1).

The correction to jet energy was divided into two parts. The nonlinearity correction compensated for undermeasured energy for tracks associated both at the vertex and the calorimeter, and is expressed:

$$E_{nonlin} = \sum_{i=1}^{n_{both}} (|P_i| - < E_{meas} >_i)$$

The B-field correction, for tracks which entered or exited the jet due to the magnetic field, is:

$$E_{Bfield} = E_{out} - E_{in} = \sum_{i=1}^{n_{vertex}} |P_i| - \sum_{j=1}^{n_{cal}} < E_{meas} >_j$$

The jet cluster energy was then corrected for the two effects using the above equations:

$$E_{trkcor} = E_{cluster} + E_{nonlin} + E_{Bfield}$$

Jet momenta were corrected by scaling up the individual momentum components to preserve the jet direction measurement obtained from calorimetry. The nonlinearity and magnetic field terms are expressed as follows:

$$|P_{nonlin}| = \sum_{i=1}^{n_{both}} (|P_i| \cos\zeta_v - < E_{meas} >_i \cos\zeta_c)$$

$$|P_{Bfield}| = \sum_{j=1}^{n_{vertex}} |P_j| \cos\zeta_v - \sum_{k=1}^{n_{cal}} < E_{meas} >_k \cos\zeta_c$$

where ζ_v and ζ_c are the angles between the track and the jet at the vertex and calorimeter, respectively.

The distribution of the energy correction factors ($E_{trkcor}/E_{cluster}$) is shown in Figure 3.2a. The average correction for jets with $|\eta_d| < 0.8$ is approximately 20 percent and decreases slowly with increasing energy as shown in Figure 3.2b. The tracking correction varies slowly with pseudo-rapidity for $|\eta_d| < 0.6$, as illustrated in Figure 3.2c.

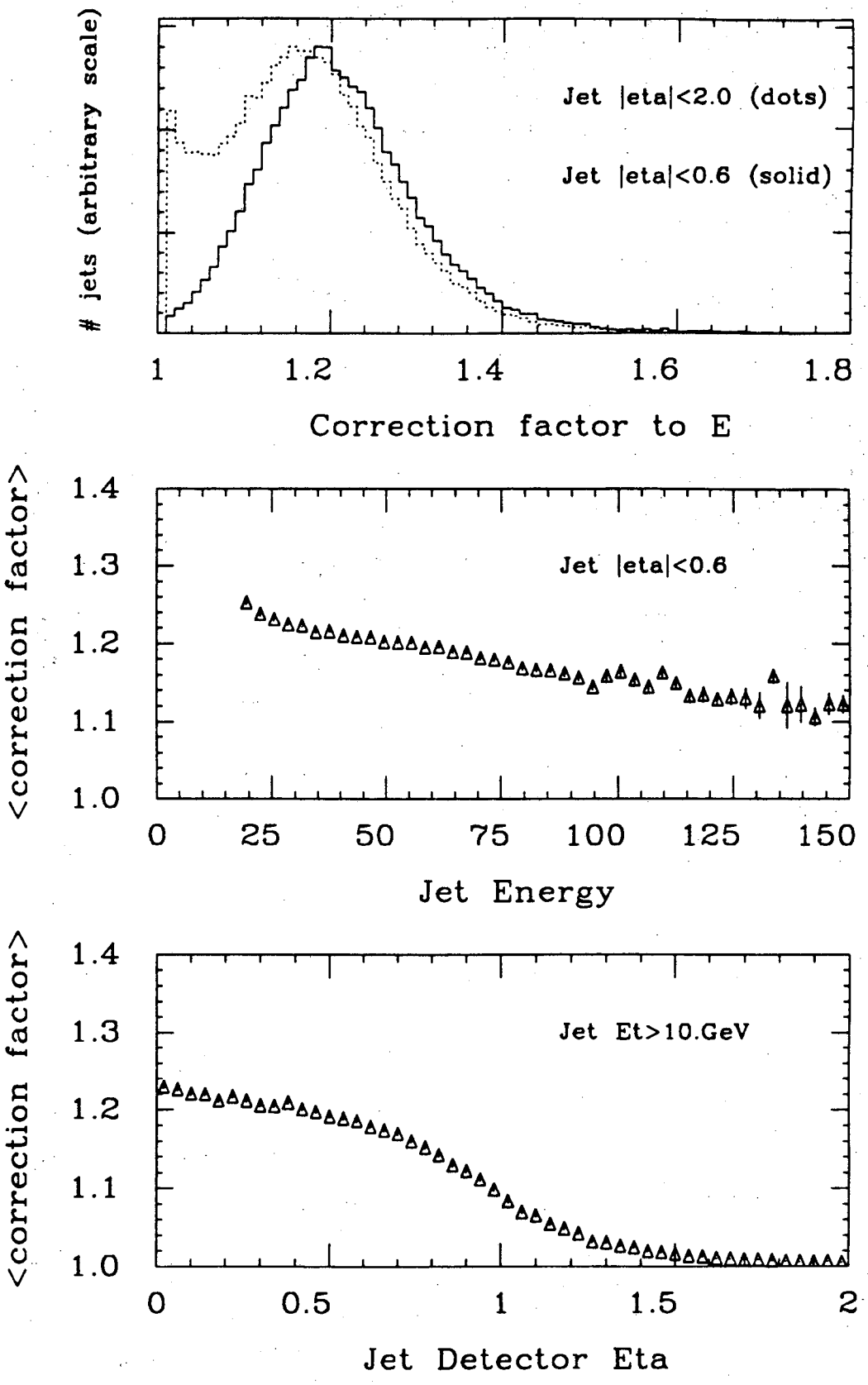

Figure 3.2: a) Tracking correction factor to jet energy. b) Average tracking correction factor as a function of jet energy. c) Average correction factor as a function of jet pseudo-rapidity.

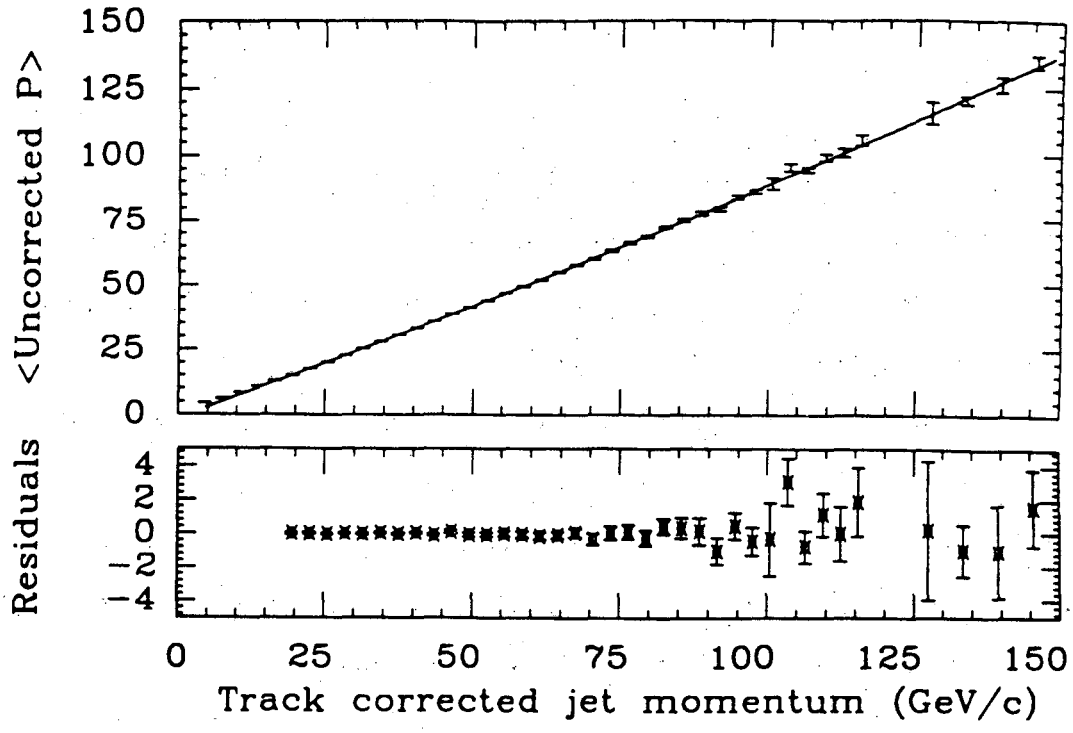

Figure 3.3: Evaluation of the average tracking correction.

3.2.2 Average Jet Energy/Momentum Correction

An average correction to jet momentum and energy was applied after the tracking correction to account for leakage, cracks, thresholds and other effects. The correction was adapted from the average central jet correction of Kuhlmann *et al*[43] which was used in the inclusive central jet analysis.

Since the average central jet correction includes a correction for nonlinearity and magnetic field effects that were already taken into account in the tracking correction, the average value of the tracking correction needed to be removed. For this purpose an inverse tracking correction was measured using the data. The average uncorrected momentum was determined for a given corrected cluster momentum, as is shown in Figure 3.3. A quadratic polynomial fit between 20 and 150 GeV/c was used to parametrize the correction:

$$|P_{invtrk}| = 0.00064|P_{trkcor}|^2 + 0.8327|P_{trkcor}| - 1.4$$

$$E_{invtrk} = 0.00123E^2_{trkcor} + 0.7123E_{trkcor} + 2.0$$

The fit residuals are small; however, beyond the range 20 to 150 GeV, the validity may be questionable.

In the central jet study, simulated Monte-Carlo data were used to determine the effects of calorimeter response, cracks, leakage and other losses. The ISAJET Monte-Carlo generator was used to generate jets at several discrete values of jet P_T, without any underlying event particles. Only events with two clustered parton jets (Section 3.1.2) were used. The ISAJET input fragmentation parameters were adjusted to match preliminary CDF jet fragmentation data for several distributions, and those parameters were varied to evaluate their effect on the jet corrections. The ISAJET events were passed through the CDFSIM simulation program[45]. For each jet, the energy in a hemisphere of the detector was summed as the calorimeter response to the jet, and the average corrections from measured to produced jet momentum and energy were determined.

The amount of energy from the underlying event inside the jet clusters was evaluated by measuring the energy density per unit $\eta - \phi$ area in the region at 90 degrees in ϕ from the jets in dijet events[44]. Events were selected from the data with only two jets very nearly back-to-back in azimuth. The energy density was measured to be 0.99±0.35 GeV per radian^2, and not observed to depend on the energy of the jets in the event. By varying the radius $R_{cluster}$ of the clustering cone, the amount of energy lost outside the large cone size of $R_{cluster} = 1.0$ was determined to be negligible in comparison with the underlying event energy entering the cone. Further, the average energy loss caused by imposing the single tower threshold $E_{T,min} = 0.2$ GeV was 0.4 GeV. The present work uses a lower single tower threshold of 0.1 GeV, so this loss should be less, but in any case the difference is very small.

The average central jet correction was applied as follows:

$$E_{avecor} = \begin{cases} -0.00174E^2_{invtrk} + 1.37E_{invtrk} - 2.36\text{GeV} & \text{if } E_{invtrk} < 70 \text{ GeV} \\ 1.115E_{invtrk} + 6.68\text{GeV} & \text{if } E_{invtrk} > 70 \text{ GeV} \end{cases}$$

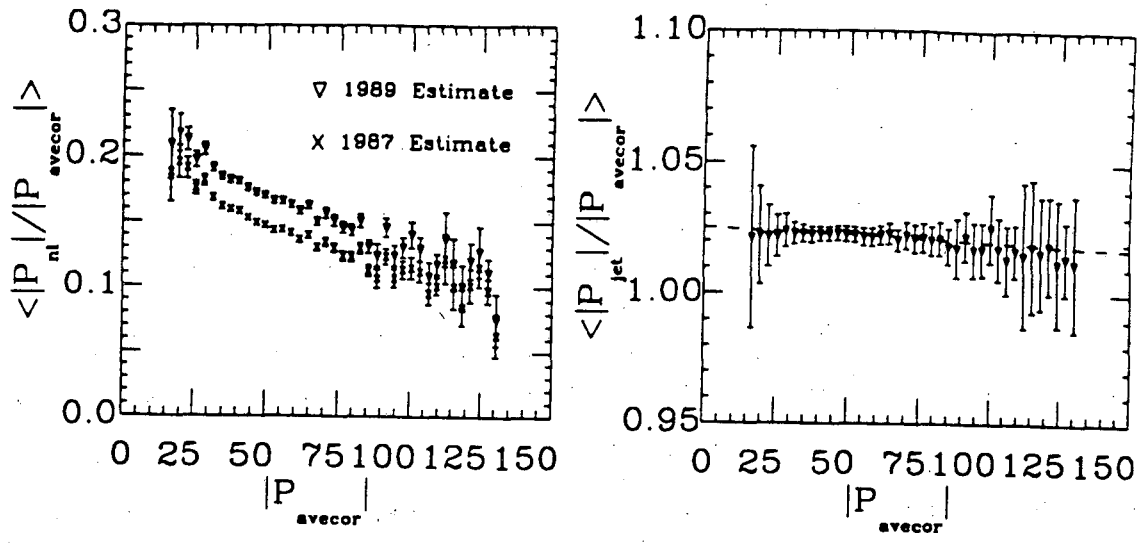

Figure 3.4: a) Jet momentum loss to calorimeter nonlinearity as a function of corrected jet momentum, using the 1987 and 1989 estimates of calorimeter response. b) Difference between the improved jet momentum correction and the previous average jet correction.

$$|P_{avecor}| = \begin{cases} -0.00146|P_{invtrk}|^2 + 1.31|P_{invtrk}| - 1.81\text{GeV}/c & \text{if } |P_{invtrk}| < 65 \text{ GeV}/c \\ 1.112|P_{invtrk}| + 4.83\text{GeV}/c & \text{if } |P_{invtrk}| > 65 \text{ GeV}/c \end{cases}$$

The average corrections were modified for this work to use the results of the 1989 nonlinearity study, in order to reduce the systematic uncertainty on the jet momentum scale. From the data, the fractional correction for nonlinearity for a given corrected jet momentum or energy was evaluated, using the two nonlinearity estimates from 1987 and 1989. For the two estimates, the average fraction of jet momentum lost due to nonlinearity is shown in Figure 3.4a as a function of $|P_{avecor}|$. The improved nonlinearity correction to jet momentum is obtained by substituting the 1989 average for the 1987 average:

$$|P_{jet}| = |P_{avecor}|(1+ < \frac{|P_{nl,89}|}{|P_{avecor}|} > - < \frac{|P_{nl,87}|}{|P_{avecor}|} >)$$

This is shown in Figure 3.4b and is parametrized as:

$$|P_{jet}| = 1.025|P_{avecor}| - 0.00005|P_{avecor}|^2$$

The modification amounts to approximately two percent change from the previously evaluated corrections.

3.2.3 Systematic Uncertainty on the Jet Corrections

The magnitude and estimated systematic uncertainty of the average jet energy and momentum corrections are shown in Figure 3.5. For the cone size of $R_{cluster}$ equal to 1.0, the momentum corrections range from 20 percent at low jet momentum to 13 percent for P_{jet} values greater than 200 GeV/c. The estimated uncertainty on the overall scale ranges from eight percent at P_{jet} = 30 GeV/c to below five percent at high momentum. The overall systematic error is a result of several effects of comparable magnitude, added in quadrature[43]. The largest contributors were: uncertainties in the calorimeter simulation, especially in the ϕ crack regions; the uncertainty of the true fragmentation function; and, at low momentum, effects of the underlying event and clustering algorithm[46]. The uncertainty due to uncertainty in the calorimeter response nonlinearity is relatively small. A two percent uncertainty, due to the fraction of charged vs. neutral momentum in the jet, was evaluated by varying the charged/total ratio within ISAJET. The size and uncertainty of the average jet energy correction are similar, but slightly larger, than the size and uncertainty of the momentum corrections.

3.3 Jet Angular and Momentum Resolution

The angular resolution with which jets are measured in the central calorimeter was investigated by comparing jet cluster ϕ and θ values with those obtained from the momentum sum of charged tracks in a cone about the jet axis. The difference $\Delta\phi$ and $\Delta\theta$ between the jet cluster axis and the track momentum sum is shown in Figure 3.6a for jets with total charged momentum above 20 GeV/c. The distribution RMS widths are both approximately three degrees, resulting from the combined resolution of the calorimeter axis and the track axis. The widths therefore overestimate the angular resolution of the calorimeter alone.

The jet momentum resolution in the central calorimeter was determined by the technique of dijet K_T balancing[42, 47, 48]. The K_T vector is defined as the net transverse

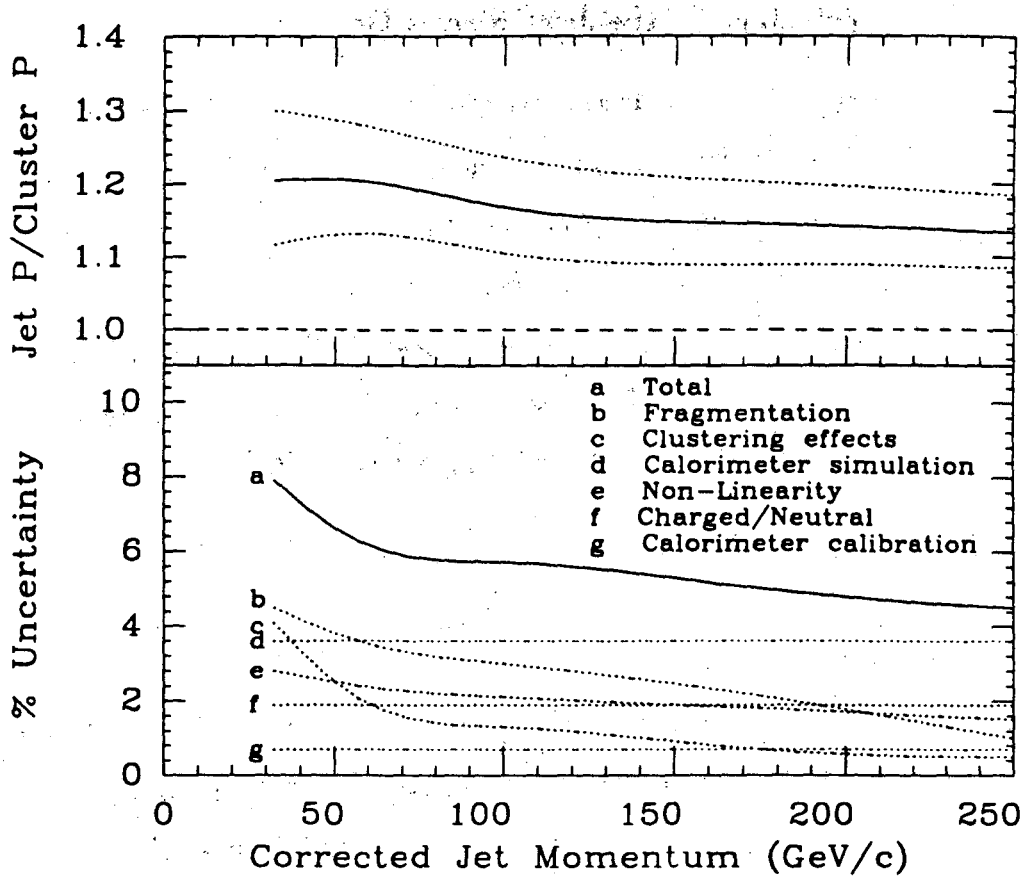

Figure 3.5: a) The average central jet momentum correction and uncertainty. b) Individual contributions to systematic uncertainty in jet momentum[43].

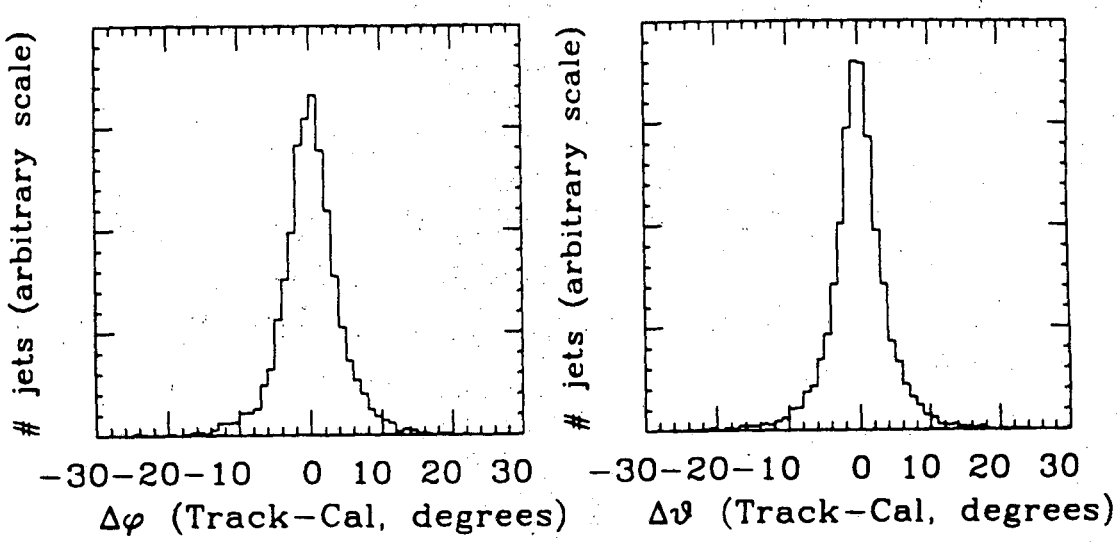

Figure 3.6: a) Difference between calorimeter and track jet axis ϕ. b) Difference between calorimeter and track jet axis θ.

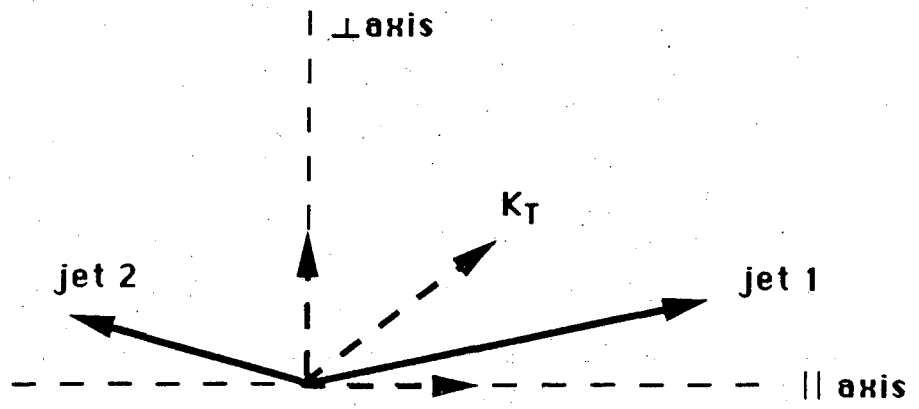

Figure 3.7: Transverse view of dijet event, illustrating K_T components.

momentum of the jets in the event:

$$\vec{K}_T = \sum_i^N \vec{P}_{T_i}$$

where $\vec{P}_{T_i}$ is the transverse momentum of the i-th jet. Conceptually, the most simple case is that of an event with only two jets, shown in Figure 3.7. The components of $\vec{K}_T$ are considered along two orthogonal axes ($\|, \perp$) parallel and perpendicular to the bisector of the two jets in the transverse plane, where the $\|$ axis is randomly directed toward either jet 1 or 2. The distribution of K_T projected onto these two axes is affected by contributions from jet momentum and angular resolution and also QCD radiative effects. The RMS widths of the K_T distribution for the two components is denoted here by $\sigma_{\|}$ and $\sigma_{\perp}$.

For dijet events, $K_{t,\|}$ is defined:

$$K_{t,\|} = \sum_{i=1}^{2} P_{T_i} \cos\phi_{\|_i} = \sum_{i=1}^{2} P_i \sin\theta_i \cos\phi_{\|_i}$$

where $\phi_{\|_i}$ is the angle between the P_T vector and the $\|$ axis. The contribution to the width $\sigma_{\|}$ from detector momentum resolution σ_P and angular resolutions σ_ϕ and σ_θ is:

$$\delta_{\|}^2 = \sum_{i=1}^{2} (\sigma_{P_i}^2 \sin^2\theta_i \cos^2\phi_{\|_i} + \sigma_{\theta_i}^2 P_i^2 \cos^2\theta_i \cos^2\phi_{\|_i} + \sigma_{\phi_i}^2 P_i^2 \sin^2\theta_i \sin^2\phi_{\|_i})$$

The contribution from angular resolution is small compared to that from momentum resolution because $\sin\phi_{\|} \ll 1$ and $\cos\theta \ll 1$ for central dijet events, and because the angular resolutions are less than 0.05 radians.

The width $\sigma_\perp$ is also produced by resolution and QCD radiative effects. The resolution contribution is written as:

$$\delta_\perp^2 = \sum_i (\sigma_{P_i}^2 \sin^2\theta_i \sin^2\phi_{||_i} + \sigma_{\theta_i}^2 P_i^2 \cos^2\theta_i \sin^2\phi_{||_i} + \sigma_{\phi_i}^2 P_i^2 \sin^2\theta_i \cos^2\phi_{||_i})$$

Only the ϕ resolution term is significant. The contribution from θ resolution can be neglected, and the P resolution term is also small if the jets are nearly back-to-back.

The radiative effects should add in quadrature with the measurement errors to produce the observed widths $\sigma_{||}$ and $\sigma_\perp$.

$$\sigma_{||}^2 = \delta_{||}^2 + (QCD)^2 \simeq 2\sigma_P^2 + (QCD)^2$$

$$\sigma_\perp^2 = \delta_\perp^2 + (QCD)^2 \simeq \sigma_\phi^2 P_{||}^2/2 + (QCD)^2$$

where $P_{||}$ is defined as $\sum P_i \sin^2\theta_i \cos^2\phi_{||_i} \simeq \sum P_i$ (typically within about five percent). In the above equations, the effects of QCD radiation recoiling against the dijet system were assumed to be the same in the $||$ and $\perp$ directions. The radiative term can then be removed from the width $\sigma_{||}$ by the following subtraction:

$$\sigma_{||}'^2 = \sigma_{||}^2 - (\sigma_\perp^2 - \sigma_\phi^2 P_{||}^2/2) \simeq 2\sigma_P$$

The quantities $\sigma_{||}'$ and $\sigma_{||}$ are shown in Figure 3.8a, for dijet events with no other jet with E_T above 5 GeV. Because of uncertainties in the procedure, the jet momentum resolution was estimated (for this work) to be the solid line between the 'subtracted' and 'not subtracted' points. The outer dashed lines show the upper and lower uncertainties which were used. These three estimates are given by the following parametrizations:

$$\sigma_P(P_{jet}) = \begin{cases} 1.085\sqrt{P_{jet}} - 2.25 & \text{Low estimate} \\ 1.105\sqrt{P_{jet}} - 1.475 & \text{Medium estimate} \\ 1.125\sqrt{P_{jet}} - 0.70 & \text{High estimate} \end{cases}$$

Figure 3.8b shows the effect of the tracking correction on the width $\sigma_{||}$, compared to the average central jet correction. The tracking correction is observed to improve the resolution by approximately 15 percent.

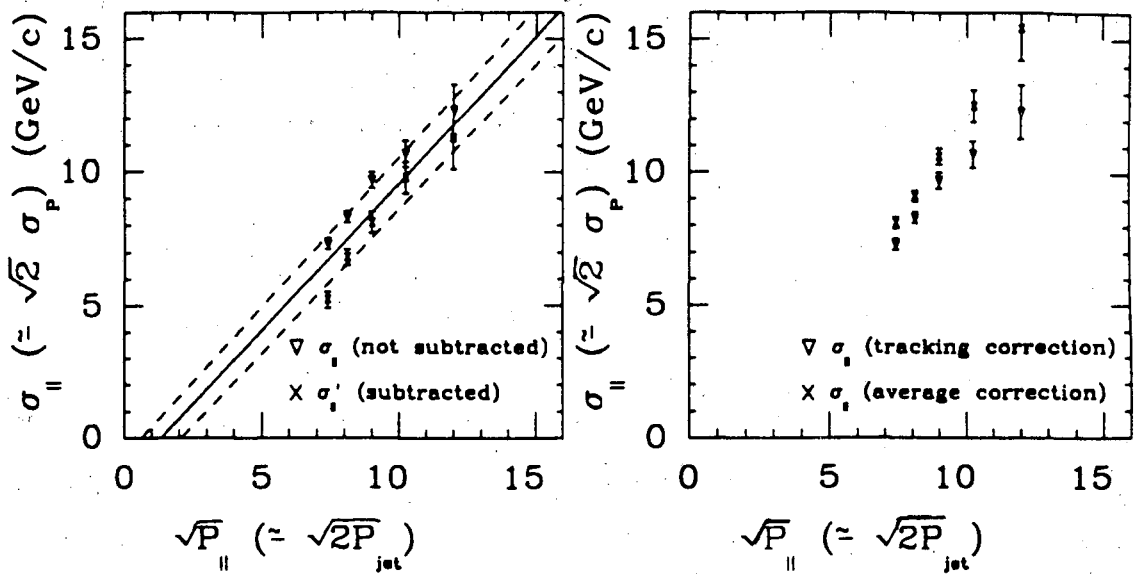

Figure 3.8: a) 'Unsubtracted' and 'subtracted' dijet $K_{t,\parallel}$ resolution vs $\sqrt{P_{\parallel}}$. b) Comparison of resolution with and without tracking correction.

3.4 Dijet Event Selection

Events and jets used for the jet fragmentation analysis were required to satisfy a set of criteria based on observed jet kinematics. The two goals in establishing these criteria was to obtain a sample of well-measured dijet events covering a large range of jet energy, and to avoid measurement biases caused by jet-by-jet fragmentation fluctuations. The data were obtained with the summed E_T calorimeter trigger (section 2.5.1). The analysis used only data from runs in which there were no known problems with data quality. The integrated luminosity contained in these runs was approximately 26 inverse nanobarns; the quantity collected with each of the four trigger thresholds is listed in Table 3.1.

In a preliminary pass, a subset of the nearly 135,000 events was selected for tracking data reconstruction[49]. At this stage, events were required to have at least two jets, and the sum of the highest two uncorrected cluster E_T's was required to be above thresholds chosen to remove trigger inefficiency bias. The thresholds, listed in Table 3.1, depended on the run trigger threshold, and whether both or only one of the two leading jets was within the central pseudo-rapidity range $|\eta_d| < 0.8$. Timing information from the central

hadron calorimeter was used to reject beam-gas events and other out-of-time backgrounds. Approximately 45,000 events were reconstructed.

Several additional selection criteria were imposed specifically for the jet fragmentation analysis:

- Only events with both jets with highest E_T in the range $|\eta_d| < 0.8$ were considered, amounting to a 54 percent reduction of the event sample.

- To remove residual trigger bias caused by the observed dependence of the raw cluster response on jet fragmentation fluctuations, higher thresholds were imposed on the sum of the highest two corrected jet E_T's. These thresholds are listed in Table 3.1 and shown with the corresponding jet pair E_T distributions in Figures 3.9a through 3.9d. The effect of the higher thresholds was to reduce the overall event sample by 57 percent.

Next, cuts were applied to select events with a two jet final state.

- The difference in azimuthal angle between the two highest E_T clusters is shown in Figure 3.10a. The shape of this distribution is due to the effects of angular resolution and initial and final state QCD radiation in the event, with a long tail resulting from additional jet activity. The two leading jets were required to be within 30 degrees of 'back-to-back' in ϕ. The cut retained 86 percent of the events.

- To ensure that the jets were isolated, no additional jets with E_T greater than the lesser of 20 GeV or 20 percent of the sum of the leading two jet E_T's were allowed. Figures 3.10b and 3.10c show the distributions in these quantities; approximately 72 percent of remaining events satisfied this cut.

Additional cuts were applied to ensure that the events and jets selected for analysis were well measured.

- To take advantage of the projective tower geometry of the calorimetry, the event vertex position was required to be within 50 centimeters of the nominal interaction point.

Table 3.1: Event selection cuts for the four hardware trigger samples. (1) Uncorrected jet pair E_T cut for central-central dijet events for reconstruction. (2) Uncorrected jet pair E_T cut for central-other dijet events for reconstruction. (3) Corrected jet pair E_T cut for central-central events used for fragmentation analysis.

Trigger	Hardware $\sum E_T$ Threshold	Luminosity nb^{-1}	Jet pair $E_T(1)$	Jet pair $E_T(2)$	Jet pair $E_T(3)$
LOW	20.	0.4	36.	40.	50.
MED	30.	13.2	48.	60.	70.
HIGH	40.	6.1	56.	60.	90.
BURN	45.	6.5	60.	60.	100.

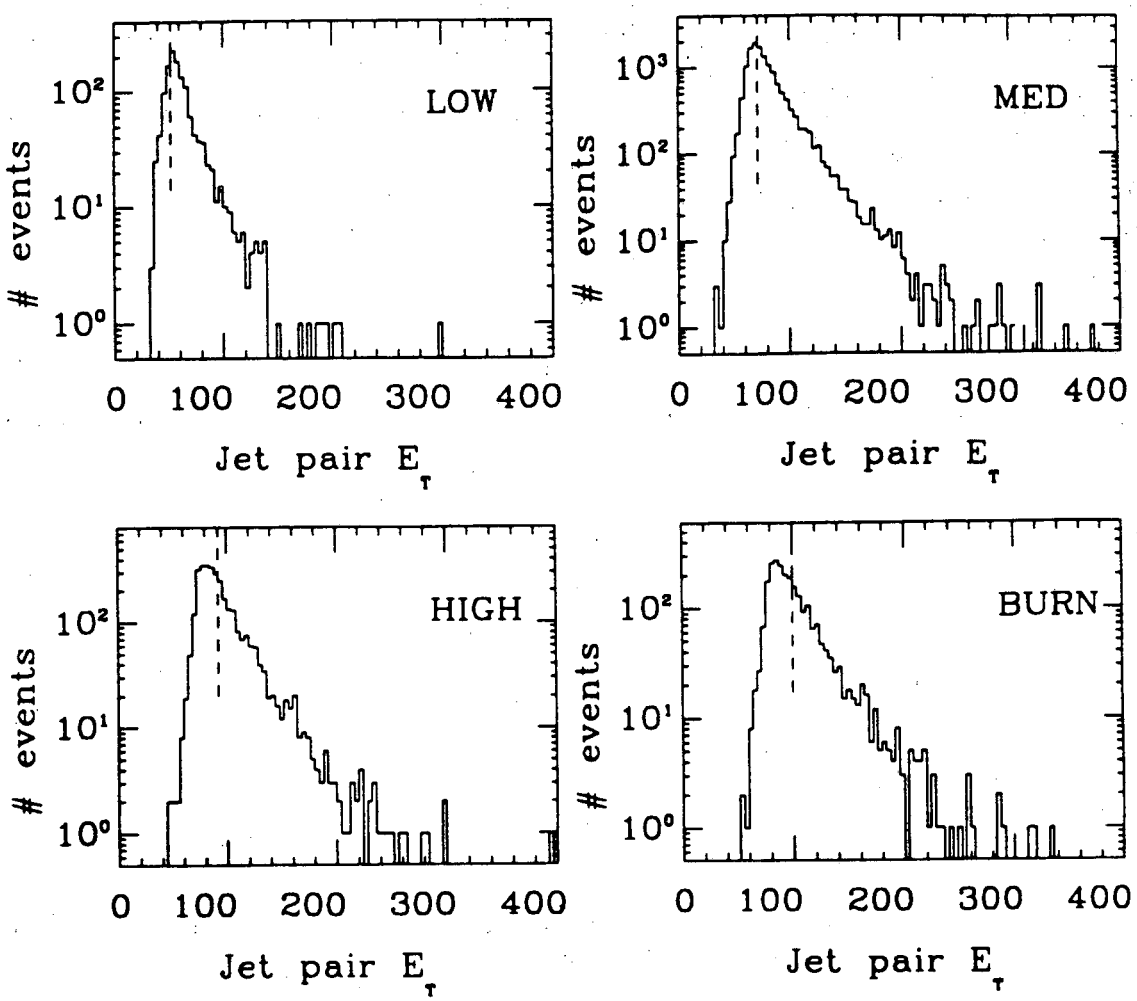

Figure 3.9: Jet pair E_T distributions for central-central jet events, for low, medium, high and burn trigger data.

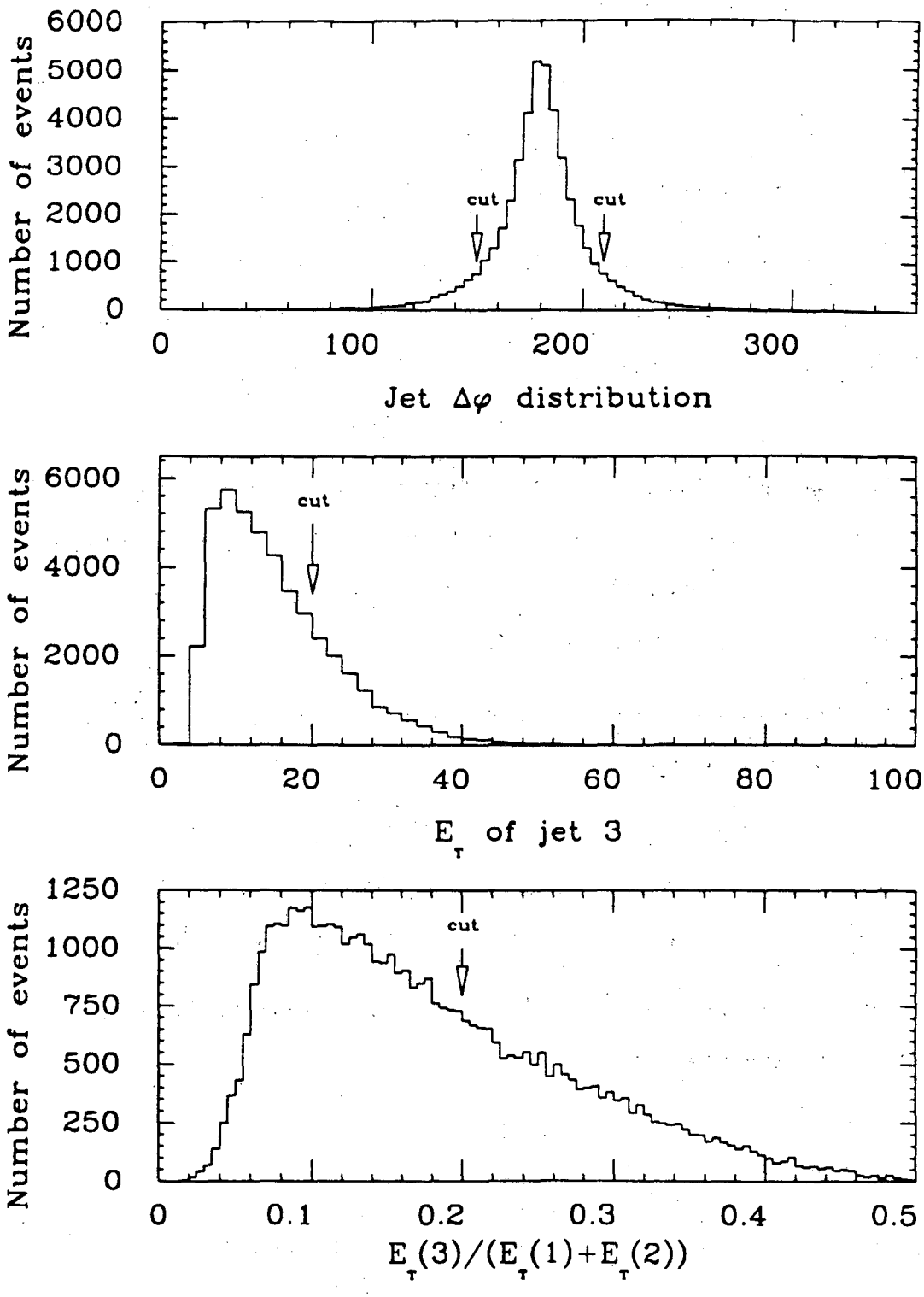

Figure 3.10: a) Delta phi between leading two jets. b) Third cluster E_T (GeV). c) Ratio of third cluster E_T to sum of leading two cluster E_T's.

The event vertex distribution is shown in Figure 3.11a. Approximately 15 percent of events were rejected by this cut.

- Fiducial cuts were also applied to the jets used for the analysis. Jet energy centroids were required to be within the detector pseudo-rapidity range $0.1 < |\eta_d| < 0.7$, where the calorimeter response is uniform and the CTC coverage is complete.

- For acceptance considerations, it was advantageous to limit the range of dijet boost rapidity of the events. The boost rapidity is defined as the average pseudo-rapidity of the leading two jets:

$$\eta_{BOOST} \equiv (\eta(1) + \eta(2))/2$$

The η_{BOOST} distribution is shown in Figure 3.11b for all events and the subset of central-central events. Boost effects were minimized by requiring η_{BOOST} to be less than 0.6, corresponding to a velocity of $0.54c$ for the dijet system along the beam axis. The fraction of remaining events which failed this cut was 9 percent.

- A cut on the dijet missing P_T significance was applied. The dijet missing P_T significance, defined here as

$$P_{T_{SIG}} \equiv \frac{K_{T,\parallel}}{\sqrt{E_T(1) + E_T(2)}},$$

and required to be less than 3.0. The distribution of this quantity is plotted in Figure 3.11c. Only two percent of the remaining events were discarded by this cut.

The final event sample satisfying the above criteria contained a total of 5541 events, with 8609 jets within the central fiducial volume.

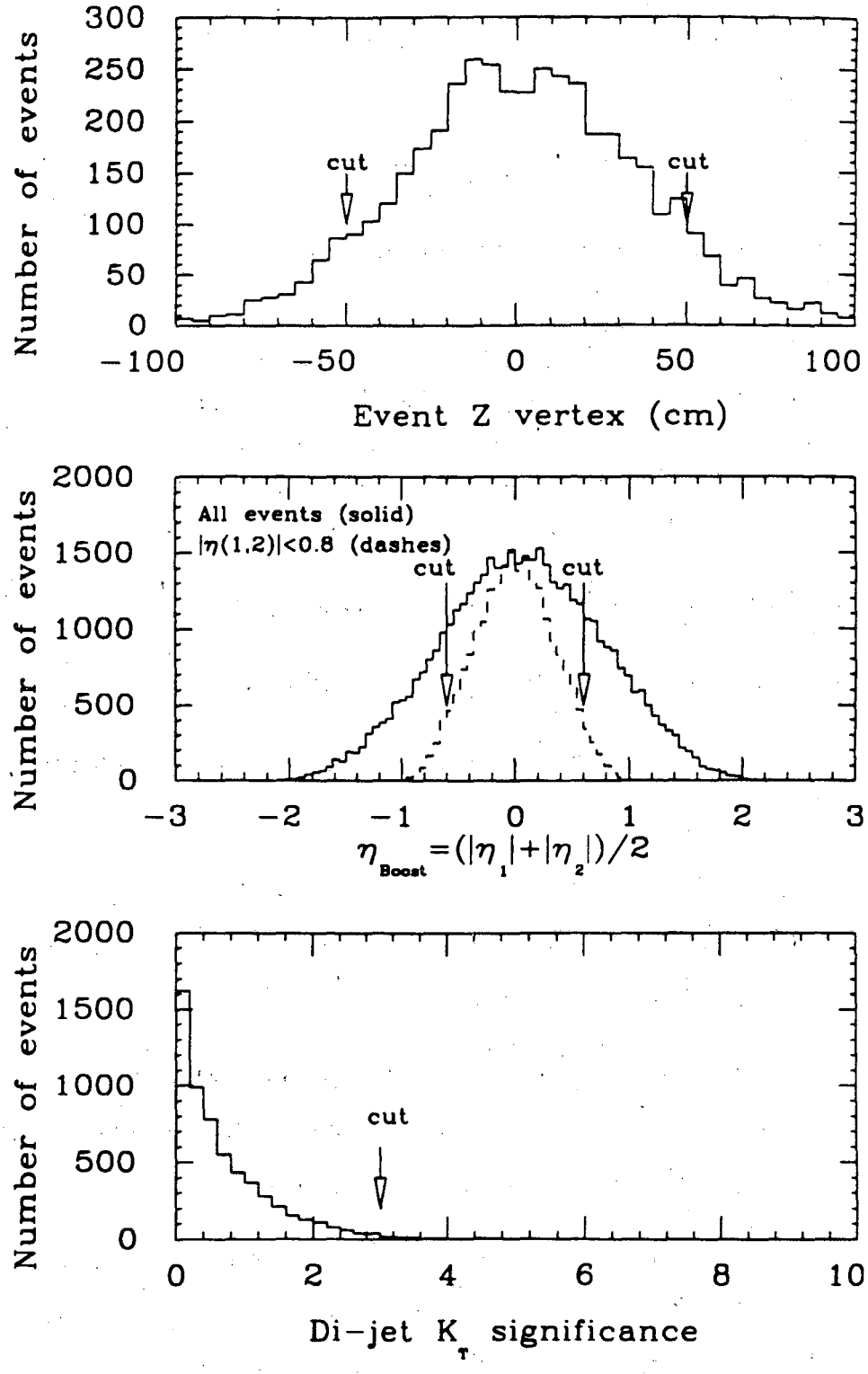

Figure 3.11: a) Event z vertex position. b) Dijet boost rapidity. c) Dijet missing P_T significance.

Chapter 4

Jet Fragmentation Properties

4.1 Definition of Variables and General Issues

In this chapter the following quantities are used to describe charged particle properties in jets:

- $P_{||}$ - the momentum of a particle projected along the jet axis.
- $P_{\perp}$ - the momentum of a particle transverse to the jet axis.
- $Z_P \equiv P_{||}/|P_{jet}|$ - the ratio of the momentum of a charged track along the jet axis to the jet momentum.
- $Z_E \equiv P_{||}/E_{jet}$ - the ratio of the momentum of a charged track along the jet axis to the jet energy. This is more comparable to the fragmentation variable $X_{||}$ that is generally used in e^+e^- experiments.
- $Y \equiv 0.5\ln((E+P_{||})/(E-P_{||}))$ - the rapidity of a particle with respect to the jet axis. E is the energy of a particle assuming a pion mass (139.6 MeV/c^2), since the CTC provides no particle identification.
- $\eta_t \equiv 0.5\ln((|P|+P_{||})/(|P|-P_{||})) = -\ln\tan(\xi/2)$ - the pseudo-rapidity with respect to the jet axis, where ξ is the angle between the axis and the track at the event vertex. This is equivalent to the rapidity for a massless particle.

This chapter focuses on the charged fragmentation function $D(Z) = 1/N_{jets}dN_{charged}/dZ$. The variable Z will generally refer to the momentum fraction Z_P as opposed to Z_E. Z_P is

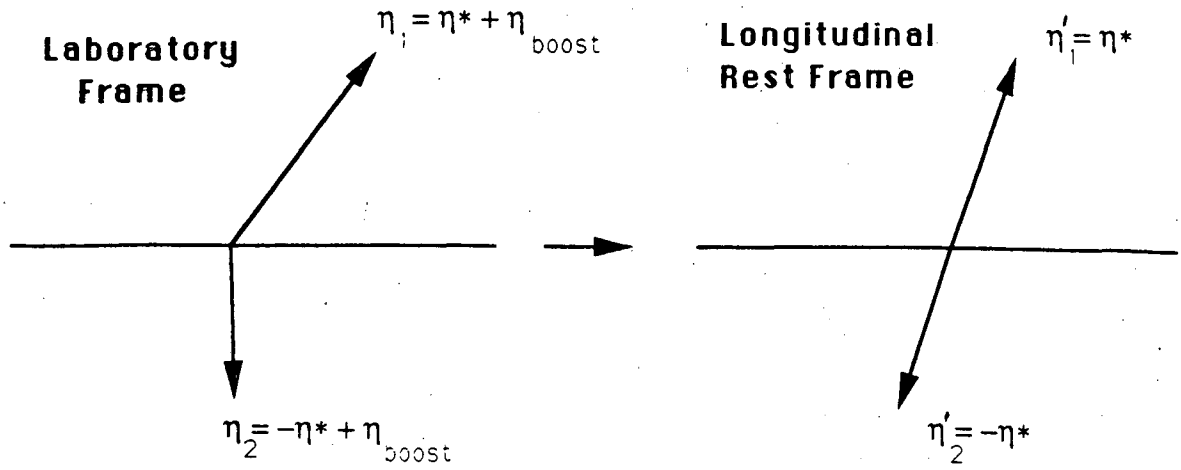

Figure 4.1: Boosting to the longitudinal rest frame of the dijet system

a more natural variable as it is dimensionless and truly 'longitudinal'. The analysis using either choice is nearly identical, and results of the analysis using the two variables will be compared.

The fragmentation properties of the jets are examined in the 'longitudinal rest frame', obtained by a Lorentz transformation of the jets and tracks along the beam line by the dijet boost rapidity $\eta_{boost} = (\eta(\text{jet 1}) + \eta(\text{jet 2}))/2$. As illustrated in Figure 4.1, in the longitudinal rest frame the two jets are back-to-back in η as well as ϕ. Having required $|\eta_{boost}|$ to be less than 0.6, the effect of the transformation is limited. The transformation is not to the dijet center-of-mass frame, since the dijet system in general has net transverse momentum.

For the purpose of examining the Q^2 dependence of the fragmentation properties, events are classified by their dijet invariant mass (M_{JJ}), defined by the relation

$$M_{JJ}^2 = (P(\text{jet 1}) + P(\text{jet 2}))^2 = (E(\text{jet 1}) + E(\text{jet 2}))^2 - (\vec{P}(\text{jet 1}) + \vec{P}(\text{jet 2}))^2 = \hat{s}.$$

Thus, for the parton subprocess, M_{JJ} is analogous to the variable $\sqrt{s}$ used in e^+e^- experiments. The dijet invariant mass is not necessarily the 'correct' variable with which to investigate Q^2 dependence. An equally good variable would have been the jet transverse energy. However, since the events are nearly at rest in the laboratory frame, the jets are at central rapidity, and they approximately balance each other, the relation

$$M_{JJ} \simeq 2E \simeq 2E_T$$

is correct to within 10 or 20 percent.

Track Association

Some tracks in the events come from the jets and others from the fragmenting beam particles (the so-called underlying event) or other radiation or jets (the recoil system). Tracks are associated to a jet if they satisfy the following criteria:

- They pass the track selection (section 2.3.7).
- Their pseudo-rapidity to the jet $\eta_t > 0.8$. This corresponds to a cone in 3-space with opening angle $\xi_{max} = 48°$, chosen to give uniform acceptance in $P_\perp$ for a given $P_{||}$ around the jet axis. Note that this is not the same as a cone in $\eta - \phi$ as was used for clustering.
- Their momentum along the jet axis $P_{||}$ is greater than 0.6 GeV/c, which corresponds to a minimum Z value given the jet momentum. This cut is chosen to keep the track P_T (to the beam axis) greater than 0.4 GeV/c, below which the CTC efficiency falls substantially below unity.

4.2 Corrections to the Raw dN/dZ Distribution

The uncorrected charged fragmentation function $D(Z) = 1/N_{jets} dN/dZ$ is shown in Figure 4.2. Only events in the dijet invariant mass range $80 < M_{JJ} < 140$ Gev/c^2 were included in this plot and other plots unless specified otherwise. The reason for limiting the M_{JJ} range is to limit uncertainties in acceptance and in resolution smearing effects. For each jet, the Z value of each associated track was plotted, using the corrected jet momentum as the denominator in Z. The bins were adjusted for reasonable statistics across the plot, and the value in each bin was divided by the number of jets used and the bin width. There are a small number of tracks where Z is greater than 1.0 (5 out of 48321 in the plot and 4 more above $Z = 1.5$). This unphysical situation might be expected to happen occasionally since the jet and track momenta are independent measurements each with finite resolution.

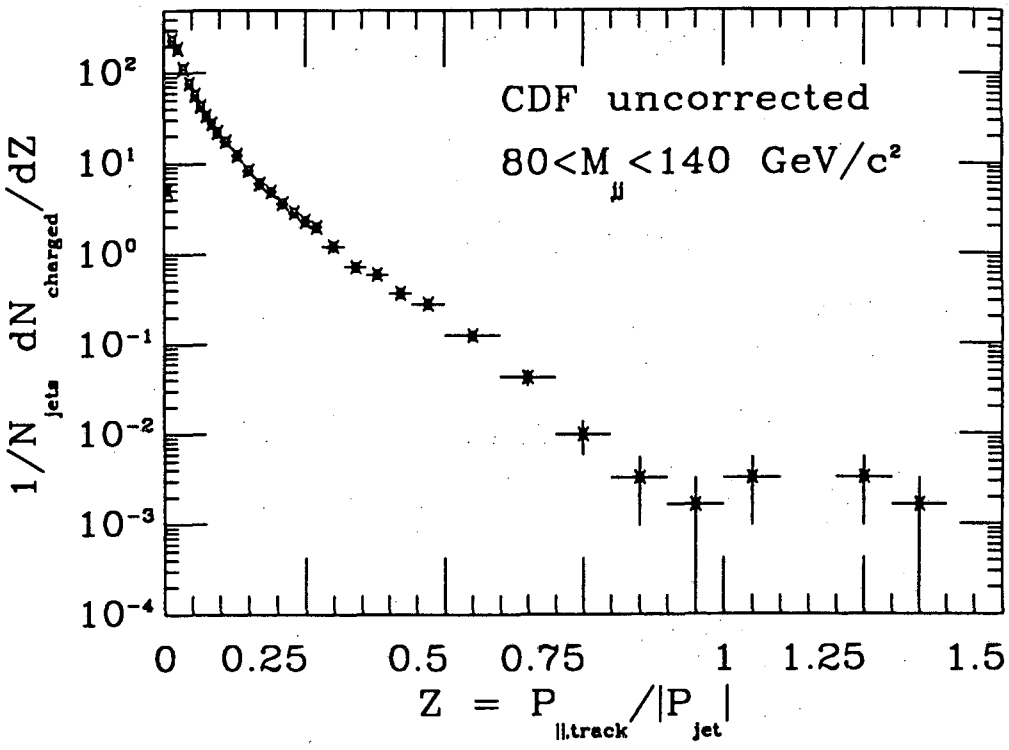

Figure 4.2: Uncorrected charged fragmentation function $D(Z)$. Statistical errors only are plotted.

4.2.1 Acceptance Corrections

As mentioned previously, tracks were required to be within a 48° cone about the jet axis in order to be associated with the jet. This requirement limits acceptance for two reasons:

- CTC acceptance. The association cone is quite large and may partially be outside the full acceptance of the CTC.
- Cone acceptance. The cone requirement places a limit on momentum transverse to the jet axis ($P_\perp$) for a given momentum along the axis ($P_{||}$). Cone acceptance is an issue for the $D(Z)$ distribution which is averaged over $P_\perp$.

The acceptance correction is divided into two parts for the separate effects. Both are evaluated in the longitudinal rest frame.

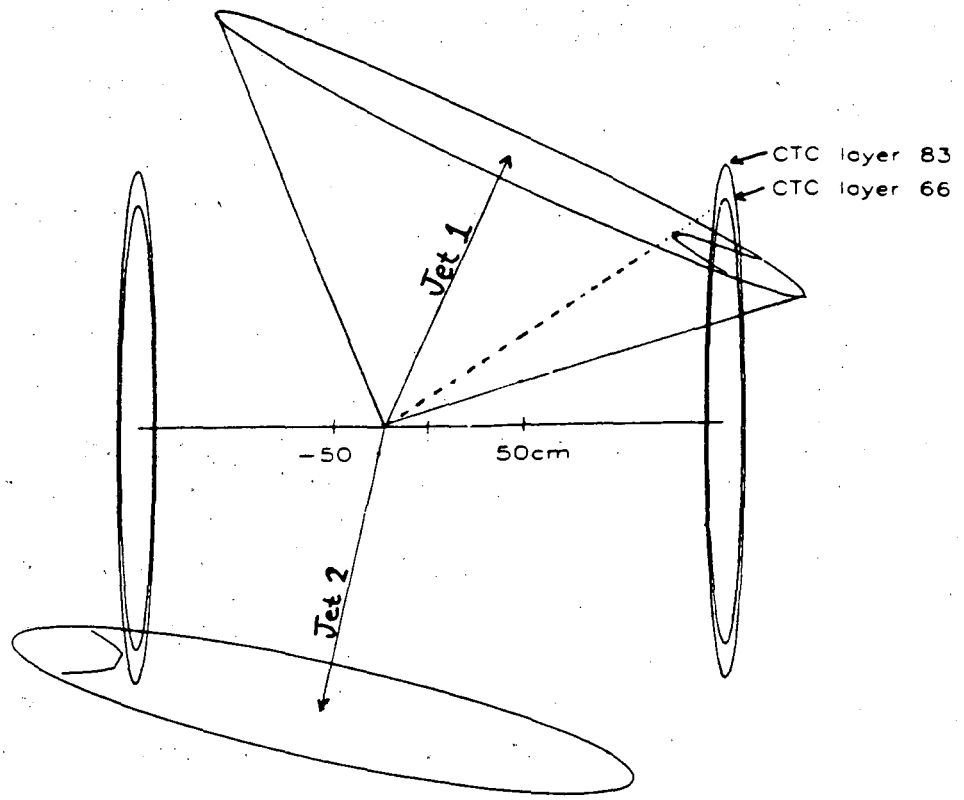

Figure 4.3: Geometry of jet in the CTC, illustrating acceptance region.

CTC Acceptance Correction

The idea behind the correction for CTC acceptance is to avoid looking at tracks in regions where the efficiency is low, falling rapidly, and difficult to estimate. This allows efficiency and acceptance to be dealt with as separate issues. The method, described in Reference [50], assumes azimuthal symmetry of particle production around the jet axis. The full acceptance region is defined to be where a high P_T track will pass through sense wire layer 66 (at a radius of 115 centimeters) before exiting the CTC, chosen such that all tracks within the region pass through at least 4 axial superlayers. Figure 4.3 shows a jet with partial acceptance in the CTC. Tracks outside the acceptance region are ignored. An "acceptance weight" is calculated for tracks within the acceptance region to compensate for lost solid angle.

The calculation of the acceptance weight takes into account the position of the event

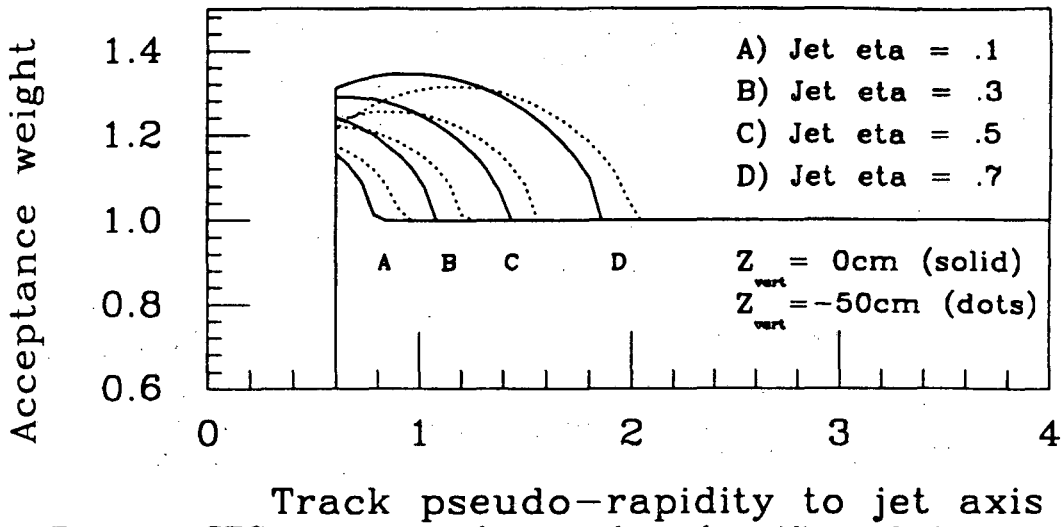

Figure 4.4: CTC acceptance weight vs. track pseudo-rapidity to the jet η_t.

vertex, the longitudinal boost, the direction of the jet and the angle of the track to the jet axis. The acceptance weight is shown at two vertex positions as a function of η_t in Figure 4.4, for several different jet angles. For $\eta_t > 2$ there are no corrections. The correction to dN/dZ from CTC acceptance is $\leq 5\%$ for $Z < 0.05$ and negligible for $Z > 0.05$. A check of the procedure with ISAJET Monte-Carlo data indicated less than 1% uncertainty in $D(Z)$ from CTC acceptance.

Cone Acceptance Corrections (dN/dZ only)

For tracks with momentum $P_{||}$ along the jet axis, the maximum $P_\perp$ which will be within the cone is $P_{\perp,max} = P_{||} \tan 48°$. The acceptance for these tracks with $P_{||}$ integrated over $P_\perp$ is the fraction with $P_\perp < P_{\perp,max}$:

$$A(P_{||}) = \frac{\int_0^{P_{\perp,max}} dN/dP_\perp dP_\perp}{\int_0^{\infty} dN/dP_\perp dP_\perp}$$

The $dN/dP_\perp$ spectrum is approximated by a function of the form:

$$dN/dP_\perp = \alpha P_\perp \exp(-\beta P_\perp)$$

where the parameter β is related to the mean $P_\perp$ of particles to the jet axis:

$$< P_\perp >= \frac{\int_0^{\infty} P_\perp dN/dP_\perp dP_\perp}{\int_0^{\infty} dN/dP_\perp dP_\perp} = 2/\beta$$

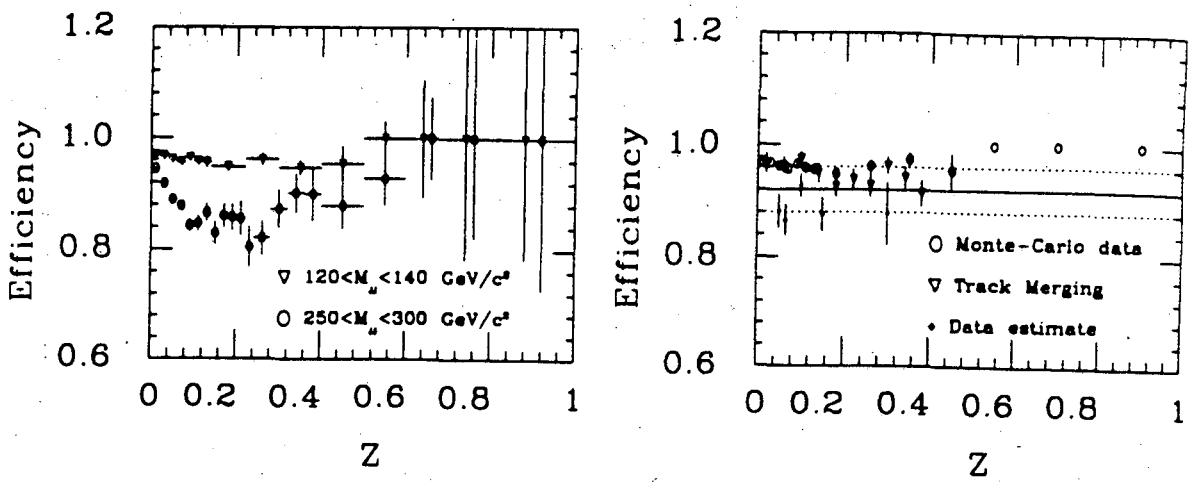

Figure 4.5: a) Monte-Carlo track finding efficiency vs. Z for two intervals in dijet invariant mass. b) Tracking efficiency vs. Z from the three studies.

In fact, the mean $P_\perp$ has been observed to depend on Z[22]. Using the value $< P_\perp >= 0.7$ GeV/c [22] appropriate to low Z, the fractional correction to the dN/dZ distribution to the lowest Z bin is approximately +15%. Uncertainty on the correction, estimated from Monte-Carlo data, may be as high as 50%. This translates to a 7.5% uncertainty to $D(Z)$ for $Z < 0.03$.

4.2.2 Tracking Efficiency

Each distribution is corrected for the efficiency of finding tracks. The efficiency as a function of Z and M_{JJ} was estimated using the methods described in Appendix B. The efficiency at a given Z falls with increasing M_{JJ}, as shown on Figure 4.5a. The sensitivity to this effect and the associated uncertainty is limited by only considering events with M_{JJ} below 200 GeV/c^2. The result from the three efficiency estimates (Monte-Carlo simulation, track merging, and data) are shown in Figure 4.5b for $80 < M_{JJ} < 140$ GeV/c^2. The first two methods illustrate a slow variation with Z, which is not significant given the steep fall of the dN/dZ spectrum. The line at 92% shows the correction applied (independent of Z) for the dN/dZ distribution in this M_{JJ} interval, to which an uncertainty of 4% is assigned. For dN/dZ as a function of M_{JJ} the efficiency is scaled by the observed variation with M_{JJ}

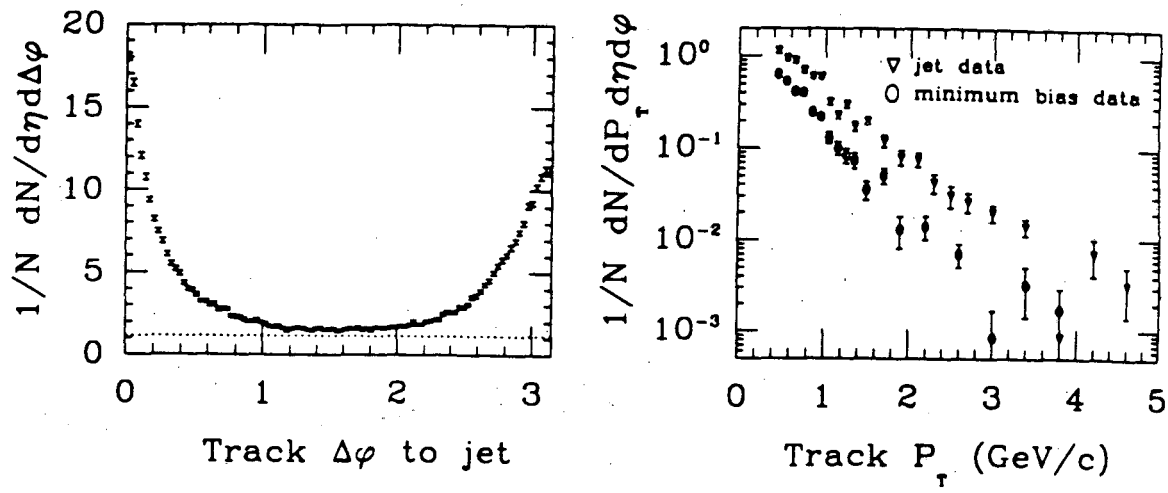

Figure 4.6: a) The track multiplicity vs $\Delta\phi$ to the leading jet. Units are tracks per radian per unit η. The density in minimum bias triggered events is also shown. b) The P_T spectrum of tracks in the underlying event slice compared with that in minimum-bias events.

from the Monte-Carlo estimate.

4.2.3 Underlying Event

The underlying event contributes background tracks uncorrelated to the jet direction. Their contribution to a given distribution was estimated using a simple prescription, and was then subtracted from the same data distribution. Figure 4.6a shows the density of tracks in ϕ with respect to the highest E_T jet in dijet events. The density is strongly peaked in the directions of the jets, indicating that the background underneath the jets is small compared to the signal. In the region of $90\pm15°$ relative to the two jets the density is uniform. This is expected if the underlying event is azimuthally symmetric; however, it is known (from e^+e^- experiments) that some particles from the jets will also enter this region. With this caveat, the tracks contained in this 0.5 radian wide slice are used to estimate the underlying event background level beneath the jets. The track density in minimum-bias triggered events is also shown; it is somewhat lower and has a more steeply falling P_T spectrum than the tracks in this region (Figure 4.6b).

A typical two-jet event is shown schematically in $\eta - \phi$ coordinates in Figure 4.7a. The two jets are shown as circles representing the cones used to associate tracks. When

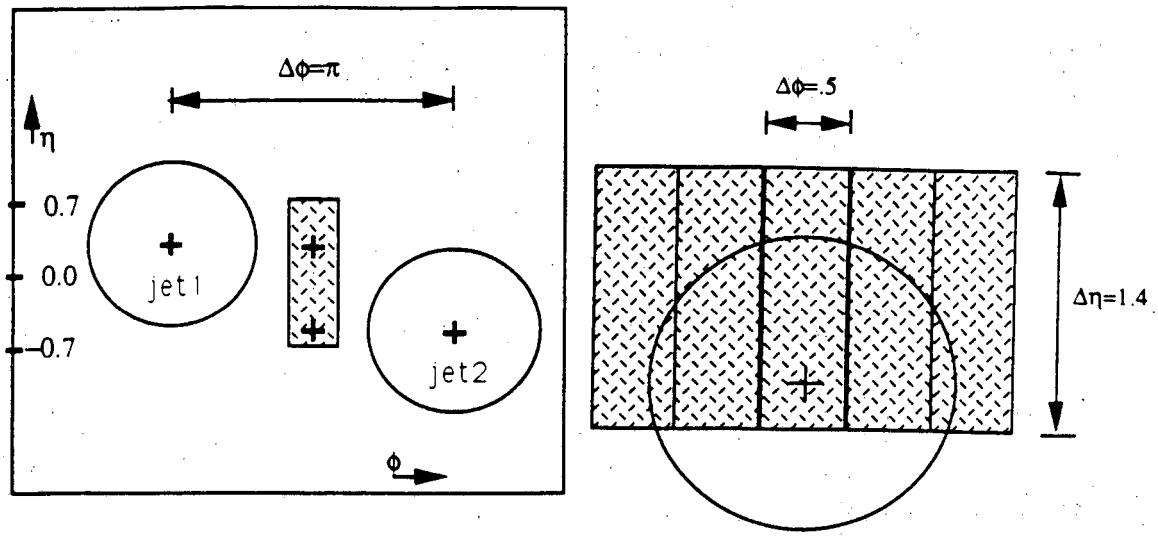

Figure 4.7: a) Diagram of a typical event with two jets. b) Method for evaluation of the underlying event contribution.

plotting a fragmentation distribution of tracks in either jet, the equivalent underlying event distribution is plotted as if the jet axis had been at the same η but rotated by 90° in ϕ. Since the slice is narrower than the association cone, the correct normalization is obtained by translating the slice by its width in ϕ to five positions, as shown in Figure 4.7b.

The underlying event contribution to dN/dZ compared to the data distribution is shown in Figure 4.8a. The correction is very small except in the $Z = 0.025$ bin, where the correction is approximately 20%. As a test of the procedure, the evaluated background was compared to the distribution for particles not associated to jets in ISAJET Monte-Carlo data. As shown in Figure 4.8b, the study indicated that the procedure may overestimate background levels, but the maximum error to $D(Z)$ from the procedure is approximately 10 percent.

4.2.4 Correction for Detector Resolution

The effect of CTC and calorimeter resolution on the dN/dZ spectrum is manifested as a migration of events from one part of the distribution to another. The quantity Z includes both the track and jet momentum, two independent measurements, so the "unsmearing" is a two dimensional problem. The measured number of tracks in a Z interval of width δZ for

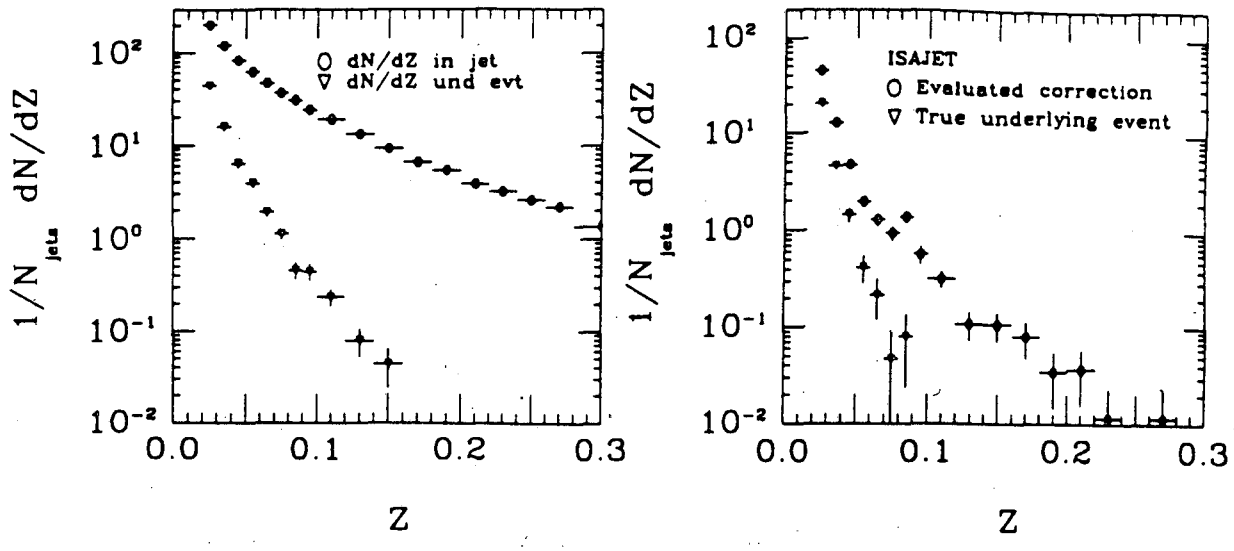

Figure 4.8: a) Underlying event contribution to dN/dZ compared to raw spectrum before subtraction. b) Underlying event correction which was evaluated for the ISAJET M.C., compared to the actual contribution from particles not associated to jets in ISAJET.

jets in a jet momentum interval of width δP_{jet} is expressed as:

$$N_{meas}(Z, P_{jet}) = D_{meas}(Z)\ \delta Z\ \Sigma_{meas}(P_{jet})\ \delta P_{jet}$$

In the above relation, the fragmentation function D is the number of tracks per unit Z per jet and the jet cross section Σ expresses the number of jets per GeV/c per unit luminosity. Since the fragmentation function and jet cross section are both steeply falling distributions, the measured D and Σ will differ from the produced values. The fragmentation function is assumed not to vary with P_{jet} for the purposes of this correction. Though $D(Z)$ is expected to vary logarithmically with P_{jet}^2, this variation is negligible within a small P_{jet} interval.

The correction from measured D_{meas} and Σ_{meas} to produced D_{prod} and Σ_{prod} were obtained using the convolution procedure described in Appendix C. For each Z bin in the distribution, a correction factor D_{prod}/D_{meas} was evaluated. The correction factors are plotted in Figure 4.9, with their estimated uncertainty shown as dotted lines.

For Z below 0.8 the resolution correction is greater than unity, which is caused by the falling jet momentum spectrum. Jets tend to be produced with lower momenta than they are observed. Consequently, tracks tend to have been produced with higher Z value than measured. As Z approaches 1.0, the track momentum resolution becomes increasingly im-

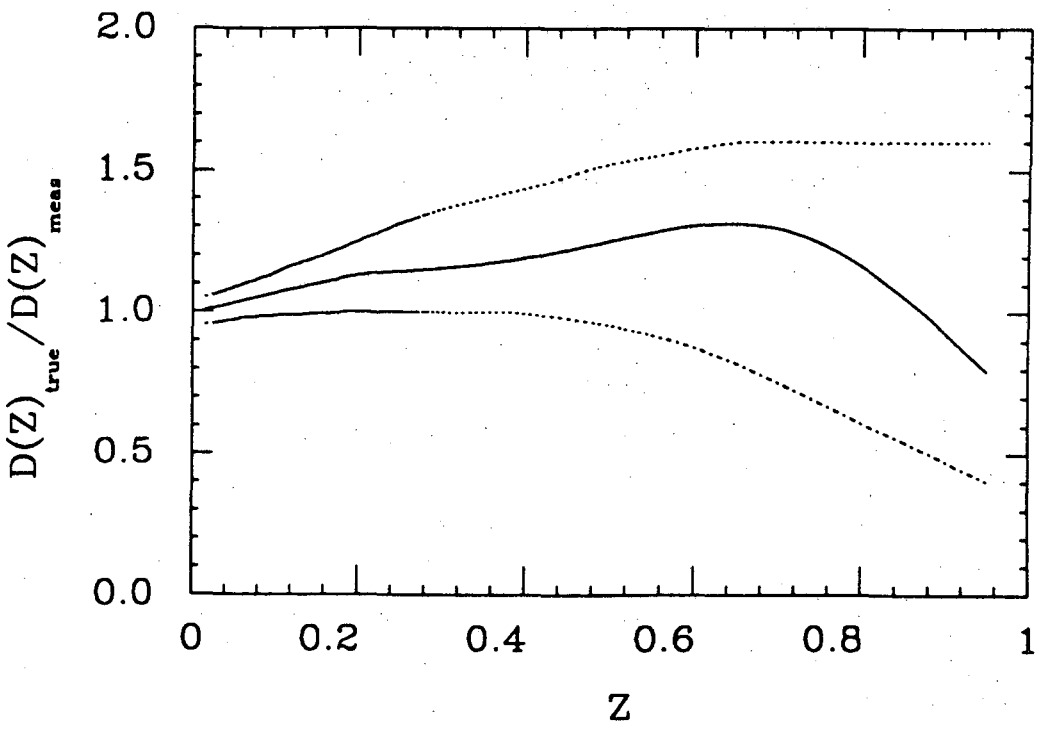

Figure 4.9: Resolution smearing correction to dN/dZ for $80 < M_{JJ} < 140$ GeV/c^2.

portant, and the correction decreases below unity. The shape of the fragmentation function at high Z and the fact that tracks can not be produced with Z greater than unity determine the amount of smearing into and out of a bin. This dependence on the produced fragmentation function causes a substantial uncertainty in the resolution-smearing correction for $Z > 0.8$.

The systematic uncertainty associated with the resolution effects is estimated to be four percent at low Z, twenty percent at $Z = 0.5$, and 100 percent at $Z = 0.9$. The estimated uncertainty takes into account uncertainty in detector resolutions (shown in Figures 2.11 and 3.8a), the uncertainty due to the shape of the produced fragmentation function (Figure C.4b), and the discrepancy between the evaluated corrections and the Monte-Carlo results (Figure C.6).

Table 4.1: Summary of interactive event scanning.

Z interval	# tracks	Comments
$0.7 < Z < 0.8$	13	all good tracks
		2 late interactions (?)
$0.8 < Z < 0.9$	2	good tracks
$0.9 < Z < 1.0$	1	good track, late interaction (?)
$1.0 < Z < 1.1$	1	missing outer 2 superlayers
$1.1 < Z < 1.2$	2	both overlap
$1.2 < Z < 1.5$	2	both overlap
$Z > 1.5$	3	2 overlap
		1 missing many hits

4.3 Backgrounds and Systematic Uncertainties to dN/dZ

4.3.1 Estimation of Backgrounds

There are a number of potential backgrounds to real hadrons in jets. Some are real (non-jet) backgrounds, where the others appear as non-Gaussian tails in either the numerator or denominator of Z. In general, these backgrounds might affect the high Z portion of the dN/dZ distribution given the low rate in that region. Some of the backgrounds can be reliably estimated either from the data or calculated cross sections; these estimates are given below. The events with tracks above $Z = 0.7$ have been scanned interactively to check the estimates and observe the effects of other backgrounds. The results of scanning, summarized in Table 4.1, indicate that backgrounds are less than five per cent for $Z < 0.7$ and up to twenty per cent for $0.7 < Z < 1.0$. Furthermore, the events with Z greater than 1.0 are dominated by gross measurement errors. It should be noted that scanning is somewhat subjective and therefore the estimated level of backgrounds is not subtracted from the distribution.

The backgrounds which were considered are:

- Electrons from Z boson decays, Drell-Yan processes, or conversions. One event consistent with a Z boson decaying to electrons was found in the scan, contributing a track at $Z = 0.7$. This is about the expected level which would pass the event selection

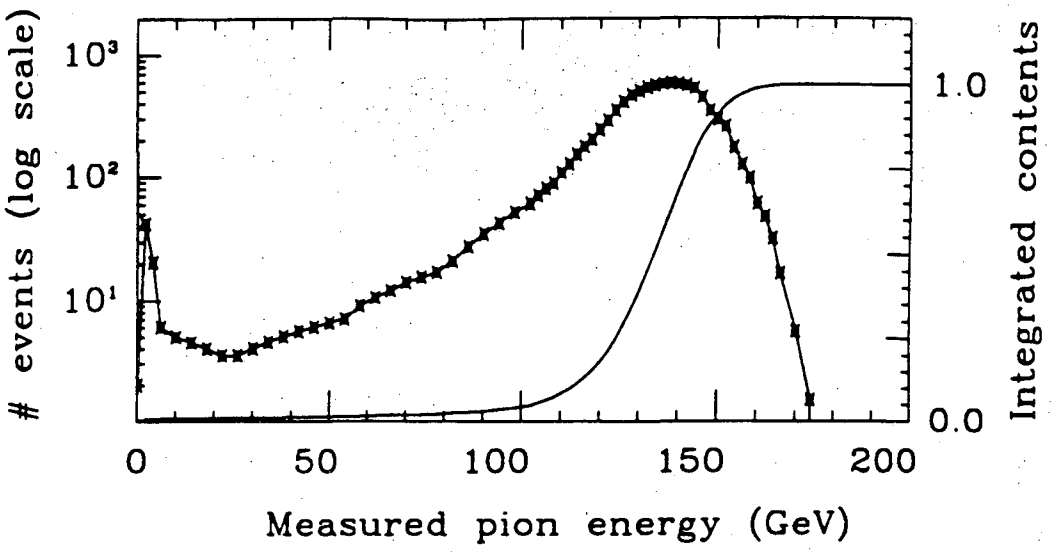

Figure 4.10: Response distribution in the first 5.1 absorption lengths (λ) of an 8 λ calorimeter of 150 GeV test-beam pions. To eliminate muon background, they were required to deposit the full energy in the 8 λ. The data have been suitably smoothed.

from the observed number of $Z \rightarrow e^+e^-$ events recorded during the run. Although an isolated electron would appear as a single particle jet, because of the corrections to the cluster energy, the measured Z value would be less than unity. Approximately three percent of photons from π^0 decays will convert into electron-positron pairs in the material inside the CTC. The conversion electrons are measured at substantially lower Z value than the parent π^0, so the background to $D(Z)$ from these conversions may be neglected.

- Direct Photons. As for electrons these photons could be removed by requiring some hadronic energy. Such a restriction does not affect the shape of the dN/dZ spectrum.

- Non-interacting pions and kaons ('punch-through'). A small fraction of charged hadrons do not shower within the central calorimeter or interact late. These particles register only minimum ionizing signals or a small fraction of the true energy, and can therefore cause a jet's energy to be grossly undermeasured. This phenomenon could in principle be taken into account in the resolution unsmearing by adding a non-Gaussian tail to the resolution function. Instead, the size of the effect was estimated from the data using the response distribution from test-beam pions (Figure 4.10). A

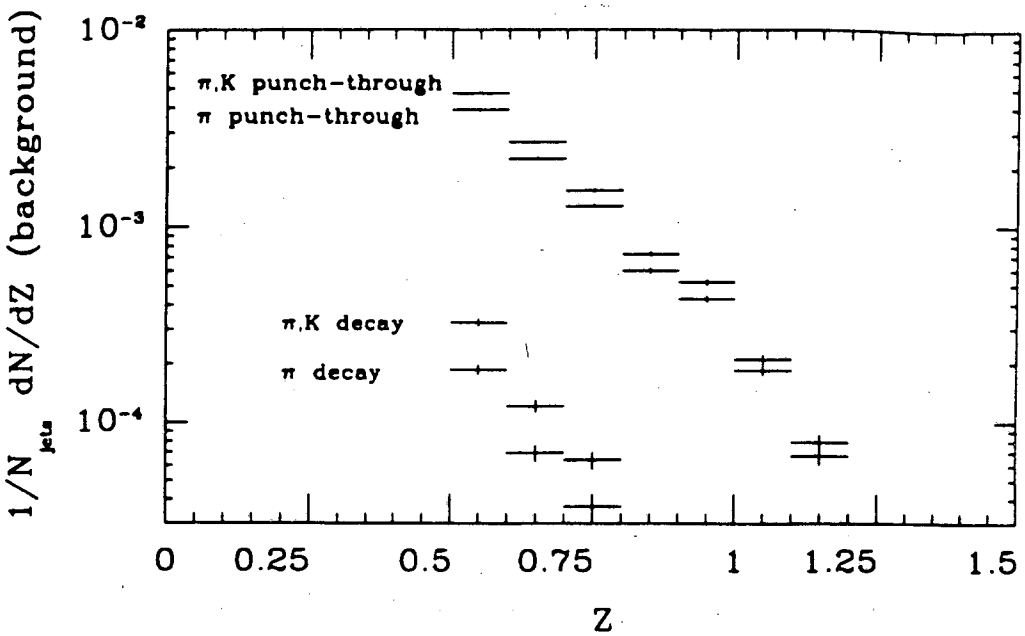

Figure 4.11: Background dN/dZ distribution from punch-through and decays.

background dN/dZ distribution was calculated using each track above $Z = 0.1$ in the data, allowing a fraction of the particle's energy to be deposited with the correct probability. The jet momentum was recalculated, and dijet missing P_T significance cut was imposed (Section 3.4. The normalized dN/dZ background distribution is shown in Figure 4.11, where it has been assumed that either all particles are pions or that twenty percent are kaons. The latter assumption gives a higher background estimate because of the 25% smaller inelastic cross section for K^+. The number of predicted events is roughly consistent with the small number of events at high Z observed with activity in the muon chambers outside the calorimetry.

- Muons or neutrinos from pion and kaon decays. The background to dN/dZ at high Z values from pions and kaons decaying into muons was calculated using the same technique used for the punch-through estimate. The result is negligible, as shown in Figure 4.11.

- Central calorimeter phi crack response. Within one degree of a ϕ boundary of a 15 degree wedge the calorimeter response is low and as many as ten percent of hadrons fail to interact. The contribution to dN/dZ from this effect has been estimated by

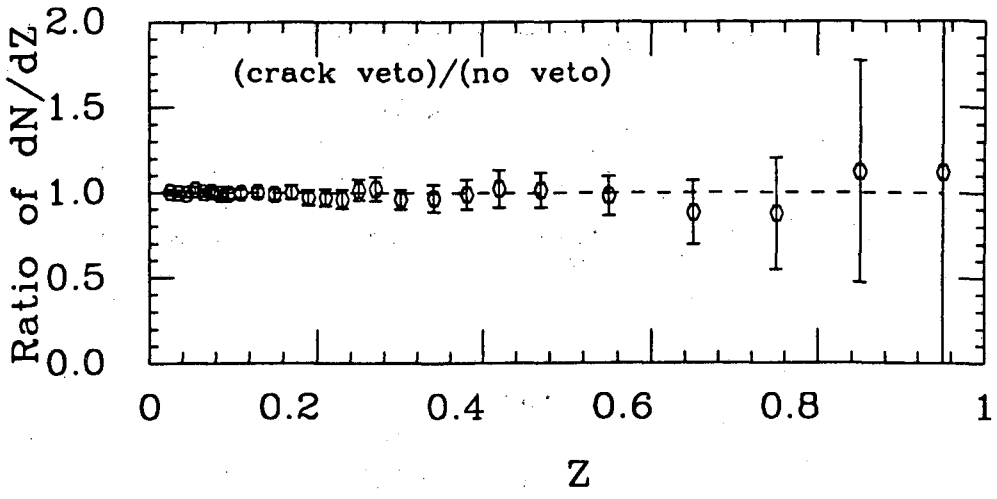

Figure 4.12: Effect of central ϕ cracks. Ratio of dN/dZ with and without crack veto, where we require that the highest P_T track not be within 1° of a ϕ crack.

rejecting jets in which the highest P_T track (to the beam) penetrates the calorimeter within one degree of a crack, which amounts to a 2/15 rejection factor independent of Z. Figure 4.12 illustrates the ratio of the dN/dZ distribution obtained with and without this cut, and there is no evidence of any measurable effect at the three percent level. The effect of the phi cracks is therefore considered to be small.

- False tracks, or non-Gaussian tails in tracking P_T resolution. The contribution of these tracks is difficult to estimate except by event scanning, because it depends (among other things) on the details of the pattern recognition software. The number of false or poorly measured tracks is minimized by the track selection cuts (section 2.3.7), particularly the impact parameter and RMS residual cuts. In the scanning two rules were used to label a track as false or poorly measured:

  1. Overlap. Two tracks overlapped each other very closely in $r - \phi$ through most of the CTC. In this case it is difficult to determine which hits belong to which track by scanning, so one might assume that the pattern recognition program could make the wrong choice, and therefore measure the momenta poorly.

  2. Many missing hits. Many hits which should be part of a track are either not used or not visible in the event display. The effective track length is shortened

so that the momentum resolution for the track is significantly degraded.

All the tracks above $Z = 1.0$ fail one of these two tests and are suspected to be bad tracks. One interesting feature of these tracks that their momenta all change drastically between the vertex constrained and unconstrained fits, which is not generally the case.

4.3.2 Estimation of Systematic Errors

The various contributions to systematic error in dN/dZ are :

- Jet corrections systematic uncertainty. The contribution to $D(Z)$ uncertainty from the jet corrections has been evaluated using the upper and lower jet correction estimates shown in Figure 3.5. The ratios of the dN/dZ distribution with these estimates to the nominal distribution is plotted in Figure 4.13. The ratio using the high estimate is less than unity, since a larger correction causes Z to be smaller. The two curves show the estimated uncertainty as a function of Z. This uncertainty is the largest contributor to systematic error to dN/dZ for most of Z.

- Uncertainty from resolution smearing (Figure 4.9). For $Z > 0.8$ the resolution uncertainty becomes comparable to the energy scale uncertainty. For this reason the results above $Z = 0.8$ are not reliable except to place an upper limit on the actual value.

- Uncertainty from boosting, acceptance and underlying event subtraction. These are the dominant sources of uncertainty for $Z < 0.05$.

- Uncertainty in tracking efficiency. This is estimated to be four percent, independent of Z.

Figure 4.14 summarizes the various contributions and gives the fractional systematic error of those contributions added in quadrature.

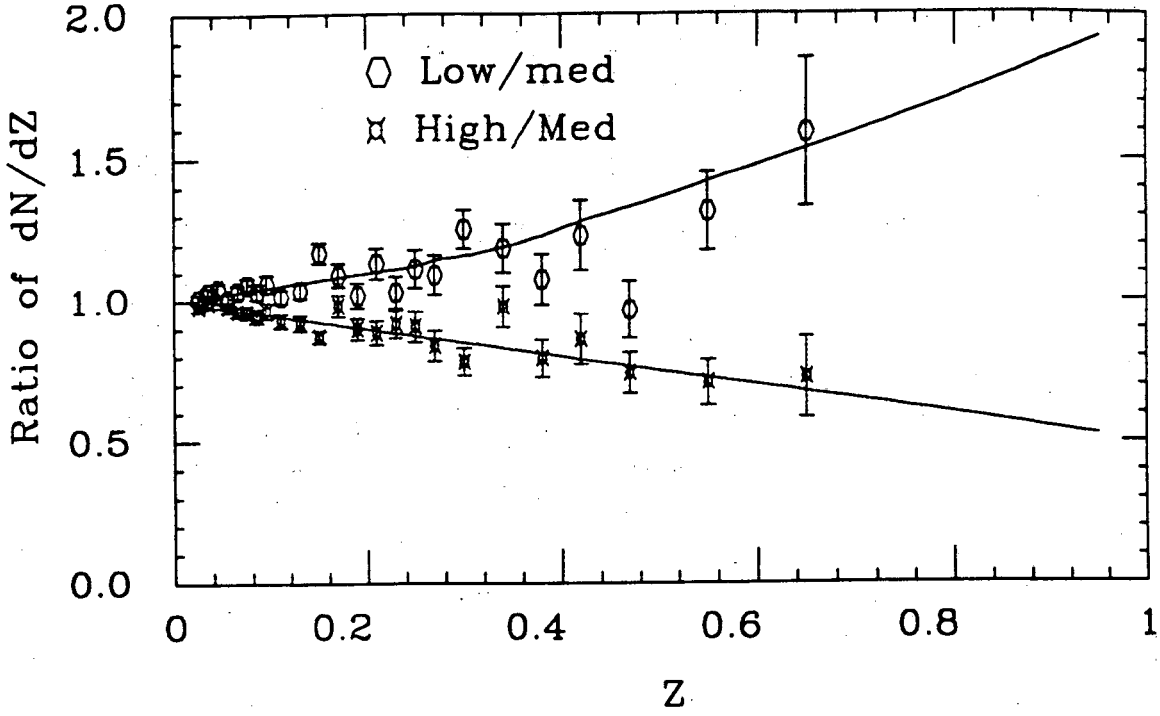

Figure 4.13: Systematic error to dN/dZ from uncertainty in jet corrections. The ratio of values of dN/dZ using the high and low estimates to the nominal distribution is plotted. The dashed lines give the estimated systematic uncertainty.

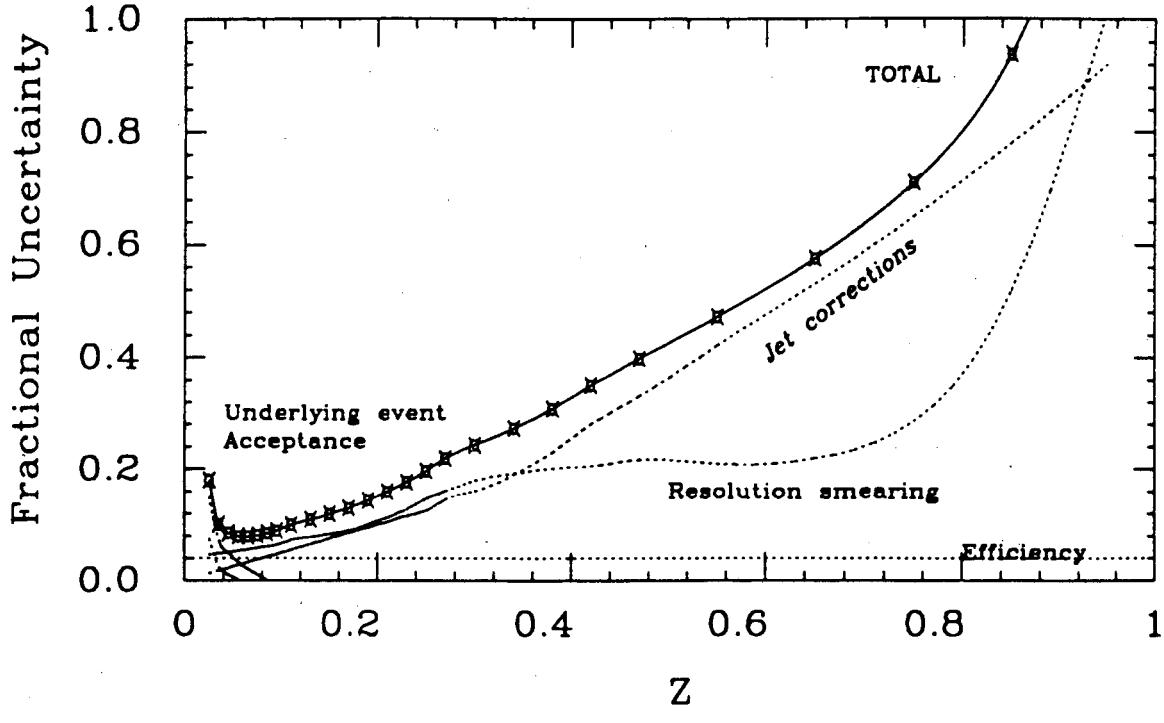

Figure 4.14: Summary of systematic uncertainty to the dN/dZ spectrum.

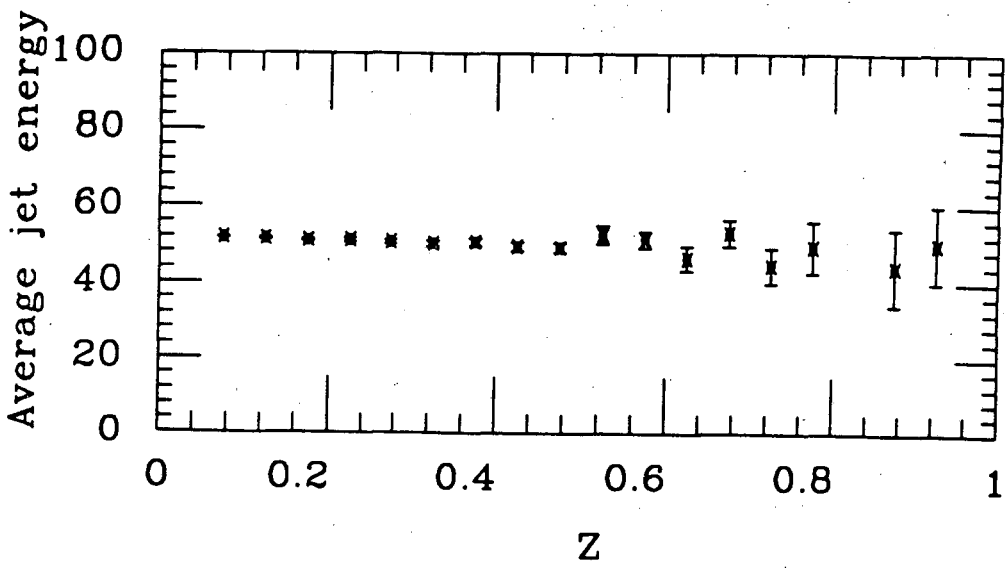

Figure 4.15: Average jet energy as a function of Z.

4.3.3 Consistency Checks

Several checks have been performed. These include varying the fiducial volume, tightening the event selection criteria, vetoing the ϕ crack regions and eliminating the boost. These all gave nearly identical results as did the standard procedure. One particularly useful check was to examine the average jet energy as a function of Z to evaluate whether or not the high Z portion of the distribution is caused by grossly undermeasured jets. The result of this study is shown in Figure 4.15. The slow variation with Z may be physical, since for higher energy jets, a slightly higher multiplicity may be expected.

4.4 Results

4.4.1 dN/dZ

The corrected charged fragmentation function for $80 < M_{JJ} < 140$ GeV/c^2 is listed in Table 4.2 and plotted in Figure 4.16. Two predictions of the HERWIG 3.2 Monte-Carlo program are also shown. The dashed curves is the fragmentation function using the mixture of quark and gluon initiated jets as given by the Duke-Owens set 2 structure functions[51], and the dotted curve is for gluon initiated jets only. The predicted gluon fragmentation

Table 4.2: Charged fragmentation function $D(Z)$ for $80 < M_{JJ} < 140$ GeV/c^2. Statistical and systematic errors are listed separately.

Z	$D(Z) \pm (\text{stat}) \pm (\text{sys})$	Z	$D(Z) \pm (\text{stat}) \pm (\text{sys})$
0.02-0.03	$163. \pm 2. \pm 30.$	0.22-0.24	$3.6 \pm 0.2 \pm 0.7$
0.03-0.04	$107. \pm 2. \pm 11.$	0.24-0.26	$3.0 \pm 0.2 \pm 0.6$
0.04-0.05	$78.2 \pm 1.3 \pm 6.8$	0.26-0.28	$2.5 \pm 0.2 \pm 0.5$
0.05-0.06	$59.8 \pm 1.2 \pm 4.9$	0.28-0.32	$1.57 \pm 0.09 \pm 0.38$
0.06-0.07	$46.5 \pm 1.0 \pm 3.8$	0.32-0.36	$0.92 \pm 0.07 \pm 0.25$
0.07-0.08	$36.9 \pm 0.9 \pm 3.2$	0.36-0.40	$0.76 \pm 0.06 \pm 0.23$
0.08-0.09	$31.6 \pm 0.8 \pm 2.8$	0.40-0.44	$0.50 \pm 0.05 \pm 0.17$
0.09-0.10	$25.1 \pm 0.7 \pm 2.4$	0.44-0.50	$0.37 \pm 0.04 \pm 0.15$
0.10-0.12	$20.3 \pm 0.5 \pm 2.1$	0.50-0.60	$0.18 \pm 0.02 \pm 0.09$
0.12-0.14	$14.3 \pm 0.4 \pm 1.7$	0.60-0.70	$0.06 \pm 0.01^{+0.03}_{-0.02}$
0.14-0.16	$10.1 \pm 0.3 \pm 1.3$	0.70-0.80	$0.014^{+0.008+0.010}_{-0.006-0.007}$
0.16-0.18	$7.3 \pm 0.3 \pm 1.0$	0.80-0.90	$0.0038^{+0.0042+0.0036}_{-0.0021-0.0021}$
0.18-0.20	$6.0 \pm 0.3 \pm 0.9$	0.90-1.00	$0.0014^{+0.0028+0.0020}_{-0.0014-0.0008}$
0.20-0.22	$4.4 \pm 0.2 \pm 0.8$		

function falls substantially below that of the quark/gluon mixture for $Z > 0.4$. In view of the differences between the quark and gluon $D(Z)$ in the model, the agreement of the combined prediction with the data is remarkable.

Direct comparison between the CDF result and e^+e^- experimental data can be misleading, due to differences in definition between the fragmentation variables used in those experiments. Typically they use the half the center-of-mass energy as the denominator of Z, without an explicit jet definition. Effects of multi-jet events and internal jet masses cause this quantity to differ from the variable Z_P defined using the jet momentum. This difference is illustrated in the ratio of the fragmentation function using Z_P to that using Z_E (Figure 4.17). Though the difference between the jet energy and momentum is typically a few per cent, the effect is magnified by the slope of the $D(Z)$ distribution. The same ratio predicted by HERWIG is also shown, and agrees qualitatively with the data.

4.4.2 Evolution with Dijet Invariant Mass.

The dijet invariant mass M_{JJ} was used as an estimator of the hard scattering momentum transfer scale to look for deviations from scaling. Over the wide M_{JJ} range accessible one

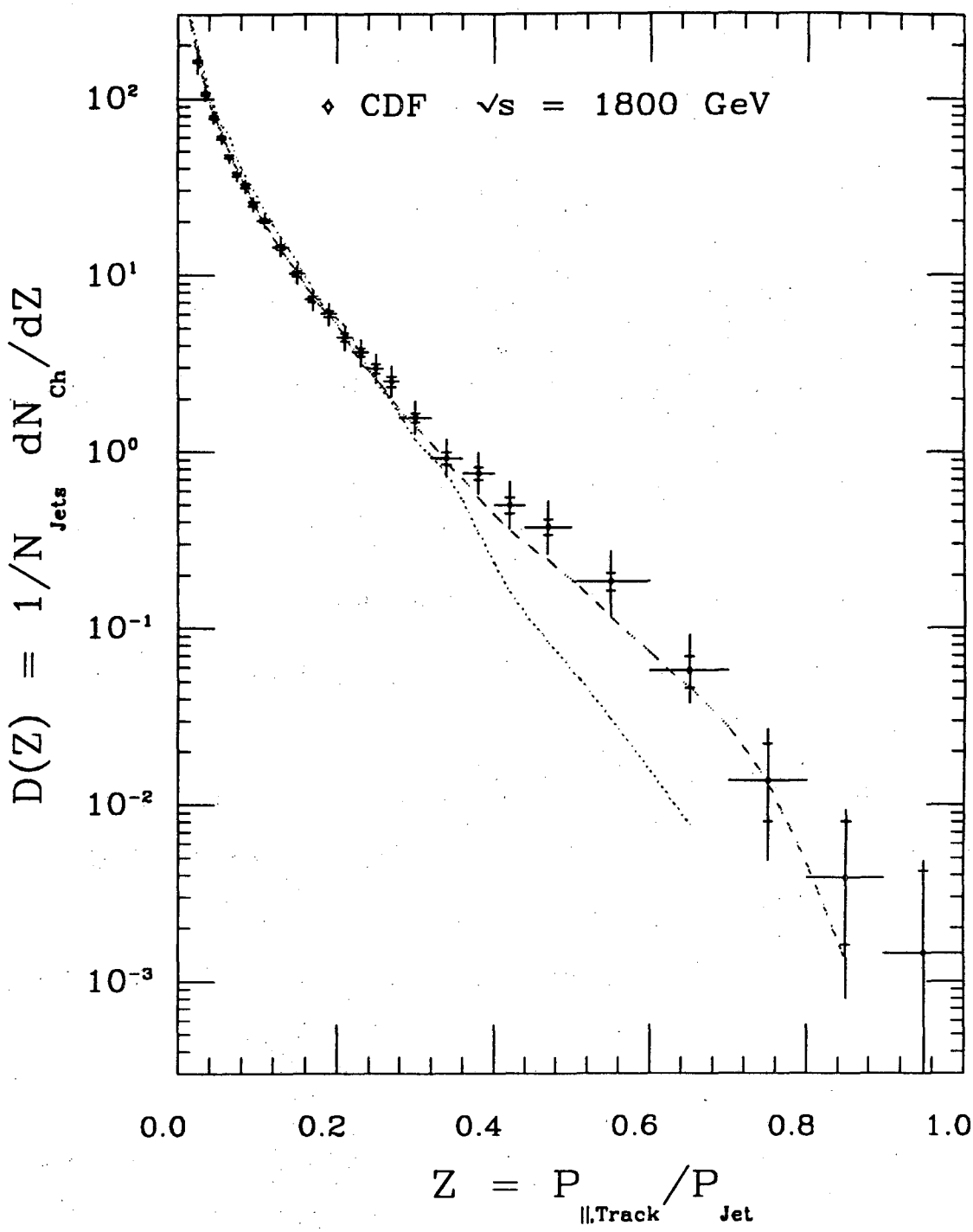

Figure 4.16: Charged fragmentation function $D(Z)$. The CDF data have statistical and systematic errors indicated. The curves are HERWIG 3.2 Monte-Carlo predictions for gluon jets only (dots) and for the quark/gluon mixture from Duke-Owens set 2 structure functions (dashes).

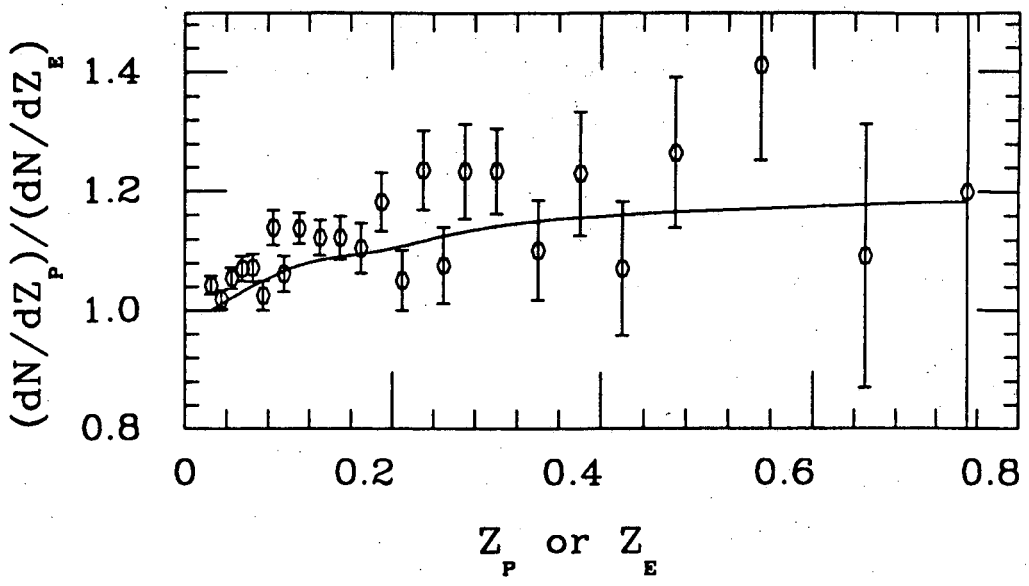

Figure 4.17: Ratio of dN/dZ_P to dN/dZ_E. Also shown is the prediction of HERWIG.

may expect observed deviations to be due to three potential effects:

- For a given jet type the fragmentation function is predicted in QCD to become steeper with increasing Q^2.
- The ratio of quark to gluon initiated jets is expected to rise with increasing Q^2. If this variation were the only effect, one might expect the fragmentation function to become less steep.
- Experimental effects such as efficiencies, calorimeter response and detector resolutions change over the large Q^2 range. The corrections for these effects were evaluated separately for each M_{JJ} interval.

The behavior of the fragmentation function with M_{JJ} is shown in Figure 4.18, compared to data from TASSO[52]. The plot is similar to those used to describe structure function evolution. The horizontal axis is logarithmic in M_{JJ}^2 for the CDF data or s for TASSO. The CDF data are the circles, with statistical errors plotted for each point. For six values of M_{JJ} a coarsely binned dN/dZ distribution is shown as a vertical set of points. Likewise, the horizontal groups show the variation of $D(Z)$ for six Z intervals. Typical systematic errors are shown at the right side of the plot.

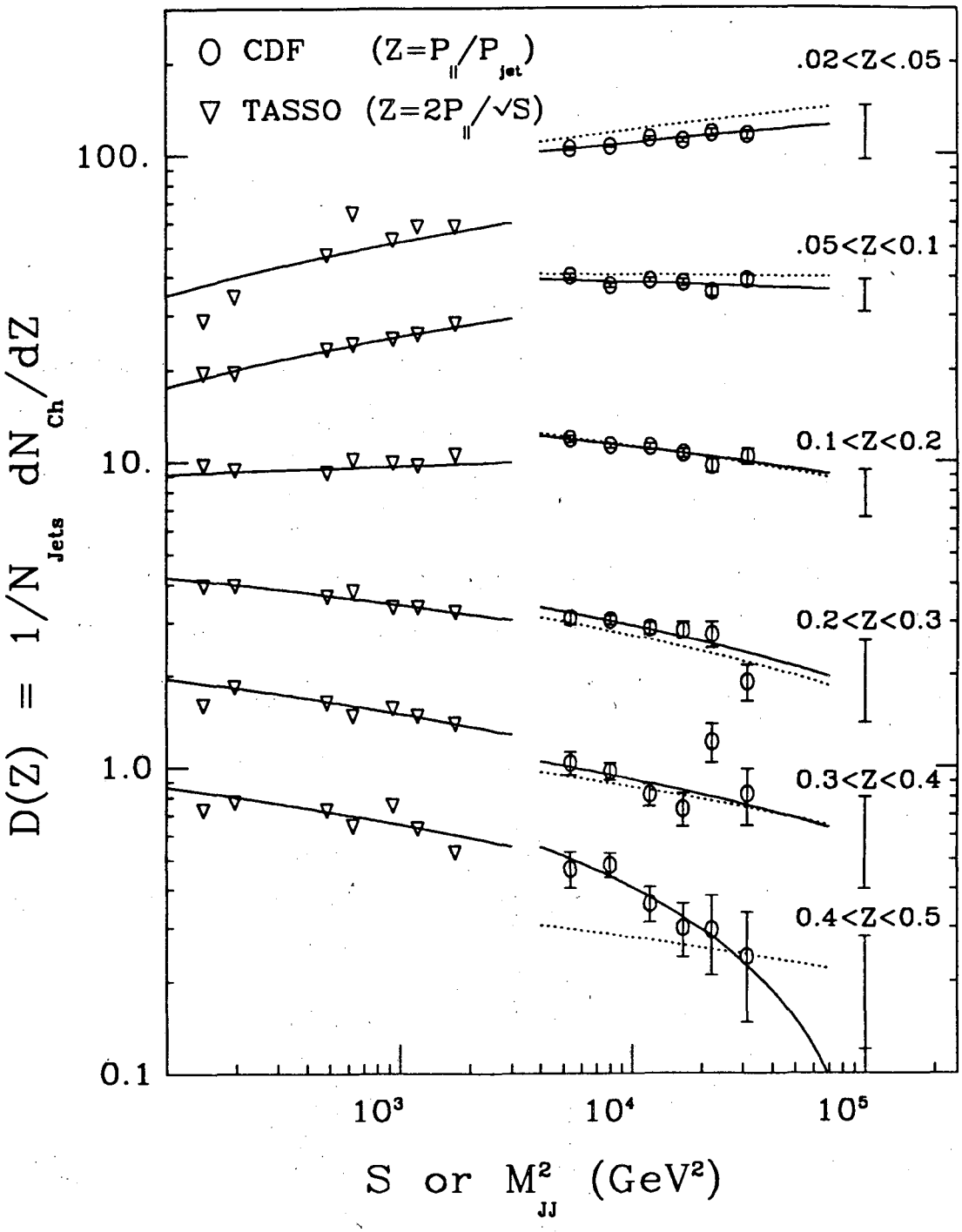

Figure 4.18: Evolution of the fragmentation $D(Z)$ with M_{JJ} (CDF) or S (TASSO) for six Z intervals. The CDF data (circles) have statistical errors plotted, with typical systematic errors shown at the right. The solid curves are fits described in the text, and the dotted curves are HERWIG 3.2 predictions.

For each experiment, the fragmentation is observed to steepen with increasing M_{JJ}^2. The prediction of the HERWIG Monte-Carlo model is plotted as dotted curves, showing qualitative agreement with the CDF data. For each Z interval, the solid lines plotted through the two experimental data sets are linear fits of the form:

$$D(Z_i, Q^2) = \gamma_i + \delta_i \ln(Q^2)$$

where the Q^2 variable is approximated as M_{JJ}^2 for CDF and s for TASSO. In fact there is theoretical ambiguity in adopting a common Q^2 definition between the different experiments, so detailed comparison between the two such as a combined fit is not warranted. However within a given experiment the curves describe variations approximately linear in $\ln(Q^2)$. The CDF slopes δ are statistically inconsistent with the assumption of perfect scaling.

In the lowest Z interval the CDF data are significantly higher than the TASSO data. This feature is interesting in view of the fact that the TASSO jets are predominantly quark initiated, whereas the CDF jets are expected to be mostly gluons. However, the theoretical uncertainties and experimental differences mentioned above prevent a quantitative comparison of the two.

4.4.3 Extraction of $< f_{ch} >$

The fraction of jet momentum carried by charged particles $< f_{ch} >$ is given by the sum rule:

$$< f_{ch} >= \int_0^1 dZ Z D(Z)$$

If isospin was a perfect symmetry in nature and only pions were produced, this fraction would be 2/3. However, the effects of resonance decays may cause $< f_{ch} >$ to deviate from that value. The mean charged fraction is extracted from the $D(Z)$ result by the numerical integral:

$$< f_{ch} > \simeq \sum_i Z_i D_i(Z) \Delta Z + \int_{0.0}^{0.02} D_{prod}(Z)$$

The distribution is extrapolated below the first data point using the fit parametrization. Figure 4.19 shows the charged momentum fraction numerically integrated up to Z for events

in the range $80 < M_{JJ} < 140$ GeV/c^2. The contribution from Z values above 0.4 is less than two per cent. Thus the dependence on the fit parametrization used to correct $D(Z)$ is negligible, since the correction factors deviate substantially above $Z = 0.4$. Also, the extrapolation below $Z = 0.02$ contributes an additional two per cent uncertainty according to ISAJET. The error bar shows the statistical error and the combined statistical and systematic error added in quadrature.

The CDF $< f_{ch} >$ of 0.65±0.02(stat)±0.08(sys) is shown compared to TASSO[52] and UA1[22] results in Figure 4.20. The choice of Z variable definition is important. The CDF charged fraction using the Z_E variable (not shown) is approximately ten percent lower than the equivalent result using Z_P. Within statistical uncertainties the value of $< f_{ch} >$ does not depend on M_{JJ}. The CDF and TASSO results are consistent across the large energy range, given the differing definitions for the fragmentation variable and the size of the systematic error. The CDF mean value appears to be inconsistent with the UA1 result of 0.47±0.02(stat)±0.05(sys).

4.5 Transverse Fragmentation Properties

The rapidity and transverse momentum distributions of charged particles with respect to the jet axis have also been investigated. These quantities do not depend directly on the magnitude of the jet momentum, so they are not sensitive to energy scale errors. However, they depend sensitively on the jet axis determination. Corrections and systematic uncertainties related to jet angular measurement errors have not been evaluated for these distributions.

4.5.1 Transverse Momentum Distribution

The transverse momentum distribution of charged particles to the jet axis is plotted in Figure 4.21a, for events with M_{JJ} between 100 and 120 GeV/c^2. Only particles with $Z > 0.1$ are included. The underlying event background distribution, evaluated at 90 degrees in ϕ from the jets (Section 4.2.3), is also plotted. Below 3 GeV/c the underlying

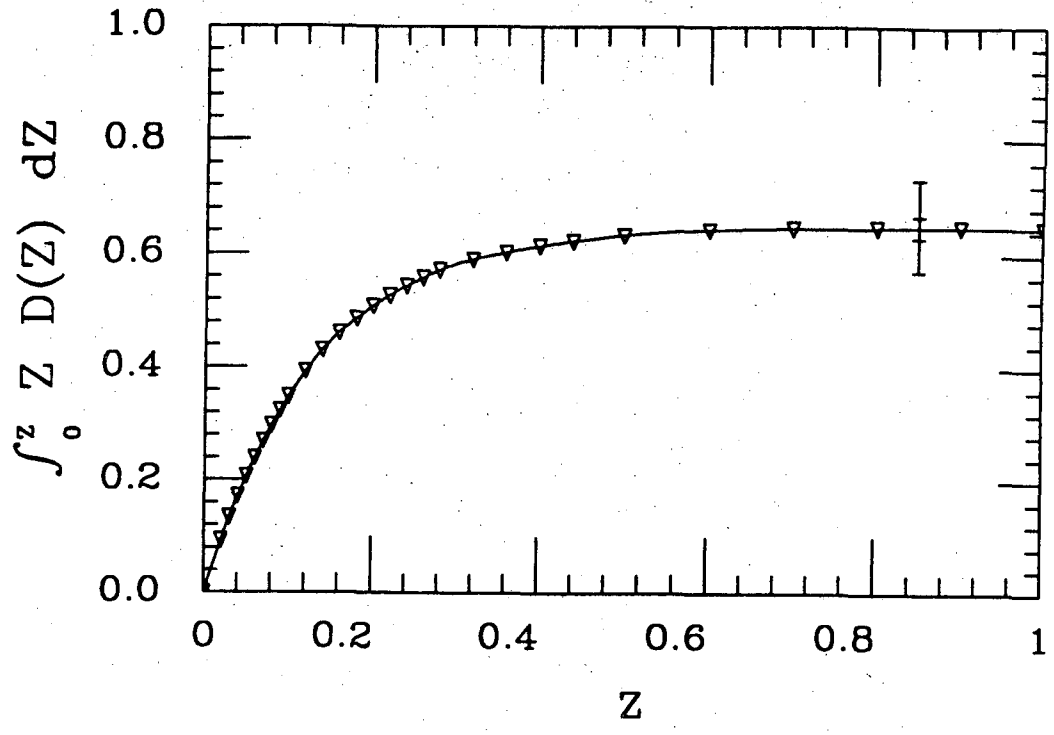

Figure 4.19: Charged fraction integrated numerically.

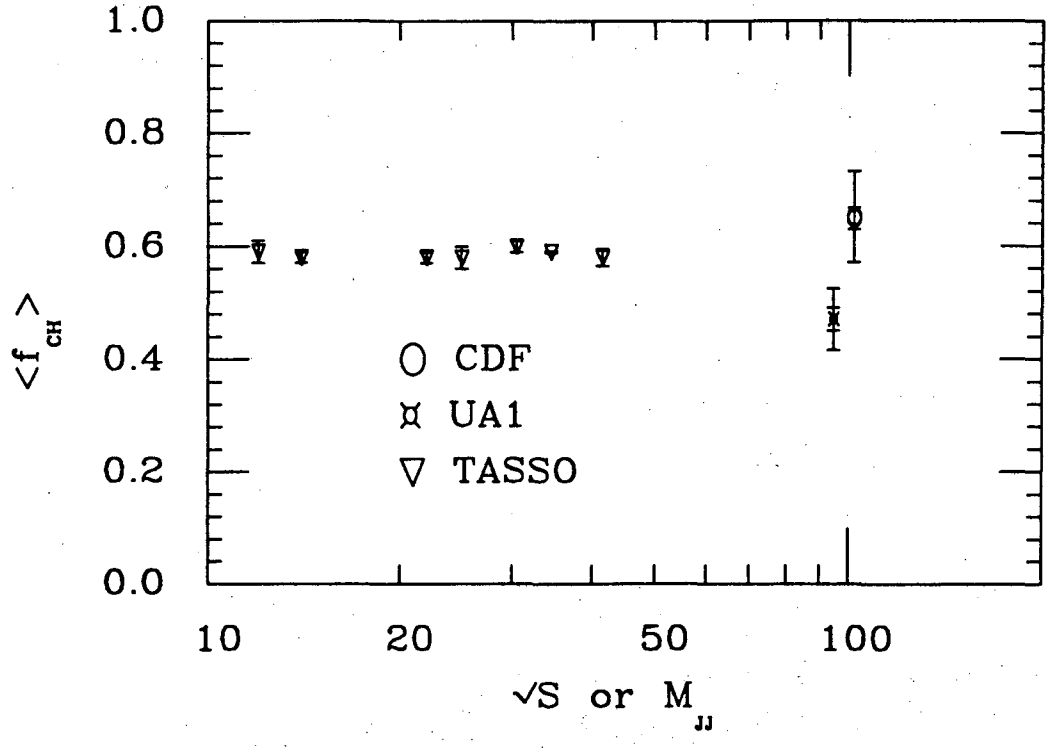

Figure 4.20: Average charged momentum fraction, compared with previous measurements.

event is negligible because of the $Z > 0.1$ requirement. For a given lower Z limit and jet momentum, the track association cone imposes a limit to $P_\perp$ acceptance; this limit corresponds to approximately 5 GeV/c for $M_{JJ} > 100$ GeV/c^2.

At low $P_\perp$, the $dN/dP_\perp$ distribution is forced to zero, as a result of phase space that increases linearly with $P_\perp$. In Figure 4.21b, this phase space factor is removed by plotting $1/P_\perp \; dN/dP_\perp = 2 \; dN/dP_\perp^2$, rather than $dN/dP_\perp$. To examine the effect of jet axis angular resolution, the data are plotted for two definitions of the jet axis: the axis from the calorimeter clustering algorithm; and the axis determined by the momentum sum of charged tracks associated with the jet. The two axis definitions give significantly different results at low and at high $P_\perp$. For $P_\perp < 0.5$ GeV/c, the distribution approximately 50 percent lower for the calorimeter axis than for the tracking axis, and for $P_\perp > 3.0$ GeV/c the distribution is higher for the calorimeter axis. This is consistent with the expectation that the axis determined by tracking is more precise than that determined by calorimetry.

In Figure 4.21c, the transverse momentum distribution is plotted for three dijet invariant mass intervals. For $P_\perp$ values below 1 GeV/c, The multiplicity with $Z > 0.1$ is lower for the higher M_{JJ} intervals. This may be due to the effective $P_\perp$ resolution, which worsens with increasing $P_\parallel$ at a constant angular resolution. Quantitative comparison of the distribution with other experiments or for different values of Z or M_{JJ} would require the systematic effects from the jet axis determination to be better understood.

4.5.2 Charged Particle Rapidity Distribution

The rapidity distribution of charged tracks to the jet axis is shown in Figure 4.22a for $100 < M_{JJ} < 120$ GeV/c^2. In the calculation of the rapidity (Y), all particles are assumed to be pions, since the CTC provides no particle identification. The background rapidity distribution of underlying event particles, which has been subtracted from the distribution, is plotted as circles. The underlying event subtraction forces the distribution towards zero at $Y = 0$. The distribution is shown for two values of the $P_\parallel$ track association cut. The

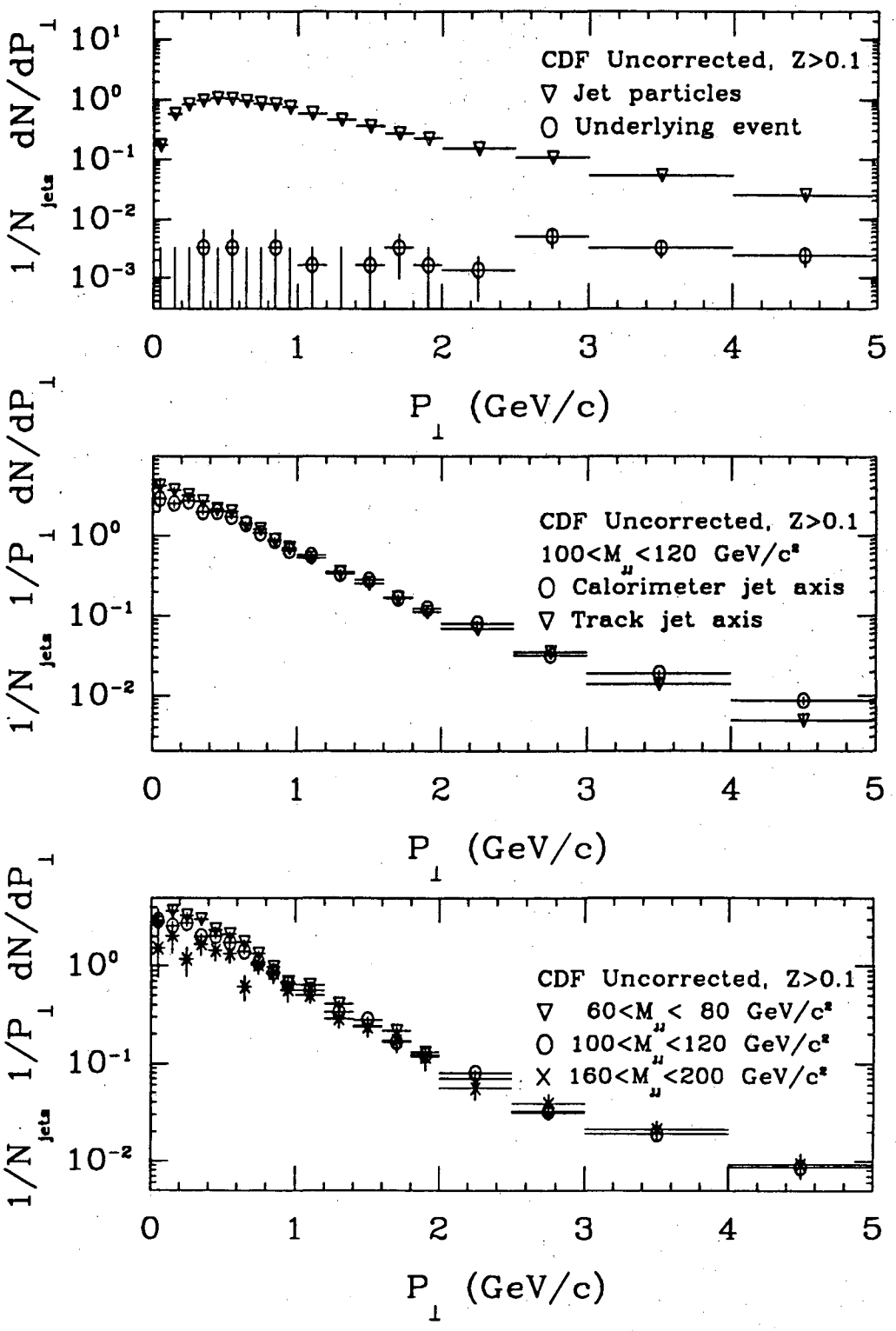

Figure 4.21: a) Transverse momentum distribution ($dN/dP_\perp$) for jet and underlying event particles. b) Transverse momentum distribution ($1/P_\perp\ dN/dP_\perp$) for two definitions of the jet axis (see text). c) Transverse momentum distribution for three dijet invariant mass intervals.

minimum $P_{||}$ causes a loss of acceptance below the rapidity

$$Y = .5 \ln\left(\frac{\sqrt{P_{||}^2 + m_\pi^2} + P_{||}}{\sqrt{P_{||}^2 + m_\pi^2} - P_{||}}\right).$$

Because of the underlying event background and the $P_{||}$ acceptance cut, the rapidity distribution cannot be reliably determined at low rapidity. For this reason, the 'rapidity plateau' observed in e^+e^- experiments is not seen in the CDF data. In Figure 4.22b, the CDF rapidity distribution for $100 < M_{JJ} < 120$ GeV/c^2 is compared with the results of three other experiments: the e^+e^- experiments TASSO[52] and AMY[54] at $\sqrt{s} = 34$ and 55.3 GeV, respectively; and UA1 at $\sqrt{s} = 546$ GeV, for the same M_{JJ} range. The systematic uncertainty for the CDF points is estimated to be approximately 10 percent, mainly from tracking efficiency; within this uncertainty the CDF and UA1 data are consistent. The height and extent of the rapidity plateau for the two e^+e^- experiments are less than height of the distribution from the CDF and UA1 experiments.

The rapidity distributions for three dijet invariant mass intervals are shown in Figure 4.23a. The height of the distribution rises by approximately 25 percent and extends outward with increasing M_{JJ} from 80 to 200 GeV/c^2. The average charged multiplicity may be obtained by integrating the rapidity distribution. However, because of the $P_{||}$ track association requirement and the underlying event subtraction, the rapidity distribution is not reliably measured for $Y < 2.0$. In the range $Y > 2.0$, which corresponds roughly to a 15 degree cone about the jet axis, the effect of the $P_{||}$ and underlying event subtraction are less than five percent. The integral of the rapidity distribution above $Y = 2.0$ is the average "jet core" charged multiplicity. The mean charged multiplicity in the jet core from CDF is shown in Figure 4.23b as a function of dijet invariant mass, and compared with the results from the TASSO, AMY, TPC and UA1 experiments. The jet core multiplicity increases from 2.4 to 5.8 over the invariant mass range 50 to 200 GeV/c^2, following the trend of the lower energy experiments. For the CDF points, the systematic uncertainty on the vertical scale is estimated to be approximately ten percent, resulting from uncertainty in efficiency and acceptance.

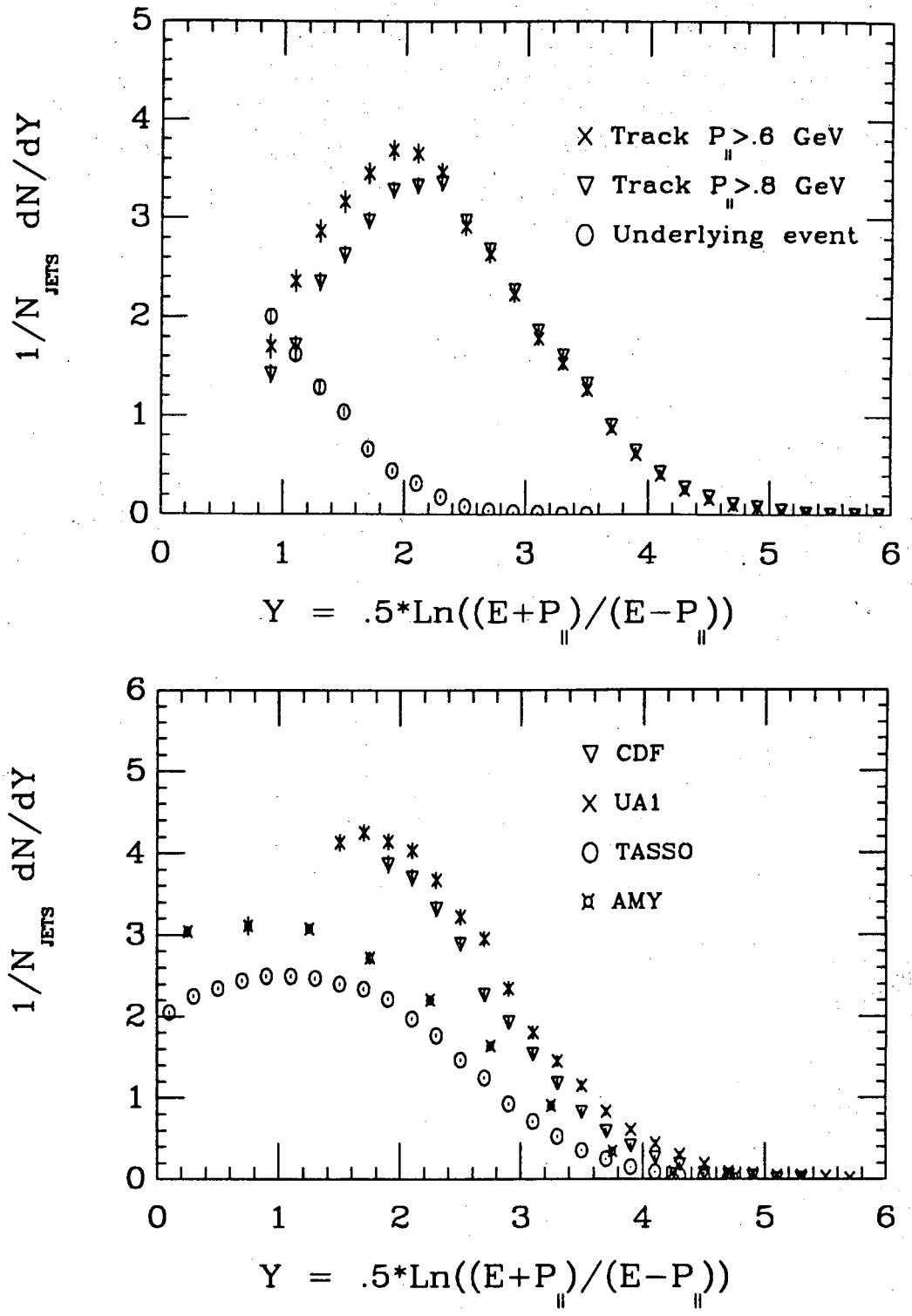

Figure 4.22: a) Charged rapidity distribution for $100 < M_{JJ} < 120$ GeV/c^2. The distribution is plotted for two values of the $P_{||}$ track association cut. b) Charged rapidity distribution for $100 < M_{JJ} < 120$ GeV/c^2, compared with results from UA1, TASSO and AMY.

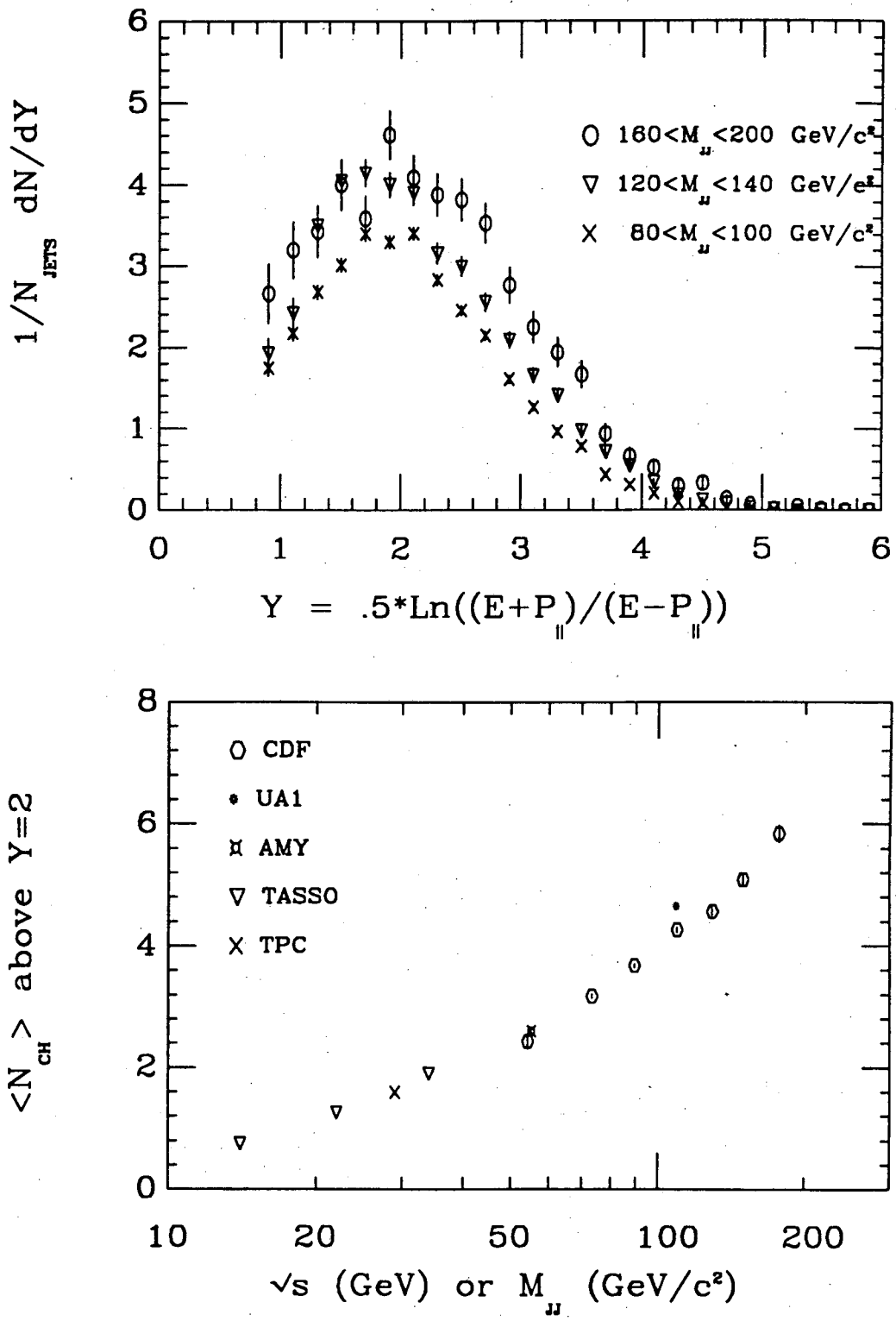

Figure 4.23: a) Comparison of the rapidity distribution for three dijet invariant mass intervals. b) Jet core charged multiplicity

Chapter 5

Summary and Conclusions

In this thesis, the fragmentation properties of hadron jets in 1.8 TeV proton-antiproton collisions were investigated using the CDF apparatus. The jets studied were expected to be predominantly gluon jets, in contrast with the predominantly quark jets observed in e^+e^- collisions.

The charged fragmentation function $D(Z)$ was presented (for events with dijet invariant mass between 80 and 140 GeV/c^2), and was in qualitative agreement with predictions of HERWIG, a QCD/cluster-fragmentation Monte-Carlo program. The average fraction of jet momenta carried by charged particles was $0.65 \pm 0.02(\text{stat}) \pm 0.08(\text{sys})$, a value consistent with the jets observed in e^+e^- data at lower center-of-mass energy. The fragmentation function became more and more peaked at low Z values with increasing dijet invariant mass. This behavior follows the trend of e^+e^- data from TASSO, and is consistent with the expectation of QCD scale breaking.

The major difficulties with the measurement (the largest contributions to systematic uncertainty to $D(Z)$) were: determination of the jet momentum scale in the calorimetry; and smearing of the distribution caused by calorimetry and tracking resolution. In addition, the track finding efficiency decreased with increasing jet energy above about 100 GeV, posing a difficult challenge for making similar measurements of higher energy jets at the Tevatron or in higher energy experiments. The efficiency issue was underscored by the jet core multiplicity (the average number of charged particles with rapidity above 2.0) which increased over a factor of two (from 2.4 to 5.8) with dijet invariant mass between 50 and 200 GeV/c^2.

The issue of whether gluons fragment differently than quarks is not clarified by these data. Quantitative comparison between the CDF jets and jets from e^+e^-, for the purpose of looking for differences between quark and gluon jets, is difficult for a variety of reasons: different Q^2 ranges of the experiments; Q^2 scale definition uncertainties; systematic errors; and differences in definition of the fragmentation variable Z. Perhaps the most promising approach in this regard will be to compare the properties of jets in QCD dijet events with jets produced in different processes (e.g. direct photon or intermediate vector boson events) within the same experiment.

Appendix A

CTC Track Reconstruction

The reconstruction code that was used for this analysis was CDF offline package version 4.4. The following description may not be completely accurate for subsequent versions.

The first step in the track reconstruction is the subtraction of time offsets (T_0's) from the raw data. These include: wire by wire T_0's determined from calibration runs which take into account delays in the read-out electronics and cables; and event T_0's from the beam-beam counters to synchronize the tracking system with the collision time. At this point, wires in cells which were known not to be working had full length hits superimposed so that tracks could be propagated across them.

The next step is pattern recognition, first using axial superlayers data only and then combining the information from the stereo layers with the axial tracks to make tracks in three dimensions. Only hits with widths between 18 and 200 nanoseconds are included in tracks. The axial search proceeds as follows:

1) Starting with the outer superlayers, short segments are located within one or two cells in a superlayer. Hit times are corrected for time of flight and signal propagation delays assuming $z = 0$. Hits with times less than 80 nanoseconds, indicating the crossing of a sense wire plane, are used as seeds. These are combined with other hits in the same and adjacent cells to make short segments, requiring at least eight hits along a one millimeter-wide road and $\Delta\phi$ less than 30° with respect to radial at the crossing. In general this solves the Left/Right ambiguity.

2) Each single superlayer track candidate is fit to a circle (described below). A first

attempt constrains the track to intersect the beam with a χ^2/DOF test to determine success. If this fails an unconstrained fit is attempted.

3) Using the fit parameters, the track is extended to inner and outer axial superlayers. First a four centimeter-wide road is used to pick up as many hits as possible. The extrapolation terminates if there are three consecutive missing hits or four consecutive bad hits (too narrow or wide). Cells with wires known to be dead and flagged with full length hits are not counted. This process is iterated using narrower roads, refitting the track with the additional hits, and, if there are enough hits, dropping some hits with large residuals.

Before associating stereo data, each axial track candidate is fit to a circle, providing the parameters c, ϕ, and d_0. In principle, these two dimensional tracks could be utilized for some analyses if the stereo search fails, since the track P_T and ϕ are reliably determined. However, with little or no information on the dip angle or z coordinate they are not useful for fragmentation study. The stereo pattern recognition takes place in three steps:

- The five cells around the track are searched to locate stereo stubs in each stereo superlayer. These can be made up of four or more hits on a two millimeter-wide road. If the slope of a test segment is consistent with being associated with the track, it is retained as a candidate in that superlayer.

- All combinations of stereo superlayer candidates are attempted to find the best stereo prediction. For each combination, a linear least squares fit in $r - z$ is performed, including the event vertex (from the VTPC) as one point, with an uncertainty of three millimeters. The combination with the lowest $\chi^2/DOF < 3$ is chosen, with the condition that all hits on the track are consistant with being inside the CTC.

- Stereo hits within a four millimeter-wide road are included on the track. If the RMS residuals of the hits to the propagated track is unreasonable, hits can be dropped to attempt to find a better combination. The final track needs to contain at least 7 stereo hits; otherwise, the stereo information is dropped.

Fitting Procedure

The parameters of the track are determined by the final fit to a helix in two or three dimensions. This is an iterated least squares fit, as there is no closed form solution due to the nonlinearity of the parametrization. The χ^2 for the parameters α_μ is defined as:

$$\chi^2 = \sum_{i=1}^{N} \frac{(d_i^{meas} - d_i^{pred}(\alpha_\mu))^2}{\sigma_i^2} = \sum_{i=1}^{N} (d_i^{meas} - d_i^{pred}(\alpha_\mu))^2 w_i^2$$

where the d are the measured and predicted distance of a hit to the wire, and the difference is weighted by one over the measurement error for each hit. The χ^2 is minimized by setting the derivative $\partial\chi^2/\partial\alpha_\mu$ to zero for each parameter, solving for $\Delta\alpha_\mu$ and iterating with the adjusted parameters. Starting from an initial assumed set of fit parameters, the fit generally converges quickly. The resulting covariance matrix is defined as

$$V_{\mu\nu} =< \delta\mu\delta\nu >= (G^{-1})_{\mu\nu}$$

where:

$$G_{\mu\nu} = \frac{1}{2}\frac{\partial^2\chi^2}{\partial\alpha_\mu\partial\alpha_\nu}$$

To convert hit times to distances, some corrections are applied, which optimize the resolution of the chamber. These correct for physical effects which are well understood and measurable, and deviations from 'nominal' conditions. They have been evaluated empirically from minimum bias data, and are applied in three levels:

0) No corrections. The basic time-distance relation $\Delta d = V_{drift} \times t_{hit}$ is assumed during the initial axial search, when a fairly crude estimate of position suffices. This is also used in general for Monte-Carlo data, since effects causing deviations to this relation are not simulated.

1) Drift velocity and time offset corrections. In this level the time-distance relation allows for different drift velocities and a distance intercept in each superlayer:

$$\Delta d = V_{drift}(SL) \times t_{hit} + d_{off}(SL)$$

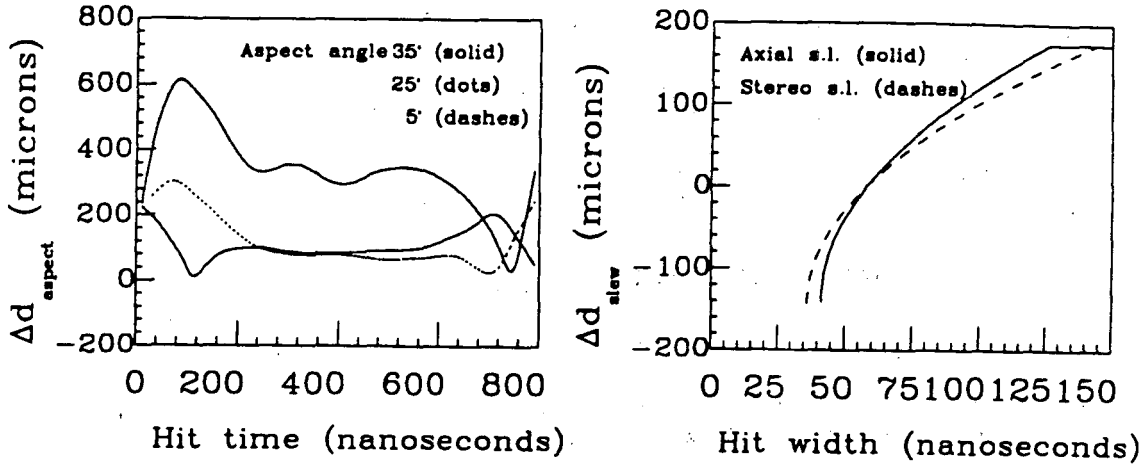

Figure A.1: Corrections applied in track finding and track fitting. a) Time/Aspect angle correction. b) Time slewing correction.

There was approximately a two percent spread in drift velocities due to different high voltages in some superlayers, which amounts to a difference of typically 800 microns. The distance offsets vary between -350 and -165 microns systematically. This level is used in the axial and stereo pattern recognition, as they are rather large systematic effects.

2) Two further corrections are applied, which were evaluated by fitting a large number of tracks in minimum-bias data. One correction is a distance offset as a function of the time of the hit and the track aspect angle. The aspect angle is the angle between the track and the nominal drift direction. This correction accounts for deviations from the ideal drift trajectory for large angle tracks and tracks very near sense wires. Figure A.1a shows this correction versus time for different aspect angles. Also, a time slewing correction is applied as a function of the pulse width of the form $\Delta d_{slew} = \alpha\sqrt{w_{hit}} - \beta$, and plotted in Figure A.1b. These corrections amount typically to less than 100 microns, and so are only used in the track fitting.

The weight for each point in the fit is set to $(1/\Delta d)^2$ to minimize the effect of points with large uncertainty.

Appendix B

CTC Tracking Efficiency Studies

B.1 Merging Single Tracks with Jet Data

In the track merging study, single simulated tracks were added to jets to test how often the reconstruction program would find them. The procedure used was as follows:

1. Events were selected with the same criteria used in the jet fragmentation analysis (Section 3.4), and a 'reference jet' was chosen within the central fiducial region ($0.1 < |\eta| < 0.7$). Tracks in the hemisphere containing that jet were reconstructed for later comparison with the event after modification.

2. A single track was generated in a GENP data bank. Tracks were generated with typical parameters for tracks within jets:

   - Exponentially falling $P_\perp$ to the jet axis, with $< P_\perp >= 0.7$ GeV/c.
   - Longitudinal momentum $P_{||} \geq 0.6$ GeV/c.
   - The spectrum was chosen appropriately for the independent variable considered, either uniform in Z in the case of efficiency vs. Z, or falling as $1/Z$ in other cases.
   - The track was either π^+ or π^- with equal probability.
   - The track was uniformly distributed in the azimuthal angle around the jet axis.
   - The tracks impact parameter $d_0 = 0$, and $z_0 = z_{event}$.
   - The track is required to fall within the full acceptance region of the CTC (Section 4.2.1).

3. The single track was simulated using the analysis-control version of the CDF detector simulation CDFSIM with the following parameters and modifications for this study:

   - The CTC detector only was simulated, including the effects of material encountered between the interaction point and the CTC.
   - Smearing or overwriting the event vertex was disabled, and vertex information from the real event was stored in an OBSV bank.
   - The particle was allowed to decay before or within the CTC.
   - Addition of random noise hits in the CTC was disabled.
   - A global T_0 offset of 100 nanoseconds was added to the simulated data and corrections for drift velocity were applied in reverse.

4. Event by event local T_0's were added to the simulated CTC element bank, which was then merged with the element bank from the reference event using the routine CTMERG. The merged element bank was then reconstructed exactly as real data. Normally simulated Monte-Carlo data with run numbers less then 10 are treated differently than real data by the reconstruction program.

5. The merged event was analyzed as described below.

Steps 2 through 5 were repeated several times for each event.

In the analysis of the merged event, the goal was to identify which, if any, of the reconstructed tracks was the simulated track. For each track the corresponding hits in the merged raw data bank were located using the CTCL link bank, and those hits were compared with the set of simulated hits. A matched hit on a wire occurred if two hits had leading edge times within four nanoseconds (200 microns) of each other. The fraction of matched hits on all tracks is shown in Figure B.1a. The criterion for successfully identifying the simulated track was that the ratio of matched hits to possible hits was greater than 25 percent. In cases where there were more than one such track the one with the largest fraction was chosen.

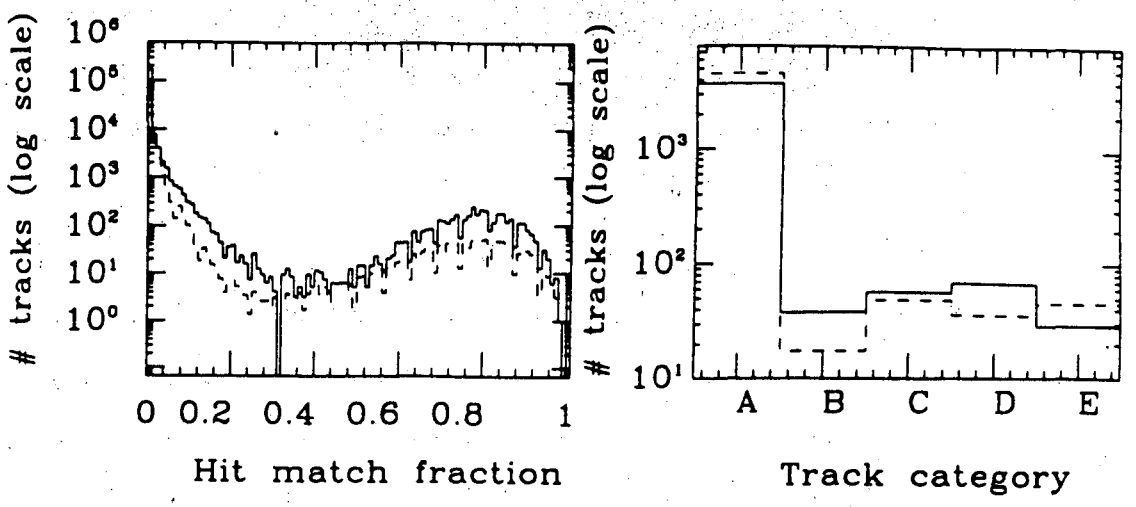

Figure B.1: a) Fraction of simulated hits contained on tracks found in the merged events (solid) and simulated Monte-Carlo events (dashes). b) Fraction of tracks in the five classes in merged events (solid) and simulated Monte-Carlo events (dashes).

Events were divided into five classes :

A) The matching track passed selection criteria and was close to the generated track in the z coordinate. This required the mean distance from the generated helix to be within five centimeters in z along the length of the track.

B) The matched track passed selection criteria, but did not adequately match the generated track parameters in z, indicating that the stereo information was probably confused.

C) The matched track was found in two dimensions only, without stereo information.

D) The matched track failed one of the other selection criteria.

E) No track was found with more than 25 percent of simulated hits.

The fraction of tracks found in the various categories is shown in Figure B.1b. The efficiency was the probability of finding the track in categories A or B, since both entered the physics plots. The efficiency was investigated as a function of various quantities, including: $1/P_t$, $\Delta\eta$, $\Delta\phi$ and ΔR to the jet; jet multiplicity and E_T; average distance to the closest track in $r-\phi$; and physics variables such as Z, Y, and $P_\perp$ to the jet axis. Though

the efficiency really depends more on local track/hit density which is difficult to quantify, the Monte-Carlo technique effectively integrated over these variables. In evaluating the efficiency as a function of physics quantities, the goal was to be able to make a bin-by-bin correction to a measured distribution.

The track merging technique has the advantage that the real CTC data, including effects which are difficult to simulate well such as spirals, noise and detector problems, are used as camouflage for the single track. The method has several disadvantages. The first is that since each event is artificially more dense by one track than an actual event, the efficiency measured is an underestimate of the true efficiency. The interpretation of variables is not always clear; for instance, the efficiency at high Z could only be determined by adding high P_T track to a low multiplicity, low energy jet. In addition, since a single "measurement" of efficiency requires an entire event to be reconstructed, the procedure is quite CPU intensive.

B.2 Monte-Carlo Event Simulation

The track reconstruction efficiency was also checked using simulated PYTHIA[41] Monte-Carlo events. In this case each charged particle in an event could be used as an independent test of efficiency, thereby reducing the amount of CPU time needed to obtain reasonable statistical precision.

Five samples of jet events were generated with minimum jet P_T's ranging from 20 to 100 GeV/c. The calorimetry and CTC data were simulated, and events were selected using the measured jet clusters. Each generated charged particle associated to a jet was compared with the CTC tracks found in the event, requiring (as in the track merging) at least 25 percent of simulated hits on a track to identify the track. The fraction of match hits on tracks and the number of tracks found in the various categories is compared with the track merging method in Figures B.1a and B.1b.

B.3 Estimating Efficiency from Data

A crude estimate was made for track finding efficiency using the data in order to check the above methods. In this study the efficiency was defined as the number of 'good' tracks which pass track selection criteria divided by the number of 'probably real' tracks. The latter category included any tracks which had eighteen or more hits in the axial superlayers two, four and six, and also had at least some hits in superlayer six or outer, so that the tracks considered were mostly within the full acceptance region. The efficiency determined using this method was approximately 90 percent, slightly lower than that obtained in the track merging and Monte-Carlo studies. This lower result may have been partially due to secondaries, acceptance uncertainties, and the effects of multiple tracks which shared the same set of hits.

Appendix C

Unfolding Detector Resolution Effects to the Charged Fragmentation Function

C.1 General Procedure

The measured fragmentation function is a convolution of a produced distribution with Gaussian resolution functions in the two independent variables jet momentum (P_{jet}) and track curvature ($C \equiv 1/P_{track}$), where $Z \simeq \frac{1}{P_{jet}C}$. In the discussion below, the jet momentum will be referred to simply as P (not to be confused with the track momentum).

The measured number of tracks in a Z interval of width δZ for jets in a jet momentum interval of width δP is expressed as:

$$N_{meas}(Z,P) = D_{meas}(Z)\ \delta Z\ \Sigma_{meas}(P)\ \delta P = \frac{\partial^2 n}{\partial Z \partial P}\ \delta P\ \delta Z \qquad \text{(C.1)}$$

In the above relation, the fragmentation function D is the number of tracks per unit Z per jet and the jet cross section Σ expresses the number of jets per GeV/c per unit luminosity. This "bin" is illustrated as a shaded rectangular region a two dimensional plot of P vs Z (Figure C.1a). In fact, the above equation is only true in the small bin-size limit, since D and Σ are steeply falling distributions.

The resolution smearing is best demonstrated on a two dimensional plot of P vs. C, shown in Figure C.1b. Since the two measurements are independent the effect of resolutions in track curvature and jet momentum is to move events vertically and horizontally, respectively. The number of tracks measured in a bin in the (P,C) plane is the density

$$\rho_{meas}(C,P) = \frac{\partial^2 n}{\partial C \partial P} \qquad \text{(C.2)}$$

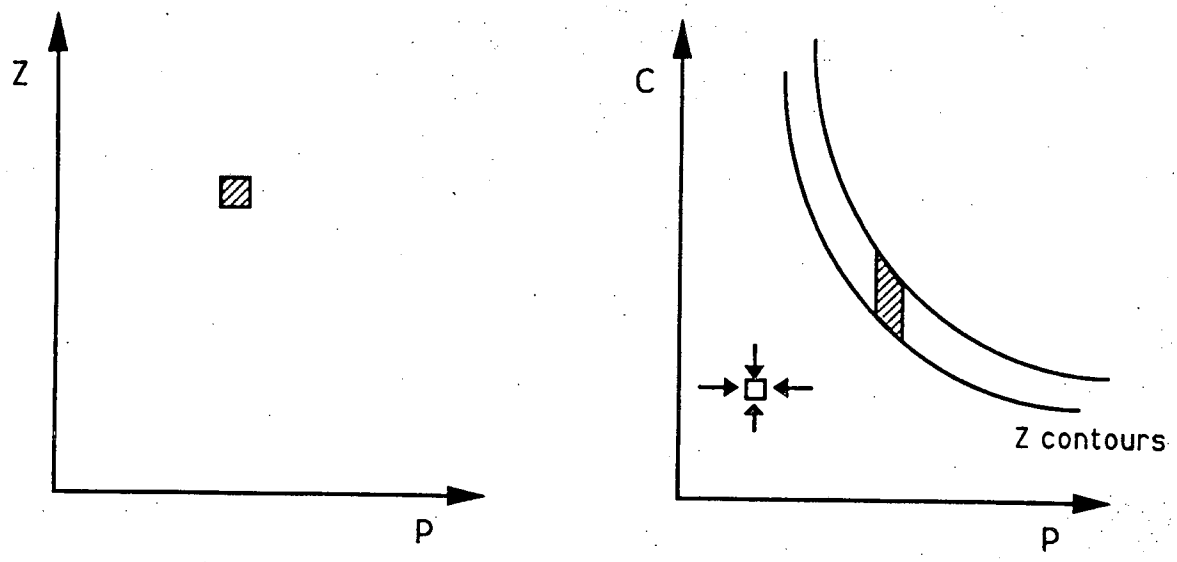

Figure C.1: a) Two dimensional plot of P_{jet} vs. Z. A single bin of width δZ and δP is shown as a shaded rectangle. b) Plot of P_{jet} vs C_{track}. Contours of constant Z are shown as hyperbolae on this plot.

multiplied by the bin area. The density in (C,P) is related to the density in (Z,P) by a Jacobian:

$$\frac{\partial^2 n}{\partial C \partial P} = |\partial Z/\partial C| \frac{\partial^2 n}{\partial Z \partial P} = \frac{1}{PC^2} D(Z)\Sigma(P) \qquad \text{(C.3)}$$

The measured number of tracks in the bin is related to the produced density of tracks by the relation:

$$\rho_{meas}(C,P)\ \delta C\ \delta P = \iint dP' dC' \rho_{prod}(C',P')\ [R_C(C,C')\ \delta C]\ [R_P(P,P')\ \delta P] \qquad \text{(C.4)}$$

The resolution functions R_C and R_P are the probability per unit measured C or P to observe the produced (primed) quantity at the measured (unprimed) value. The convolution integral expresses the conservation of probability, as long as the resolution functions are normalized to unity ($\int R = 1.0$) and the complete space of the variables P and C are integrated over.

The number of measured events within the interval $[Z_1 < Z < Z_2,\ P_1 < P < P_2]$ is obtained by integrating the density in the interval:

$$\begin{aligned} N_{meas}(Z,P) &= \int_{P_1}^{P_2} dP' \Sigma_{meas}(P') \int_{Z_1}^{Z_2} dZ' D_{meas}(Z') \\ &= \int_{P_1}^{P_2} dP' \int_{\frac{1}{P'Z_2}}^{\frac{1}{P'Z_1}} dC' \rho_{meas}(C',P') \end{aligned} \qquad \text{(C.5)}$$

For a sufficiently small momentum range, the integral over P' can be replaced by the momentum interval. Substituting for ρ_{meas}, the measured fragmentation function in a Z bin is:

$$\frac{1}{\Delta Z}\int_{Z_1}^{Z_2} dZ' D_{meas}(Z') = \frac{1}{\Delta Z}\int_{\frac{1}{P}Z_2}^{\frac{1}{P}Z_1} dC \iint \frac{dP'dC'}{P'C'^2}\frac{\Sigma_{prod}(P')}{\Sigma_{meas}(P)} D_{prod}(Z') R_C(C',C) R_P(P',P) \qquad \text{(C.6)}$$

C.2 Unfolding the Jet Momentum Spectrum

The functions Σ_{prod} and Σ_{meas} are determined by fitting the measured jet momentum distribution. The fits were performed using MINUIT program[55], assuming Poisson statistics for the bin contents[56]. The measured distribution of jet momenta in the event sample is shown in Figure C.2a. Below about 60 GeV/c the shape of the spectrum is biased by trigger thresholds and selection criteria. A power law parametrization was used to fit the spectrum:

$$\Sigma(P_{jet}) = \alpha' \times P_{jet}^{-\beta} = \exp(\alpha\beta) \times P_{jet}^{-\beta}$$

The parameters α and β (as opposed to α' and β) were used in order to reduce the correlation between them. A fit in the range 60 to 120 GeV gave the parameter values: $\alpha = 5.048 \pm .020$; $\beta = 5.793 \pm .138$. Statistical fluctuations in the momentum range near 120 GeV/c cause a mediocre fit χ^2/DOF of 40.7/28. However, the optimum parameters were insensitive (within statistical errors) to the upper and lower limits between 56 and 180 GeV/c.

The effect of resolution on the produced distribution is expressed via the convolution[57]:

$$\Sigma_{meas}(P) = \int_{P_{min}}^{P_{max}} dP' R_P(P,P') \Sigma_{prod}(P') \qquad \text{(C.7)}$$

where the resolution function R_P is Gaussian with the width σ_P from Figure 3.8:

$$R_P(P,P') = \frac{1}{\sqrt{2\pi}\sigma_P(P')} \exp\left[-\frac{(P-P')^2}{2\sigma_P(P')^2}\right]$$

The upper and lower limits of integration were set to the momentum $P_{jet} \pm 5\sigma$ of resolution evaluated at the limits. This integral is numerically evaluated at each bin, and Σ_{meas} is fit to the data by varying the parameters in Σ_{prod}.

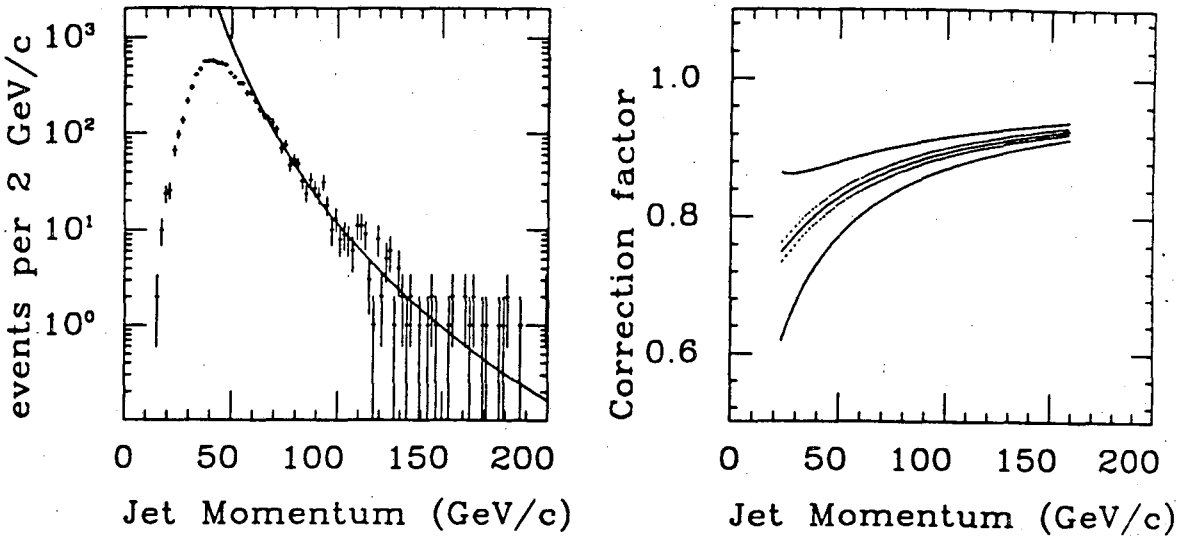

Figure C.2: a) Measured jet momentum distribution. The fit shown is a power law parametrization. b) Resolution corrections to the spectrum derived from the fit.

The optimum parameter values from the convoluted fit were $\alpha = 5.04 \pm .02$ and $\beta = 5.69 \pm .03$. The ratio $\Sigma_{prod}/\Sigma_{meas}$ is the correction factor which relates the measured to produced jet momentum distributions. The results are shown in Figure C.2b for five separate cases. The center curve is for the nominal jet resolution, and the upper and lower outer curves are for optimistic and pessimistic jet resolution estimates, respectively. The other two curves are the correction factors obtained using the 1σ uncertainties on the optimum fit parameters. This uncertainty can be neglected compared to the resolution uncertainty. The correction is always less than unity, as there are more measured jets than are actually produced at a given momentum. Due to the steepness of the spectrum, there is a net migration of jets from lower to higher momentum as a result of resolution smearing.

C.3 Unfolding the Fragmentation Function

With the above estimates for the jet cross section produced and measured, the effect of resolution on a produced fragmentation function is given by Equation C.6. For the purposes of evaluating a correction for the measured spectrum, a parametrization of the measured frag-

mentation function was used as the produced fragmentation function. This approximation may be justified if the magnitude of the correction D_{prod}/D_{meas} is not far from unity.

Three different parametrizations were used for $D(Z)$. As the functional form used affects the derived correction, it is more important to use a smooth function better fitted to the data than one preferable based on theoretical reasoning.

The three fits to the measured distribution are shown in Figure C.3. First, an exponential form was used:

$$D(Z) = \frac{\alpha}{Z} \times \exp(-\beta * Z)$$

This parametrization has been used by UA1 to describe their data[22]. It gives a poor fit to the CDF data ($\chi^2/DOF = 55/25$), due to the shape of the distribution near $Z = 0.5$. On theoretical grounds this parametrization is unattractive as it converges to a constant at $Z = 1$ without steepening; however it fits well to some hadron collision data. A more theoretically desirable parametrization was also attempted:

$$D(Z) = \frac{\alpha}{Z} \times (1 - Z)^{\beta}$$

This fit the data very poorly ($\chi^2/DOF = 322/25$), as the function falls much faster than the data at $Z > 0.6$.

The third parametrization is a spline of the exponential parametrization, which describes the low Z end well, with a fourth order polynomial (on a logarithmic scale) for higher Z:

$$D(Z) = \begin{cases} \frac{\alpha}{Z} \times \exp(-\beta * Z) & \text{for } Z < Z_{knot} \\ \exp(a + bZ + cZ^2 + dZ^3 + eZ^4) & \text{for } Z > Z_{knot} \end{cases}$$

At the boundary, the function value and first and second derivatives were required to match, so that three of the parameters are eliminated by the following relations:

$$c = 1/Z_{knot}^2 - 3dZ_{knot} - 6eZ_{knot}^2$$

$$b = -(1/Z_{knot} + \beta) - 2cZ_{knot} - 3dZ_{knot}^2 - 4eZ_{knot}^3$$

$$a = \ln \alpha - \ln Z - \beta Z - bZ_{knot} - cZ_{knot}^2 - dZ_{knot}^3 - eZ_{knot}^4$$

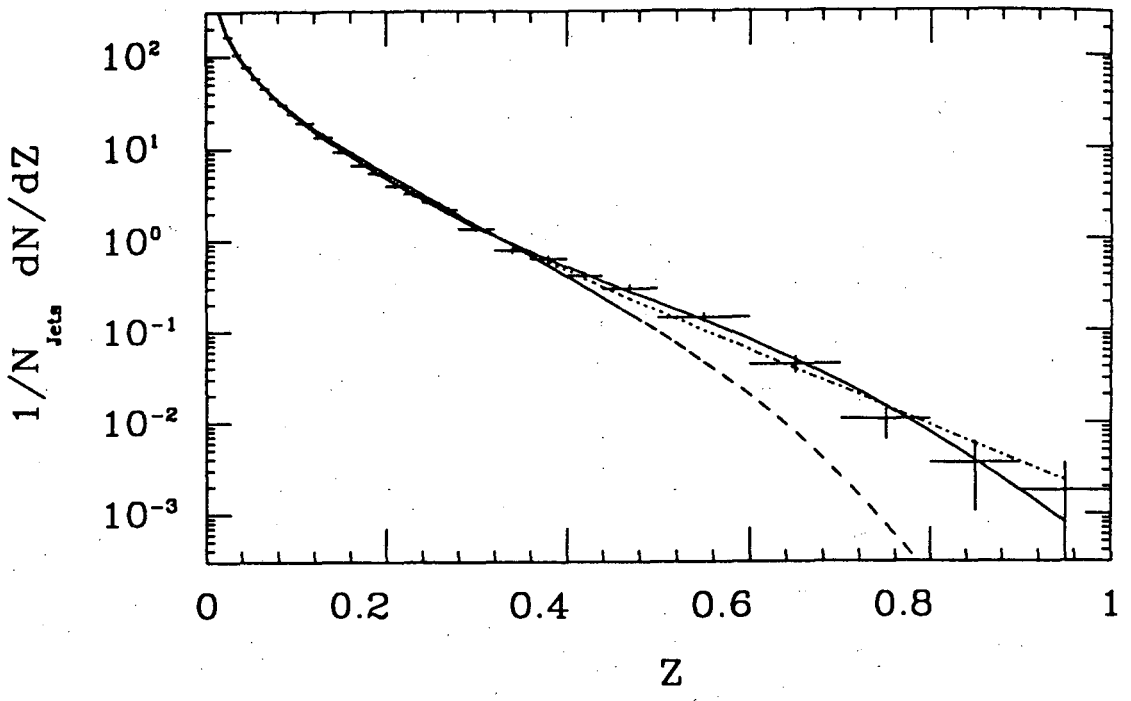

Figure C.3: Fits to the measured fragmentation function (see text). The three parametrizations shown are an exponential form (dashes), a power law form (dots), and a splined fit (solid).

The convolution integral is sensitive to derivatives higher than the first, so it is important to match the second derivative. The optimum choice of Z_{knot} was found to be 0.24, by varying the position and comparing the fit χ^2 to the measured spectrum. This function fit the data quite well as shown in Figure C.3, so it was used to evaluate the correction for resolution smearing.

Correction factors for the 27 bins of the distribution, evaluated as $D_{true}(Z)/D_{meas}(Z)$, are shown for the spline fit in Figure C.4a. As before, the limits of integration are set at $\pm 5\sigma$ from the 'nominal' P_{jet} and C_{track} at the measured Z. Had the fit been to a two-dimensional grid in P_{jet} and C_{track} these nominal values would have been the measured quantities. Instead, the nominal P_{jet} is taken as the average jet momentum in the dijet invariant mass interval, $< P_{jet} >$. The nominal C for a measured Z is then equal to $\frac{1}{Z<P_{jet}>}$. Also shown are the corrections for P_{jet} and C_{track} resolution separately, which were obtained by setting the resolution of the other quantity to a δ function. Note that the momentum resolution does not affect the distribution except at high Z, due to the fact

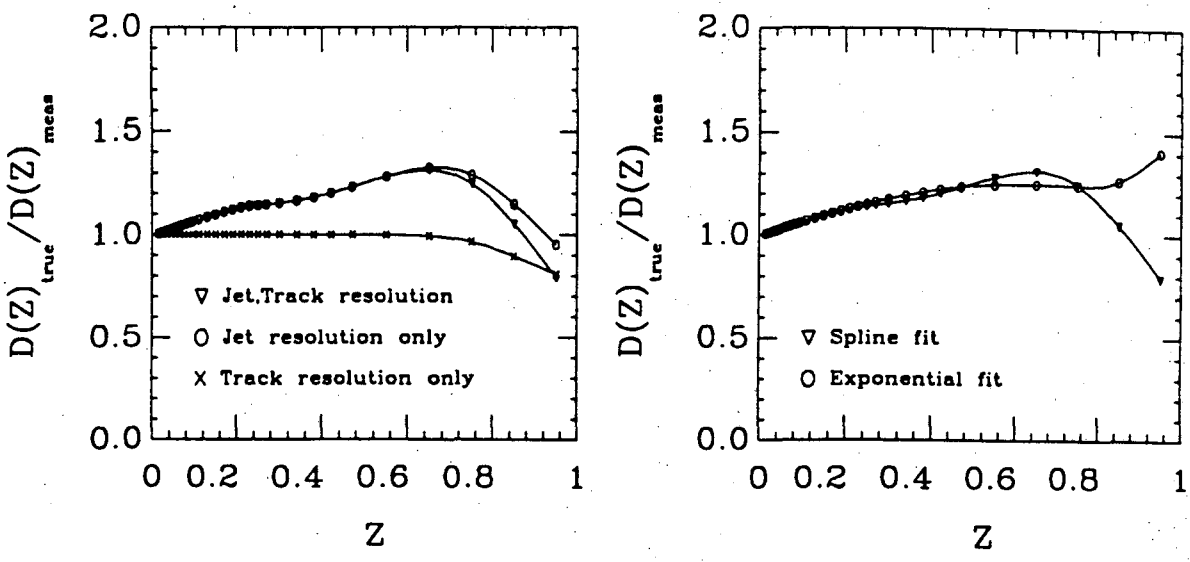

Figure C.4: a) Correction factors due to resolution smearing, evaluated using the spline parametrization. The separate contributions from track and jet momentum resolution are also shown. b) Comparison of the corrections evaluated using the spline and exponential fit parametrizations.

that the fractional track momentum resolution worsens linearly with P_{track} (or Z).

The effect of the energy resolution is to cause the measured distribution to be less than the produced distribution for most of the Z range, by shifting events from higher to lower Z values. This is the same effect as is observed in the jet spectrum, that jets tend to come from lower momenta than where they are measured. Had the jet spectrum been ignored, the result would have been that events tend to shift up in Z.

At Z values approaching 1, the correction factor decreases below unity for two reasons: the asymmetric momentum errors can cause tracks to be measured at substantially higher Z values than they are produced; and the distribution becomes steeper, which is reflected in the parametrization. In Figure C.4b the corrections are compared using the spline with those evaluated using the exponential form. There is little difference except at high Z, where the correction factors using the exponential form are never less than unity.

Imprecise knowledge of the detector resolutions adds an additional uncertainty to the correction factors. In Figure C.5a the correction factors are evaluated using the upper, middle and lower estimates for jet momentum resolution; Figure C.5b shows the same for

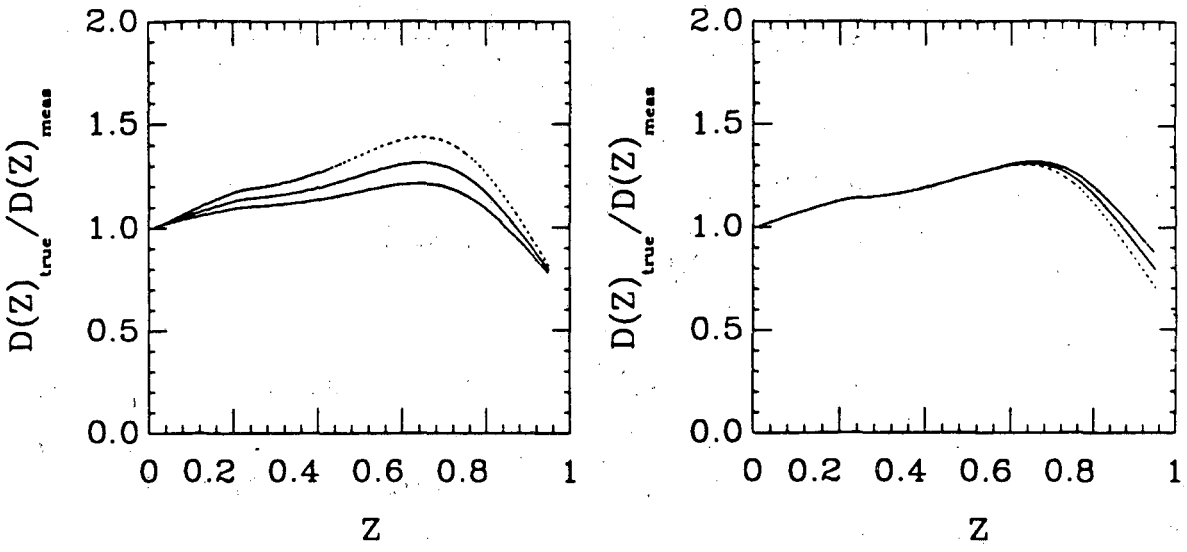

Figure C.5: Effects of resolution uncertainty on correction factors to $D(Z)$ a) Correction factors using low, medium and high estimates of jet momentum resolution. b) Correction factors using low, medium and high estimates of track momentum resolution.

track momentum resolution. The systematic uncertainty from these is considerable.

The detector resolution effects on dN/dZ have also been investigated using a simple Monte-Carlo generator and ISAJET[39]. The simple Monte-Carlo incorporated the basic elements of the problem:

- The jet momentum spectrum $\Sigma_{prod} \propto P_{jet}^{-5.7}$.
- Jet fragmentation into pions according to the Feynman-Field prescription[9].
- Jet and track resolution as measured from the data.

Events were selected and treated identically to the data. The ratio of produced to measured dN/dZ for the simple Monte-Carlo and is plotted in Figure C.6a. The predicted correction factor, shown by the solid line, overestimates the effect of resolution for $Z < 0.6$. A similar result was observed with ISAJET data simulated with the QFL program (Figure C.6b).

The effect of jet momentum resolution smearing appears to be less than the corrections predict. This may be true for the following reasons:

- Events were selected with a requirement on two jet sum E_T, with no requirement on a single jet.

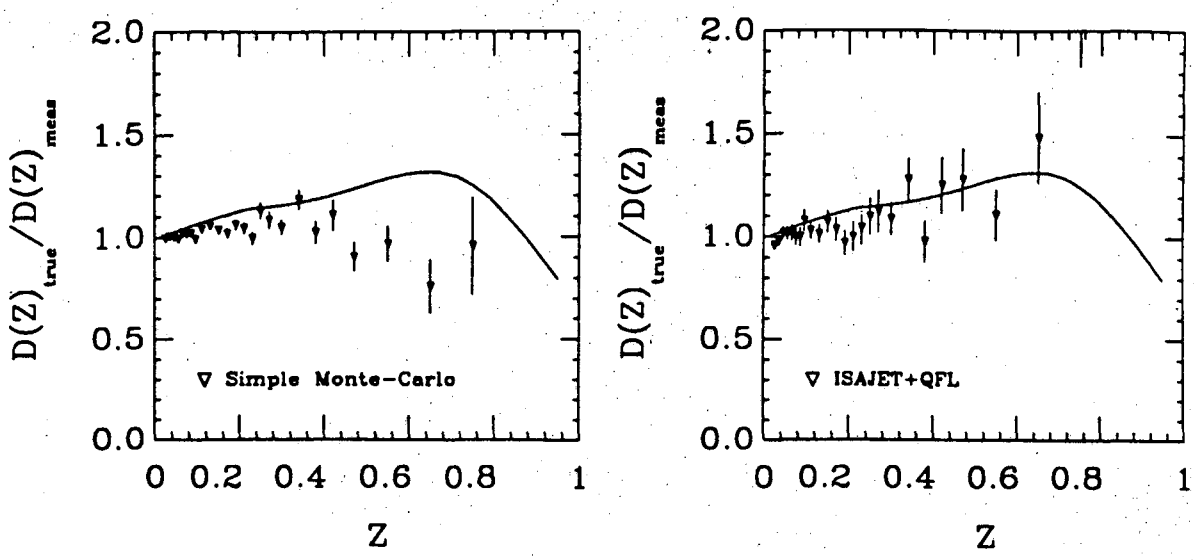

Figure C.6: a) Ratio of produced to measured dN/dZ from the simple Monte-Carlo. b) Ratio of produced to measured dN/dZ from ISAJET+QFL.

- A dijet K_T significance cut was imposed.
- The fragmentation function is plotted for an interval in dijet invariant mass (not jet momentum).

The resolution-smearing correction is shown with estimated systematic bounds in Figure 4.9. The uncertainties were estimated to take into account the discrepancy between the evaluated corrections and the Monte-Carlo results at $Z < 0.6$, the uncertainty in track and jet momentum resolutions, and the uncertainty in the shape of the fragmentation function for $Z > 0.6$.

Bibliography

[1] P. A. M. Dirac, Proceedings of the Royal Society of London, **A 114**, 243 (1927).

[2] Glashow, S. L., Nucl. Phys. **22**, 579 (1961).
Weinberg, S., Phys. Rev. Lett. **19**, 1264 (1967).
Salam, A., Nobel Symposium # 8, edited by N. Svartholm, Almqvist and Wiksell, Stockholm, p. 367 (1968).

[3] Bardeen, W. A., Fritzsch, H., and Gell-Mann, M., in *Scale and Conformal Symmetry in Hadron Physics*, edited by R. Gatto, Wiley, New York (1973).
Gross, D. J. and Wilczek F., Phys. Rev. **D8** 3633, (1973).
Weinberg, S., Phys. Rev. Lett. **31** 494, (1973).

[4] G. Hanson *et al*, Phys. Rev. Lett. **35**, 1609 (1975).

[5] M. Banner *et al*, Phys. Lett. **118B**, 203 (1982).
G. Arnison *et al*, Phys. Lett. **123B**, 115 (1983).

[6] R. P. Feynman, *Photon-Hadron Interactions*, W. Benjamin (1972).
M. Berman, J. D. Bjorken and J. B. Kogut, Phys. Rev. **D4**, 3388 (1971).

[7] I. Hinchliffe, private communication.

[8] E. Eichten *et al*, Rev. Mod. Phys. **56**, 579 (1984).

[9] R. P. Feynman and R. D. Field, Nuch. Phys. **B136**, 1 (1978).

[10] B. Anderson *et al*, Phys. Rep. **97**, 31 (1983).

[11] S. Wolfram, *Proceedings of the 15th Rencontre de Moriond*, ed. J. Tran Thanh Van, 549 (1980).

[12] B. R. Webber, Nucl. Phys. **B238**, 492 (1984).

[13] K. Konishi, A. Ukawa, and G. Veneziano, Nucl. Phys. **B157**, 45 (1979).

[14] S. J. Brodsky and J. Gunion, Phys. Rev. lett. **37**, 402 (1976).

[15] A. H. Muller, Nucl. Phys. **B241**, 141 (1984).

[16] M. Derrick *et al*, (HRS Collaboration), Phys. Lett. *165B*, 449 (1985).

[17] A. Petersen *et al*, (MARKII Collaboration), Phys. Rev. Lett. *55*, 1954 (1985).

[18] W. Bartel *et al*, (JADE Collaboration), Phys. Lett. **123B**, 460 (1983).

[19] G. Altarelli and G. Parisi, Nucl. Phys. **B127**, 298 (1977).

[20] C. Peterson, D. Schlatter, I. Schmitt, and P. M. Zerwas, Phys. Rev. **D27**, 105 (1983).

[21] W. Braunschweig *et al* (TASSO Collaboration), DESY Report 89-032 (1989).

[22] G. Arnison *et al*, Nucl.Phys. B276 253 (1986).
P. Ghez, Ph.D. Thesis, LAPP-EXP-86.02 (1986).

[23] The CDF collaboration is listed on page vi.

[24] F.Abe *et al*, Nucl.Instr.and Meth., A271, 387 (1988).

[25] Tevatron 1 Design Report, Fermilab, 1984.

[26] D. Mohl, G. Petrucci, L. Thorndahl and S. van der Meer, Physics Reports **58**, 73 (1980).

[27] Jackson, J. D., *Classical Electrodynamics*, Chapter 13, 2nd. Edition, John Wiley and Sons, New York, 1975.

[28] Sauli, F., "Principles of Operation of Multiwire Proportional and Drift Chambers", CERN

[29] H. Brafman *et al*, IEE Trans. Nucl. Sci. NS-32, 336 (1983).

[30] R. L. Gluckstern, Nucl.Instr.and Meth., 24, 381 (1963).

[31] A. D. Johnson, G.H.Trilling, Mark II Note TG-301 (unpublished).

[32] P. Billoir *et al* Nucl.Instr.and Meth., A241, 115 (1985). P. Avery, Cleo Note CBX 87-38 (unpublished).

[33] F. Bedeschi et al., Nucl. Inst. & Methods A **268**, 50 (1988).

[34] C. W. Fabjan, CERN-EP/85-84 (1985).

[35] S. Behrends, S. Kuhlmann, D. Amidei, F. Rimondi, CDF note # 583, (1987).

[36] U.S. Department of Energy report DOE/ER-0189 (1983).

[37] F. Abe *et al*, Phys. Rev. Lett **61**, 1819 (1988).

[38] D. Brown *et al*, CDF Note # 605 (1988).

[39] ISAJET version 6.02 Monte-Carlo program, described in F. Paige and S. Protopescu, *Proceedings of the Summer Study on the Physics of the Superconducting Super-Collider*, ed. R. Donaldson and J. Marx, 320 (1986).

[40] HERWIG version 3.2 Monte-Carlo program, described in G. Marchesini and B. R. Webber, Nucl. Phys. B **310** 461 (1988).

[41] PYTHIA version 4.8 Monte-Carlo program, described in Comp. Phys. Comm **46**, 43 (1987).

[42] S. dell'Agnello *et al*, CDF Note # 1015 (1989).

[43] S. Kuhlmann *et al*, CDF Note # 686 (1988).

[44] B. Flaugher and S. Kuhlmann *et al*, CDF Note # 685 (1988).

[45] S. Behrends, S. Kuhlmann, CDF Note # 684 (1988).

[46] S. Kuhlmann, CDF Note # 687 (1988).

[47] R. D. St.Denis, Ph.D. Thesis, Harvard University (1988).

[48] R. Ansari *et al*, Phys. Lett. **B186**, 452 (1987).

[49] B. Hubbard, CDF Note # 824 (1988).

[50] B. Hubbard, CDF Note # 768 (1988).

[51] D. W. Duke and J. F. Owens, Phys. Rev. **D30** 49 (1984).

[52] M. Althoff *et al*, Z.Phys C22, 307 (1984).

[53] H. Aihara *et al*, Phys.Rev.Lett **52**, 577 (1984).

[54] Y. K. Li *et al*, submitted to Phys. Rev. D (1989).

[55] F. James and M. Roos, Computer Physics Communications **10**, 343 (1975).

[56] S. Behrends and J. Huth, CDF Note # 747 (1988).

[57] R. M. Harris, CDF Note # 606 (1988).

LAWRENCE BERKELEY LABORATORY
TECHNICAL INFORMATION DEPARTMENT
1 CYCLOTRON ROAD
BERKELEY, CALIFORNIA 94720